



HAL
open science

Characterization of the bone-implant interface and numerical analysis of implant vibrational behavior for a mechanics based preoperative planning of total hip arthroplasty

Andres Rondon

► **To cite this version:**

Andres Rondon. Characterization of the bone-implant interface and numerical analysis of implant vibrational behavior for a mechanics based preoperative planning of total hip arthroplasty. Biomechanics [physics.med-ph]. Université Pierre et Marie Curie - Paris VI, 2017. English. NNT : 2017PA066059 . tel-01596018

HAL Id: tel-01596018

<https://theses.hal.science/tel-01596018>

Submitted on 27 Sep 2017

HAL is a multi-disciplinary open access archive for the deposit and dissemination of scientific research documents, whether they are published or not. The documents may come from teaching and research institutions in France or abroad, or from public or private research centers.

L'archive ouverte pluridisciplinaire **HAL**, est destinée au dépôt et à la diffusion de documents scientifiques de niveau recherche, publiés ou non, émanant des établissements d'enseignement et de recherche français ou étrangers, des laboratoires publics ou privés.

Université Pierre et Marie Curie, Paris 6

École doctorale : Sciences mécaniques, acoustique, électronique et robotique de Paris

Thèse de Doctorat

Spécialité : ACOUSTIQUE - BIOMÉCANIQUE

Présentée par

Andres RONDON

en vue d'obtenir le grade de
Docteur de l'Université Pierre et Marie Curie, Paris VI

**RECHERCHE D'UN CRITÈRE MÉCANIQUE DE STABILITÉ DANS LE CADRE DU PLANNING
DE L'ARTHROPLASTIE TOTALE DE HANCHE.
ANALYSE NUMÉRIQUE DU COMPORTEMENT VIBRATOIRE DE L'IMPLANT ET
CARACTÉRISATION DE L'INTERFACE OS-IMPLANT.**

**CHARACTERIZATION OF THE BONE-IMPLANT INTERFACE AND NUMERICAL ANALYSIS OF
IMPLANT VIBRATIONAL BEHAVIOR FOR A MECHANICS BASED PREOPERATIVE PLANNING
OF TOTAL HIP ARTHROPLASTY.**

Soutenance prévue le 03 mars 2017

Composition du jury :

Rapporteurs :	Sebastien LAPORTE	Professeur des Universités, Arts et Métiers ParisTech
	Martine PITHIOUX	Chargée de Recherche CNRS, Aix Marseille Université
Examineurs :	François OLLIVIER	Maître de Conférences, Université Pierre et Marie Curie
	Moussa HAMADOUCHE	Professeur des Universités, Praticien hospitalier, Université Paris 5
Directeur de thèse :	Quentin GRIMAL	Professeur des Universités, Université Pierre et Marie Curie
Co-encadrant :	Elhadi SARIALI	Professeur des Universités, Praticien hospitalier, UPMC

Acknowledgments

I would like to start by thanking the LIB, for opening its doors for me, giving me one of the most exciting and challenging opportunities I've ever had, a once-in-a-lifetime experience that I will never forget and will always be grateful for.

To my advisor and thesis director, Quentin Grimal, thanks for the opportunity, for sharing your knowledge and savoir-faire with me, for your encouragement, your patience, and for always pushing me to do my best. Your methods and pedagogy for transferring your knowledge and ideas, and your attention to details, provided me with great lessons that I'm sure will help me throughout all my life.

Hedi Sariali, my co-supervisor, I want to thank you for bringing such an important insight to this project with your clinical knowledge and expertise. I enjoyed a lot working with you, learning about your work as a surgeon provided a very interesting touch to my research experience.

Pascal Laugier, and all the great team of people that works in the LIB, thanks and congratulations for making of this lab such a great place to do research at. I am leaving the lab as a proud LIBien.

I would like to acknowledge Pascal Dargent, Didier, Sylvain, Quentin V., Stefroy, Christine Chappard. I am very grateful for your help, cooperation, and involvement in one way or another for the development of my thesis. Thanks to Symbios, for their contribution to this project.

I would like to thank Prof. Sebastien Laporte, and Martine Pithioux, for accepting being the reviewers of my thesis. And also François Ollivier, and Moussa Hanamoduche for being part of the jury as well.

Laura and Sylvain, our great conversations always helped me gain a better perspective, I appreciate your friendship and guidance. And to all the group of lab mates, with whom I not only had the opportunity and honor to share this great learning experience, but also have now the pleasure to call my friends: Simon, Alexandre, Xiran, Florian, Nico, Chao, Michael, Jerome, Kyle, Thanh, Johannes, Guillaume. And of course, a very special merci, to my good amigo and partner in crime Quentin Vallet, with whom I shared the dream-team bureau of the LIB! Thanks buddy for three+ years of great moments and laughter, and for all your help on this roller-coaster ride that we shared (claro que si, my friend!). Thanks to all of you, my good friends, for making of coming every day to the lab such a joy and a treat... (I will miss our happy jeudis).

Finally, I want to thank my family and friends, in Venezuela, in Paris, and around the world, for being my support, and helping me put things into perspective when things got rough. Special thanks to my mother for her support and words of wisdom, mis logros son tus logros mama.

Abstract

This thesis work is concerned with the enhancement of three-dimensional preoperative planning (P3D) tools for total hip reconstruction. When cementless implants are used, primary stability is vital for a good osseointegration. For this, a correct selection of the size and position of the implant is necessary. The surgeon may use P3D based on the computed tomography scanner of the patient's hip to optimally select the implant's size and anticipate the final implant's position. Available planning methods lack a mechanical criterion reflecting the actual quality of the bone-implant contact. In this work we propose a method to improve P3D using a vibrational finite element analysis to calculate patient-specific mechanical parameters representative of primary stability.

We found that the modal response of the stem is very sensitive to changes of the area and apparent stiffness of the bone-implant interface. A clear transition between loose and tight contact allowed the definition of thresholds that could potentially discriminate between a stable and an unstable stem. We also studied the effect of the broaching procedure and its relevance for P3D. The effect of broaching on bone microstructure at the bone-implant interface was analyzed using cadaveric samples and micro-computed tomography. A mapping of the stiffness of bone in contact with the implant was obtained with indentation on the same cadaveric samples.

Keywords

Modal analysis; hip prosthesis; vibration; primary stability; bone mineral density; indentation; broaching; trabecular bone.

Résumé

Ce travail de thèse avait comme objectif l'amélioration des outils de planning préopératoire tridimensionnels (P3D) pour l'arthroplastie totale de la hanche. Lors de l'utilisation d'implants sans ciment, une bonne stabilité primaire est requise pour obtenir une ostéointégration satisfaisante. Pour cela, une sélection appropriée de la taille et de la position de la prothèse est indispensable. En utilisant des images scanner obtenues par tomographie à rayon X de la hanche des patients, le chirurgien peut se servir du P3D pour faire la sélection de l'implant et anticiper sa position finale. Aujourd'hui, les méthodes de planning disponibles ne fournissent pas de critère mécanique qui pourrait refléter la qualité du contact os-implant.

Nous proposons une méthode pour l'amélioration du P3D basé sur une analyse vibratoire par éléments finis pour le calcul de paramètres mécaniques personnalisés et liés à la stabilité primaire. Nos résultats suggèrent que la réponse modale de la tige est très sensible aux changements de l'aire de contact et de la raideur apparente de l'interface os-implant. Une transition marquée du comportement modal associée à un ancrage plus ou moins bon nous a permis de définir des seuils qui pourraient potentiellement discriminer des implants stables et instables dans le cadre du planning.

Nous avons aussi étudié l'effet de la procédure de râpage et son possible impact sur le P3D. L'effet de la râpe sur la microstructure de l'os à l'interface os-implant a été analysé sur des pièces anatomiques à l'aide d'images de micro-tomographie à rayon X. Une distribution spatiale de la raideur de l'os en contact avec l'implant a aussi été obtenue par indentation des mêmes pièces anatomiques.

Mots-clés

Analyse modale; prothèse de hanche; vibration; stabilité primaire; mouvement proximal; indentation; râpage; os trabéculaire.

Contents

Abstract	ii
Résumé	iii
1 Introduction	1
1.1 Context and motivation	1
1.1.1 Total Hip Replacement (THR)	1
1.1.2 THR broaching and bone properties	4
1.1.3 Preoperative Planning	6
1.1.4 Vibration Methods - Implant Stability	9
1.2 Enhancement of 3D planning	13
1.3 Objectives of the thesis	14
1.4 Outline of the thesis	14
2 Numerical Model	17
2.1 Introduction - Finite Element Analysis (FEA)	17
2.2 Geometrical model	17
2.3 Mesh	20
2.4 Boundary Conditions (BC)	20
2.5 Registration of HU densities on the mesh	21
3 Modal analysis of clinical cases	23
3.1 Introduction	23
3.2 Materials and Methods	24
3.3 Results	28
3.4 Discussion	28
4 Modal analysis of controlled cases	31
4.1 Materials and Methods	31
4.2 Data Analysis	32
4.3 Results	33
4.4 Discussion	38
5 Characterization of broaching effect on bone-implant interface from μCT-Scan images	43
5.1 Introduction and Context	43
5.2 Materials and Methods	44
5.2.1 Overview of the protocol	44

5.2.2	Samples handling and preparation	46
5.2.3	3D Planning and selection of samples.	46
5.2.4	Preparation of samples.	47
5.2.5	μ -CT Scan image acquisition.	50
5.2.6	Broaching Procedure	52
5.2.7	Image Processing Procedure	53
5.3	Results	61
5.4	Discussion	62
6	Mechanical characterization of the bone-implant interface after broaching	67
6.1	Introduction	67
6.2	Bone Preparation and preservation	68
6.3	Overview of indentation testing	70
6.3.1	Sample mounting and testing devices	70
6.3.2	Definition of indentation spots	73
6.3.3	Mechanical test of indentation	73
6.3.4	Preliminary mechanical tests	78
6.4	Results	79
6.4.1	Results preliminary tests	79
6.4.2	Results of broached bone - study samples	82
6.5	Discussion	86
6.5.1	Analysis of contact stiffness results	86
6.5.2	Analysis of Young's modulus spatial distribution	87
7	Conclusion and Perspectives	89
A		
	Appendix: Modal shapes, clinical study	91
B		
	Appendix: Modal analysis, controlled study	93
C		
	Appendix: Broaching BMD spatial distribution, μCT-Scan images	95
D		
	Appendix: Broaching BMD angular variation, μCT-Scan images	99
E		
	Appendix: Results of indentation orthogonality test	109

Contents	vii
<hr/>	
Bibliography	111
List of publications and communications	117

CHAPTER 1

Introduction

1.1 Context and motivation

1.1.1 Total Hip Replacement (THR)

Total Hip Replacement is one of the most commonly performed and successful orthopedic surgeries nowadays, which consists of replacing the hip joint with a prosthesis. With over one million interventions worldwide per-year, and a high survival rate of over 95% at 15-20 years or more (Holzwarth and Cotogno, 2012; Karachalios, 2014), it has been appointed as the "orthopedic operation of the century" (Learmonth et al., 2007). However, the long-term success of this intervention is highly dependent on the quality of the contact between the bone and the implant achieved by the surgeon during the operation, which allows a proper subsequent osseointegration (Karachalios, 2014). The wrong selection of an implant's size and position by the surgeon can lead to bad contact conditions, jeopardizing the outcome of the surgery.

The hip joint (Figure 1.1) is one of the largest and more stable joints in the human body (Nordin and Frankel, 2001). It presents the characteristics of a classical ball-and-socket joint and is surrounded by powerful and well-balanced muscles, providing a remarkable intrinsic stability, but also a great range of mobility (Byrne et al., 2010), allowing the performance of daily activities such as walking, sitting, and squatting (Nordin and Frankel, 2001). It features the four characteristics of a synovial joint: it has a joint cavity; joint surfaces are covered with articular cartilage; it has a synovial membrane producing synovial fluid, and; it is surrounded by a ligamentous capsule (Byrne et al., 2010).

The hip joint is composed by the femoral head and the acetabulum of the pelvis Figure 1.1. The femoral head is the convex component of the ball-and-socket configuration of the hip joint, it forms two thirds of a sphere, and is covered by articular cartilage (Nordin and Frankel, 2001). The femoral head is attached to the femur shaft by the femoral neck, with an inclination angle that facilitates freedom for joint motion (Byrne et al., 2010; Nordin and Frankel, 2001). The acetabulum is the concave component of the ball-and-socket configuration of the hip joint, its surface is also covered with articular cartilage. The acetabulum becomes congruous with the femoral head when the hip joint is loaded (Nordin and Frankel, 2001).

Total hip replacement needs to be performed when the hip-femoral joint is permanently damaged and has to be replaced with a hip prosthesis. In this procedure, the head of the femur is removed to access the femoral canal and insert a

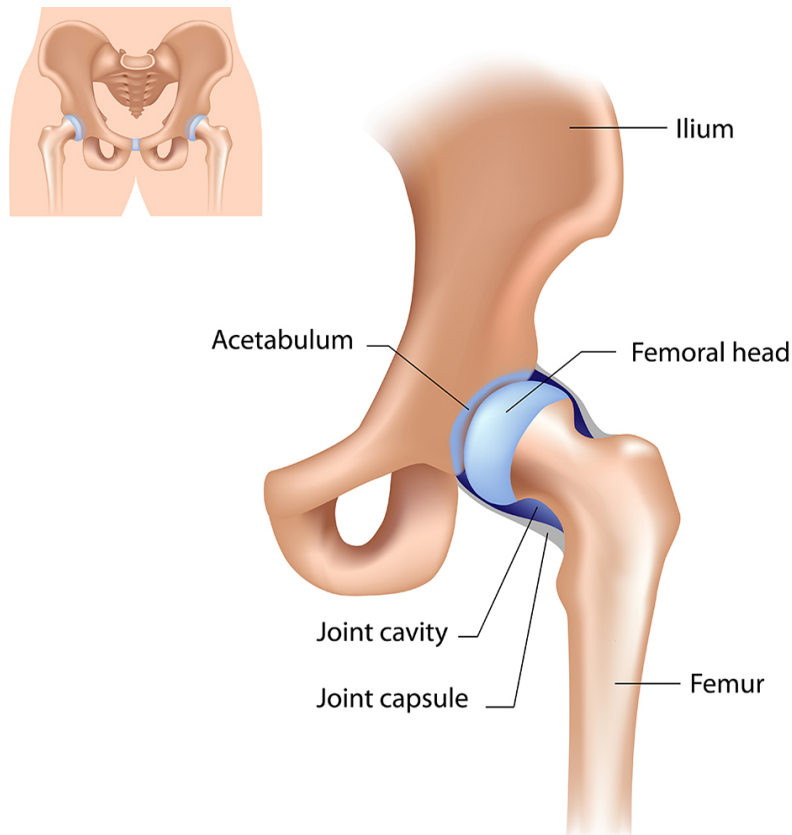


Figure 1.1: Anatomy of the hip joint. Source: www.corentec.com - hip anatomy

implant-stem which is then connected to an acetabular cup that goes inserted in the acetabulum of the hip bone (Figure 1.2).

In the current practice of THR, an increasing number of procedures are performed with cementless stems (Figure 1.3), especially when treating young patients with high activity level (Søballe, 1993; Holzwarth and Cotogno, 2012). This type of implant has shown to provide multiple advantages as opposed to cemented ones; first, cementless implants allow to avoid the introduction of cement in the organism of the patient that could generate the so-called cement disease, or polymethyl methacrylate debris, causing rejection reactions, premature loosening and other complications (Learmonth et al., 2007), they also help to match more properly the properties of the surrounding bone, thanks to the implementation of bioactive coatings and rough surface textures that cementless stems usually have incorporated to help enhance bone in-growth and fixation (Søballe, 1993; Søballe et al., 1992; Holzwarth and Cotogno, 2012; Karachalios, 2014). Among the most commonly used metal materials in orthopedic prostheses we can find: stainless-steel, cobalt-chrome, titanium and titanium alloy. Cementless hip prostheses made of a Ti alloy (Ti-6Al-4V) are characterized for having a high corrosive resistance, and has proven to be particularly

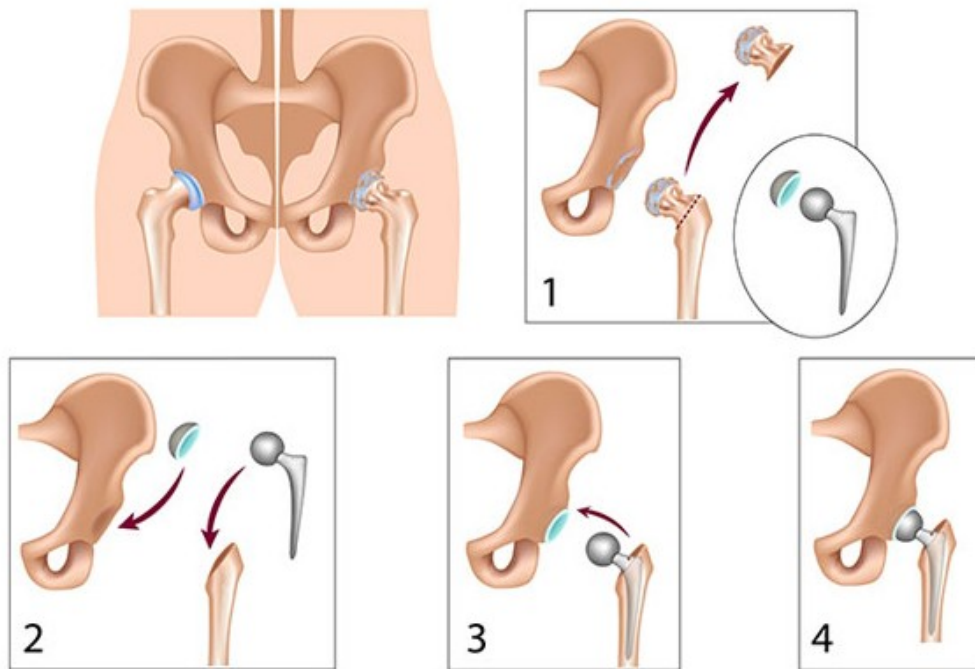


Figure 1.2: Total Hip Replacement Scheme. Source: www.drugwatch.com - hip replacements

biocompatible in comparison with other materials. One of the advantages of this material is that its mechanical properties adapt well to those of cortical bone, which helps reduce non-anatomical bone remodeling caused by stress shielding (Søballe, 1993).

The use of a cementless implant involves a press-fit condition between the stem and the femur that is crucial for a proper fixation, and the survivorship and good function of the joint replacement (Karachalios, 2014; Ramamurti et al., 1997). Obtaining a proper press-fit at surgery indicates that there is a good anchorage of the implant in the bone cavity (Karachalios, 2014; Ramamurti et al., 1997); this is a necessary conditions to obtain primary stability, which is defined as the mechanical fixation of an implant achieved at the time of the surgery (Karachalios, 2014). Primary stability, is paramount for achieving bone in-growth, also known as the osseointegration process guaranteeing good functional outcomes (Albrektsson and Albrektsson, 1987; Viceconti et al., 2006) especially in the early post-operative period.

There are multiple debates regarding the threshold of bone-implant relative motion that allows proper bone in-growth, it has been reported by multiple authors that there seems to be a relation between the magnitude of bone-implant motion and the type of interface tissue developed after surgery (Søballe et al., 1992; Bragdon et al., 1996). The formation of fibrous tissue is undesired since it is mechanically



Figure 1.3: Cementless hip stem without the femoral head -SPS Evolution Symbios.
Source: www.symbios.ch

unstable (Søballe et al., 1992). To obtain a proper bony in-growth, the movement of the implant within the bone, also called "micromotion" ((Karachalios, 2014)), should not exceed $150 \mu\text{m}$ (Søballe, 1993; Bragdon et al., 1996).

1.1.2 THR broaching and bone properties

At the macrostructural level, bone is differentiated into two different types, cortical or compact bone, and cancellous or trabecular bone (Figure 1.4).

Cortical bone composes the external layer of all bones, with a dense structure of low porosity (porosity usually lower than 15%), presenting a compact appearance at the macroscopic level (Mitton et al., 2011). One complication that affects this

Trabecular bone is found in the inner parts of bone, and presents a highly porous sponge-like appearance, with a 3D structure made of connected plates and rods, known as trabeculae (Mitton et al., 2011).

For the implantation of a hip implant, it is necessary to open the femoral canal by removing the trabecular bone and leaving an open access for the implant to penetrate. This step of the surgery is known as the broaching procedure, for this the surgeon uses a set of broaching tools of different sizes that are introduced pro-

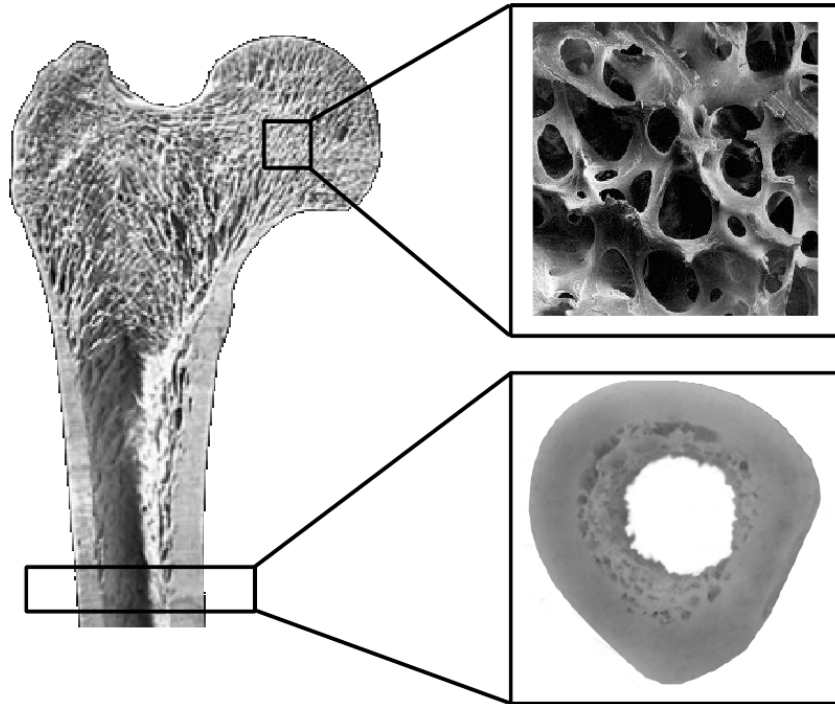


Figure 1.4: Structure of trabecular bone (up) and cortical bone (bottom). Source: M. Granke. Multi-scale investigation of bone quality using ultrasound. PhD Thesis

gressively in a size-increasing manner until obtaining the desired size of the cavity for implanting the stem (Figure 1.5). It appears obvious to infer that this broaching process would have a non-negligible effect on the mechanical properties of the trabecular bone, which would most likely affect the bounding conditions in the interface zone between the bone and the implant. Mechanical tests of indentation have been widely used for characterizing the mechanical properties of bone at different structural levels (Oliver and Pharr, 2004).

On the other hand, it has been demonstrated that the bone mineral density of the bone can be associated to its elasticity through different empirical equations (Keller, 1994; Wirtz et al., 2000; Helgason et al., 2008; Auperrin, 2009). Specifically in our context of interest, the Hounsfield densities can be extracted from computed tomography (CT) scan images of the bone to make a mapping of the mechanical properties of the bone after broaching by making use of those relations.

The Hounsfield density is a quantitative parameter that can be extracted from the CT-Scan images of the bone of the patient; it is expressed in Hounsfield units (HU), and it corresponds to a linear transformation of a measure of the attenuation coefficient of the X-rays and a normalization with respect to the attenuation coefficient of water. It is expressed by:

$$d_{HU} = 1000 \times \frac{\mu_X - \mu_{water}}{\mu_{water}},$$

Where d_{HU} , μ_X and μ_{water} are the Hounsfield density, the attenuation coefficient of the X-rays in the material in question (bone), and the attenuation coefficient in water. For standard pressure and temperature conditions, the Hounsfield density in water is zero and the Hounsfield density in air is -1000 HU (Aamodt et al., 1999), while for the cortical bone is between 400 and 1000 HU (Shapurian et al., 2006).



Figure 1.5: Broaching tools (Symbios®) of different sizes used for THR.

1.1.3 Preoperative Planning

THR is performed with the aim of recovering the biomechanical functionality of the hip joint when it's damaged, for this a very precise work has to be done during the surgery to recreate the original anatomical configuration of the patient. In cementless THR, the choice of the size and position of the implant for each specific patient is vital for obtaining the correct press-fit and primary stability (Reggiani et al., 2008; Holzwarth and Cotogno, 2012; Karachalios, 2014) previously described.

The implantation of the stem in the bone and the evaluation of the level of anchorage is commonly assessed by the orthopedic surgeons in a rather empirical fashion. According to communications with an experienced orthopedic surgeon and limited literature reference (BEGUEC et al., 2015) a common practice is to use the sound of hammer blows as an indication of the quality of the press-fit between the implant and the bone. This implies that the stem size, position, and attainable stability is usually assessed empirically by the surgeon in the operating room with an inherent risk of error. For instance an underestimation of stem size may lead to pain, lower limb shortening or dislocation, whereas an overestimation may generate bone fractures and limb lengthening (Knight and Atwater, 1992; Sariali et al., 2012a).

Radiographs (X-rays) are used as a preoperative two-dimensional template for planning the surgeries, and anticipating prosthesis size and possible complications. This technique however, has proven to be highly dependent on the level of experience of the surgeon, and leads to prediction errors of size and position of the implant in approximately 50% of the cases when using cementless implants (Knight and Atwater, 1992; Carter et al., 1995; González Della Valle et al., 2008; Sariali et al., 2012a) and originating problems such as lower limb discrepancy (Sariali et al., 2012a).

In order to assist the surgeons in making the correct selection of the prosthesis and plan the surgeries preoperatively, new tools are becoming available that allow to make a planning of the procedure more accurately, such as *HipPlan* and *HipOP* (Viceconti et al., 2003a; Sariali et al., 2009b, 2012a, 2016), this may in particular be of big help for the less experienced surgeons. Specifically, three-dimensionnal (3D) preoperative planning software, which are mainly based in anatomical compatibility techniques, make use of CT-Scan images of the hip joint of the patient and a 3D numerical model of the implant, allowing the surgeon to make a navigation with the digital model of the prosthesis. The surgeon virtually places the stem and the acetabular cup in the cavity of the femur and the acetabulum respectively, until finding the correct size and position for the implant, which is specified by a representation of the density of the bone projected on the surface of the stem's model (*HipPlan*®), Symbios, Yverdon-les-bains, Switzerland), (Figure 1.6). With these tools, the surgeon anticipates the final position of the stem in the bone cavity after the insertion by successive hammer blows (Sariali et al., 2009b). More precisely, the surgeon needs to decide whether the regions of contact between the stem and the bone, for a given model and size of stem, can ensure a satisfactory anchorage by press-fit. However, the surgeon only has visual and geometrical arguments to make a decision and needs some training to take benefit of the 3D planning. This among others, is seen as one of the reasons the preoperative planning is seldom used in clinical practice while it may significantly help reduce failures, as explained below.

A study performed using the 3D preoperative planning software *Hip-Op* on the accuracy of CT-based surgical planning for THR as compared to traditional 2D templating planning (Viceconti et al., 2003a), shows that the accuracy of the selection of the size of the stem and the socket increased from 83% for the stem and 69% for the socket to 86% and 93% respectively. Demonstrating an improvement on the accuracy of the planning, specially when deformed anatomies are involved, and showing a high precision and accuracy specially for less experienced surgeons.

Sariali et al. have performed several studies on the accuracy of 3D preoperative planning using the *HipPlan* software. In a study to evaluate the accuracy of reconstruction of the hip using 3D preoperative planning and cementless implants (Sariali et al., 2009b), 223 patients with osteoarthritic hips were analyzed using the 3D planning tool. The post-operative restoration of the anatomy was assessed by

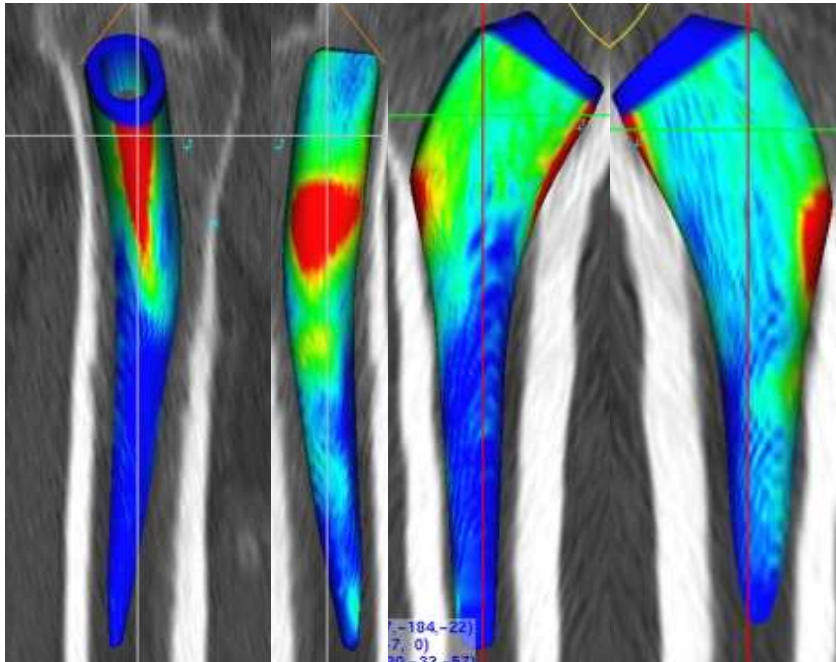


Figure 1.6: 3D preoperative planning - HipPlan.

CT and compared with the pre-operative plan, with accurate results in 86% of the cases for the acetabular component, 94% for the stem, and 93% for the neck-shaft angle. They conclude that the method appears to provide high accuracy, as the difficulties that can be found at the moments of the surgery can be anticipated and solved pre-operatively.

In another study (Sariali et al., 2009a) to determine 3D morphological data of the hip focusing on femoral offset (defined as the distance between the center of the femoral head and the femoral axis (Sariali et al., 2009a)) and using the software *HipPlan*, the mean femoral offset was found to be 2.2 mm greater than the 2D femoral offset values reported in the literature, the authors conclude that 3D planning software could allow an optimization of the planning process and the design of hip prostheses.

Given the potential that 3D planning tools seem to have for the improvement of THR, the interest for the advancement of techniques for these planning tools appears to be increasing in the last few years.

One study attempted to use anatomical compatibility and data set registration techniques for automated positioning of the hip implant based on predefined positions from 3D preoperative plans done by surgeons, the method produced good results for implant positioning when compared to manual positioning done by an experienced surgeon (Viceconti et al., 2003b).

Another study proposed an atlas-based approach for automated 3D preoperative planning for THR (Otomaru et al., 2012). Statistical atlases were constructed from a number of 3D preoperative plans performed by experienced surgeons; based on distances map representing the preference of bone-implant contact patterns of the surgeon, 40 cases were evaluated utilizing the automated technique, and errors were measured as differences between the automated and a surgeon's plan. By using the automated method positional and orientation errors were reduced as compared to other planning techniques, particularly 2D template methods.

1.1.4 Vibration Methods - Implant Stability

In this study we propose the use of vibration methods for the analysis of stability of cementless hip prosthesis during preoperative planning. In other words, we have combined 3D planning with a vibrational analysis to enhance the planning. Various studies have been carried out by multiple authors during the last few decades on the implementation of vibration methods perioperatively (during surgery) for the analysis of stability of hip prostheses and other types of implants, revealing promising applications of this technique for stability assessment pre and perioperatively. We have identified two main research groups that have been consistent throughout the years in the advancement of this technology and have inspired some of our study ideas, they are the team of Pastrav et al. from Leuven Engineering University College, Leuven, Belgium, and the team of Viceconti et al. from the University of Bologna and Rizzoli Orthopedic Institute, Bologna, Italy. The following presents a summary of some of the works of these and other authors:

1.1.4.1 Experimental studies:

Various experimental studies have been proposed with the goal of shedding light on the applicability of vibration methods for the analysis of stability of hip prostheses.

Pastrav et al. (2009b) and Varini et al. (2010) proposed systems and protocols for perioperative assessment of stability of hip prostheses.

Pastrav et al. (2009b) developed a system to measure in-vivo the frequency response functions of the stem-femur system corresponding to successive insertion stages on the implant with the goal of detecting the insertion end-point of non-cemented and partially cemented hip stems. They observed that the higher mode numbers (frequency range 0-10 kHz) are more sensitive to the stability change compared to the lower mode numbers, in agreement with numerical studies Pastrav et al. (2009a), and also that during the insertion of the implant in the femur, the changes of boundary conditions and implant stability between different stages are reflected by the resonance frequency evolution (Figure 1.7).

Varini et al. (2010) presented a study focusing on an in-vitro validation of a device to measure implant stability perioperatively based on vibration analysis. Fresh cadaver specimens and composite samples were used for the study. The device was composed by an excitatory piezoelectric system that delivered a controlled excitation to the prosthesis [1200-2000 Hz], and an accelerometer mounted on the host bone measured the transmitted vibration to identify resonance frequencies, which were measured immediately after press-fitting. Simultaneously a torque was applied to the implant and bone-implant micromotions were measured with the use of a displacement transducer. With this vibration technique they were able to discriminate between different levels of stability, concluding that the highest peak in the excitation range due to torque application is the best indicator of implant stability, and that when that shift is less than 5 Hz during the application of the torque, the residual micromotion after removal of the load was always less than 150 μm , which has been identified in other studies as the threshold for a correct implant anchorage (Søballe, 1993; Bragdon et al., 1996).

In terms of loosening detection techniques, Puers et al. (2000) developed an implantable telemetry system for the detection of hip prostheses loosening by applying vibration analysis techniques. With an accelerometer placed in the head of the hip prosthesis, they monitored the response of the femur-prosthesis system to mechanical sine wave vibrations applied by an electromagnetic shaker at the distal end of the femoral bone. The author claims satisfying preliminary results with cadaver experiments, although no specific data is reported.

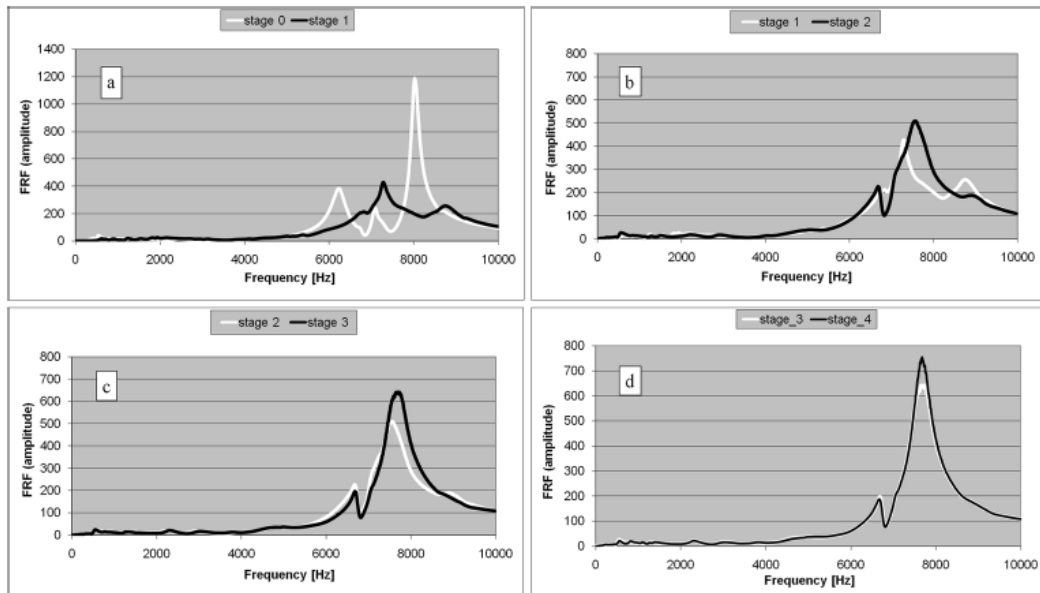


Figure 1.7: Frequency response function graphs corresponding to successive insertion stages of a non-cemented stem. Each successive stage follows a hammer blow.

1.1.4.2 Numerical studies:

Qi et al. (2003) implemented a numerical modal analysis using finite element methods and computer simulations to determine how much information a vibrational technique can reveal regarding the loosening of the femoral component of a total hip reconstruction. They computed and observed the first ten natural frequencies and mode shapes (Figure 1.8, right) of the implant-femoral model under free vibration, with hypothetical absence of contact portions at specific locations (Figure 1.8, left), and presented the interface failure size as a quantitative measurement of the femoral prosthetic loosening. They observed variations of the effect of interface failure (absence of contact) on the stiffness of the femoral component with different location and sizes of the failure zone, finding that higher modes are more sensitive to interface failure, and that the method was able to properly detect loosening when the size of interface failure was more than one-third of the length of the stem.

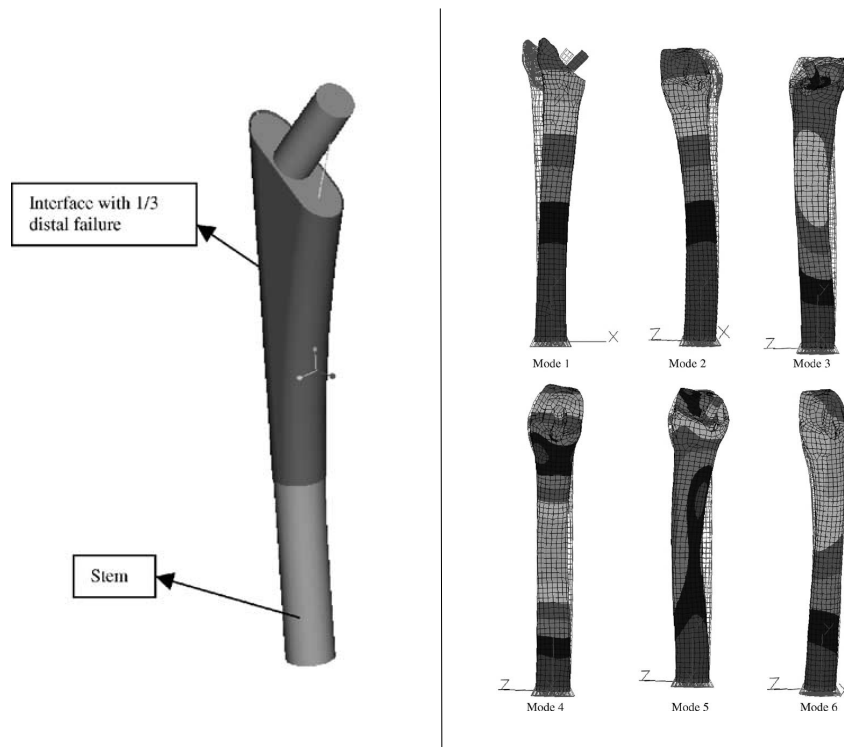


Figure 1.8: Example of hypothetical interface failures, 1/3 distal interface failure (left). First 6 vibration modes of the control model (right). Reproduced from Qi et al. (2003)

Pastrav et al. (2009a) performed a finite elements modal analysis on the hip stem-femur system under various contact situations (Figure 1.9, top) simulating different stages of the insertion of the implant in the bone's cavity, and observed variations in modal shapes and natural frequencies. In agreement with Qi et al. (2003), their

results show that a shift to higher frequencies correspond to an increment of the implant-bone contact surface, with a more pronounced effect on higher modes. They also observed that the dynamic behavior is most influenced by proximal contact changes (Figure 1.9, bottom).

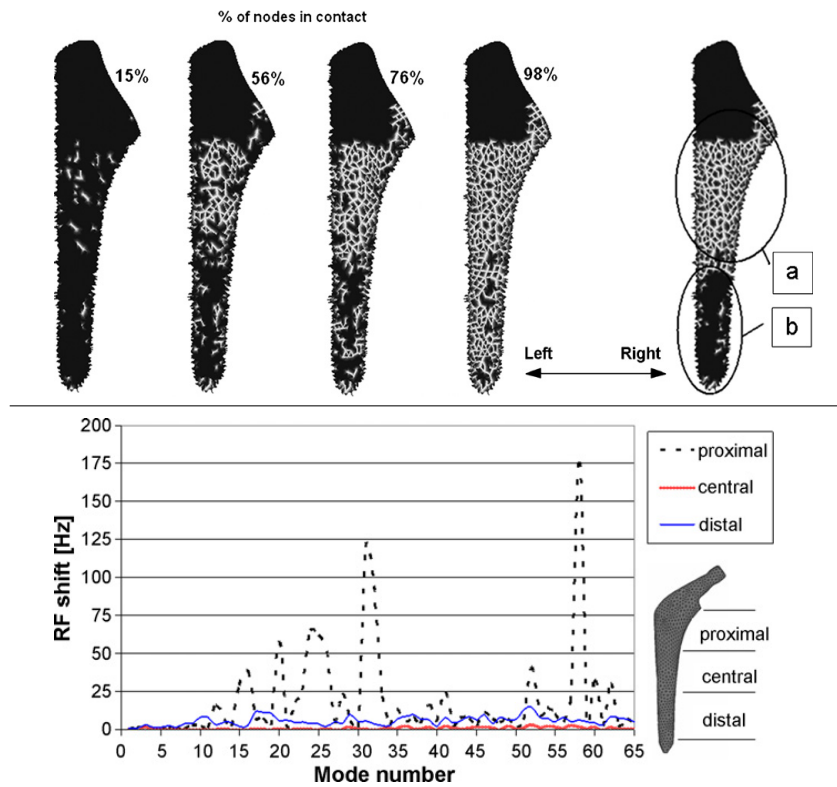


Figure 1.9: Top: Change of contact distribution: progressive increase of general contact (left); different contact areas in different zones; (a) proximal and central zones; (b) distal zone (right). Bottom: Resonance frequency shift plotted for proximal, central and distal contact increase (38-98%), free-free suspension of the implant-femur system. Reproduced from: Pastrav et al. (2009a)

In a similar study, Perez and Seral-Garcia (2013) determined the variations in the numerical modal analysis of a cementless hip prosthesis simulating different stages of the osseointegration process. Natural frequencies and modal shapes were observed under vibration for different bone and implant material properties and also different contact conditions at the bone-implant interface. It was found that as the osseointegration process evolved, increasing the contact surface and stiffness in the bone-implant interface, the values of the natural frequencies also increased in agreement with observations of Qi et al. (2003) and Pastrav et al. (2009a), and concluding also that higher modes and their corresponding resonance frequencies are more sensitive to contact conditions in the interface.

As evidenced in the aforementioned studies, vibration analysis has been considered and proven to have good potential as a mean to assess primary stability of hip stems. It has been demonstrated that the vibrational behavior of the stem is modified when the stem is progressively inserted into the femoral cavity by successive surgeon-controlled hammer blows. More precisely, resonant frequencies of the first vibration modes converge to plateau values as the stem's end-point of insertion is reached.

For 3D planning purposes, Reggiani et al. (2007) showed that a finite element (FE) model built from the CT-scan of a cadaveric femur could predict the level of primary stability achieved for a cementless stem. Their analysis is based on the simulation of the quasi-static torsion of the stem and the computation of torsional micromotion. The model, which incorporates a finite element mesh of the bone and frictional contact conditions, is quite realistic but as a counterpart has several parameters and requires relatively large computational resources. Our hypothesis is that primary stability can be assessed during planning by resorting to a somewhat simpler model based on the modal analysis of the stem.

1.2 Enhancement of 3D planning

Even though currently available 3D preoperative planning tools represent an important step forward for the advancement of THR techniques, they are still in early stages of development. One critical limitation that has been identified in these tools is the lack of relevant mechanical criteria that is used to guide the surgeon during the planning. As it can be observed in Figure 1.6, the software only provides visual information obtained from the levels of density of the bone in contact with the numerical object of the implant, but it does not specify the mechanical implications of the cartography observed, that is, what do those colors actually say about the global quality of the press-fit of the bone-implant interface?

The definition of this mechanical criteria is at the core of this thesis project, and represents an important part of the contribution of this work for the enhancement of 3D preoperative planning techniques.

In this thesis work, the technique that we propose is based on the implementation of a finite element method for performing a modal analysis of the stem for the assessment of primary stability of cementless hip implants, with the purpose of determining numerical indicators that can be used to discriminate between stable and unstable cases during preoperative planning. In short, we introduce resonance three-dimensional planning (RP3D) as a mean to assess primary stability preoperatively.

An exploratory preliminary study was performed using clinical data to identify from real cases common markers of stability discrimination. Then, in a study of

controlled cases those same markers served to identify the typical boundary conditions necessary to achieve stability. One advantage of our technique lays on its simplicity, since only the implant is included in the geometry of the finite element model (i.e no need to mesh the bone).

In the other hand we studied the effect of the broaching procedure on the bone, to this date this effect has not been defined and characterized, and any efforts towards the implementation of 3D preoperative planning techniques seem to be incomplete without a full understanding and consideration of the real contact conditions in the bone-implant interface, determined by the properties of the bone at the moment of the implantation, i.e. bone surface after broaching.

The existing 3D preoperative planning software make use of CT-Scan images of the patient before surgery, which evidently have not been through the broaching process yet. As a result, the planning obtained is based on a mere approximation of the actual contact conditions, since the real bone properties in the interface after broaching are not taken into account, this approximation may be far from reality depending on how important the effect of the broaching process on the bone surface is. On that account, it appears necessary to quantify the effect of the broaching process on the mechanical properties of the contact surface of the bone, to determine whether or not an approximation without taking into account the broaching effect is accurate enough for obtaining a realistic planning.

The potential of vibration methods for stability discrimination in THR has been established numerically and experimentally. Now, there is an interest for investigating the usefulness of this technique in the specific context of preoperative planning, and to establish the considerations related to the real boundary conditions in the bone-implant interface due to the effect of the broaching process.

1.3 Objectives of the thesis

- Introduce resonance three-dimensional planning (RP3D) as a mean to assess primary stability preoperatively; and evaluate the sensitivity and applicability of the method.
- Determine how, and to which extent, preoperative CT-Scan information can be used for RP3D. Define what is the relation between preoperative bone mineral density and the actual bone-implant contact.

1.4 Outline of the thesis

Chapter 2 introduces the finite element model, and numerical simulation considerations, taken into account for the vibrational analysis of the stem for stability

discrimination.

Chapter 3 presents an exploratory preliminary study based on clinical cases, as our first attempt to use the numerical vibration technique for identifying discriminatory factors between stable and unstable cases from the modal response of the stem.

In **Chapter 4** we present a fully developed vibrational finite element study based on controlled cases of bone-implant contact conditions for the definition of stability thresholds.

Chapter 5 is concerned with the characterization of the effects on bone properties of the broaching procedure by implementing image analysis techniques to measure bone mineral density variations on the μ CT-Scan images of cadaver samples before and after broaching.

Chapter 6 presents a study of the mechanical properties of the bone by implementing an indentation mechanical testing on cadaver bone samples at the surface of the broached cavity.

CHAPTER 2

Numerical Model

2.1 Introduction - Finite Element Analysis (FEA)

This chapter is dedicated to present the numerical model and FEA methods implemented in the context of our study.

A finite element (FE) modal analysis was conducted on the software of numerical simulations and analysis *Code Aster* (Code_Aster, EDF R&D, license GNU GPL, <http://www.code-aster.org>) implementing the Sorensen method for modal computation. The outputs of the computation are the modal frequencies and modal shapes calculated in the frequency range [0 – 21 kHz].

A *.comm* file is created, which contains the algorithm with the specifications of the FEA to be performed, including: FEA method, areas of affectation (nodes and elements to be affected), mechanical properties of the object, boundary conditions, stiffness matrix (corresponding in our case to the contact stiffness on the bone-implant interface) among other parameters depending on the desired outputs.

Salome-Meca (Salome-Meca, EDF Open Cascade, license GNU GPL, <http://www.salome-platform.org/>) was used to visualize the modal shapes. Code_Aster results were post-processed with custom Matlab (MATLAB Release 2015a, The MathWorks, Inc., Natick, Massachusetts, United States.) programs.

More detailed information regarding the FEA performed in each specific study will be presented in chapters 4, and 3.

2.2 Geometrical model

A finite element mesh was created for a cementless stem (SPS®, Symbios, Yverdon-les-bains, Switzerland), see Figure 1.3. Meshes of two different sizes were created for each side, left and right, for a total of four meshes. Size C: height 11.5 cm, length 3.4 cm, and width 2.5 cm. Size D: height 12.2 cm, length 3.6 cm, and width 2.6 cm. The stem is a cementless anatomic model with a metaphyseal proximal fixation which is made of titanium alloy Ti6Al4V-Iso 5832-3, assumed isotropic and linear elastic, with Young Modulus 114 GPa, Poisson ratio 0.34 and density 4500 Kg/m³. A CAO file (.ply format) of the stem, Figure 2.2, was provided by the manufacturer and used to create the FE mesh.

The CAO objects of the stem (provided by Symbios) contained small geometrical details (such as engraving) and could not be used as such to create a mesh. Therefore, the CAO file was first processed to remove small details which have a

negligible effect on the vibrational behavior in order to obtain a regular well conditioned mesh. Furthermore, in order to control the mesh density a parameterized geometry was created.

In order to do this, first, 15 cross-section contours were extracted from the CAO file (Figure 2.1). The contours selection process comprehends several steps since the nodes on the surface of the stem in the CAO file are not evenly distributed, which makes the extraction of the contours a little more laborious. To do this, three points per contour are selected directly on the surface of the object. With these three points the equation of the plane in which that contour is contained is obtained, then a tolerance value is manually assigned to each contour plane equation to include points that are located in adjacent planes of the CAO object and be projected on the plane of interest to fill the holes of areas where there are no points due to the uneven distribution of the original mesh (Figure 2.1). An interpolation is done to put all the points on the same contour line, to finally obtain a complete contour representative of the geometry of that part of the stem (Figure 2.2).

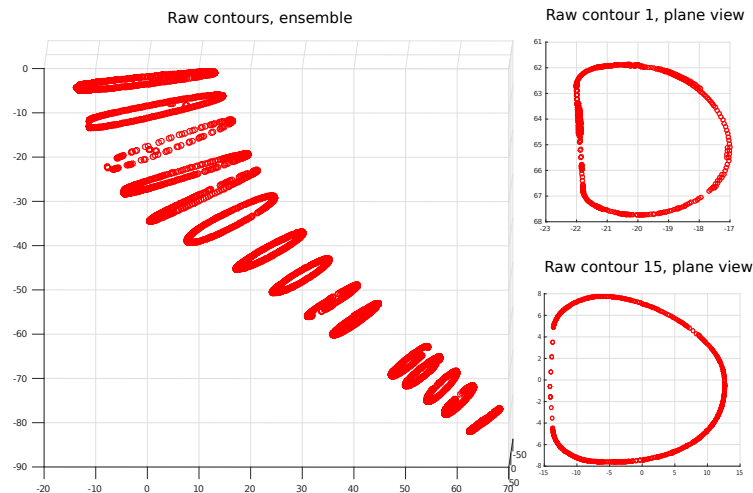


Figure 2.1: Visualization of the 15 contours in raw state, extracted from the CAO object. Left: ensemble of all 15 contours. Right: Plane view of contours 1 and 15.

Once the desired contour shapes are obtained, a new discretization is performed to obtain points evenly distributed over the contour by verifying consistency with the Pythagorean theorem, with the hypotenuse equal to the desired mesh element size (e). Then, the points are connected by lines to create a geometry file (.geo format), with the implementation of an algorithm adapted from a master's thesis (Vallet, 2013), see Figure 2.3. This was then imported into the meshing tool GMSH (Geuzaine and Remacle, 2009) to create the mesh of the stem. For the obtained element size (e) the mesh consisted of ≈ 24000 degrees of freedom, and ≈ 22500 tetrahedral second order elements (Figure 2.4).

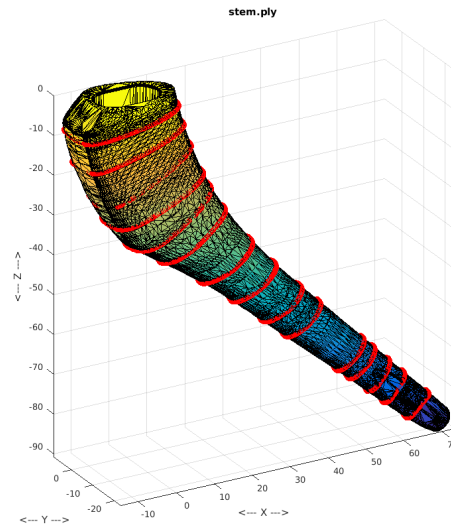


Figure 2.2: Visualization of the 15 contours after interpolation and reorganization, represented over the original CAO object.

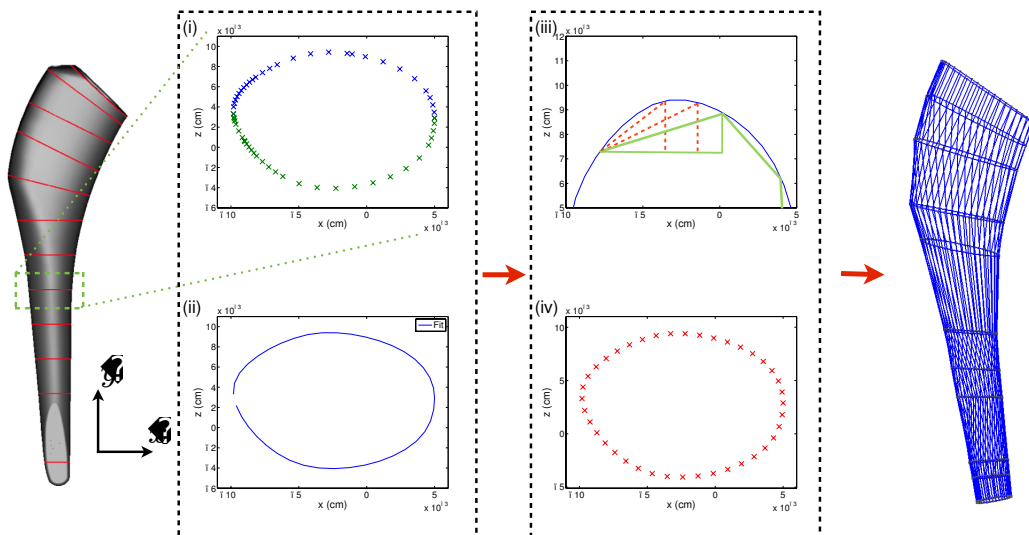


Figure 2.3: Successive steps for the construction of the mesh of the implant from the CAO object: (i) Extraction of contour points from the CAO object (ii) Interpolation of the contour (iii) Testing of points verifying Pythagoras's theorem, with hypotenuse equal to the desired element size (iv) Cloud of equidistant points forming the origin contour that is saved into a file format to be interpreted and processed on *gmsh*

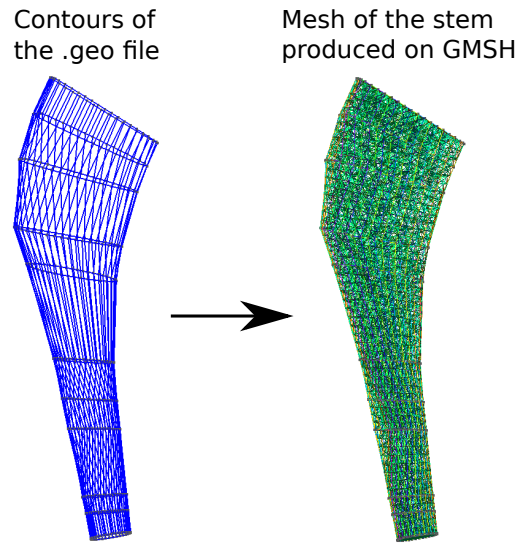


Figure 2.4: Left: Illustration of the contours saved into a .geo file format to be interpreted and processed on *gmsh*. Right: Mesh of the stem obtained on *gmsh* from the .geo file.

2.3 Mesh

In order to determine the appropriate mesh size, a convergence study was performed on a cantilever beam for which an analytical solution of the eigen-modes is available.

For this convergence study we took into account the cantilever beam theory and Newton's equation. Three different boundary condition (BC) configurations were considered for the cantilever beam, embedded-free, double-embedded, and free conditions.

The cantilever beam presented the following geometrical characteristics: $5 \times 0.2 \times 0.1$ cm ($L \times h \times b$). And mechanical properties: $E=210$ GPa (Young's Modulus), $G=79.3$ GPa (shear modulus); $\rho=7800$ Kg/m³ (volumetric mass). The second order mesh had 9286 degrees of freedom, and 5024 tetrahedral elements (Figure 2.5, a).

The eigen-modes of bending, torsion, and longitudinal motion were evaluated for each BC configuration on *Code Aster*. We selected a number of elements per wavelength of 16, which satisfies the Courant-Friedrichs-Lewy (CFL) condition, with an average error of 0,093% between the FE solution and the analytical result for the first seven eigenmodes, with the embedded-free configuration (Figure 2.5, b); this corresponds in our study to a characteristic element size of $e = 2$ mm.

2.4 Boundary Conditions (BC)

In our modal FEA studies, the boundary conditions are given by the stiffness in the bone-implant interface zone, which is simulated by springs attached to nodes on the

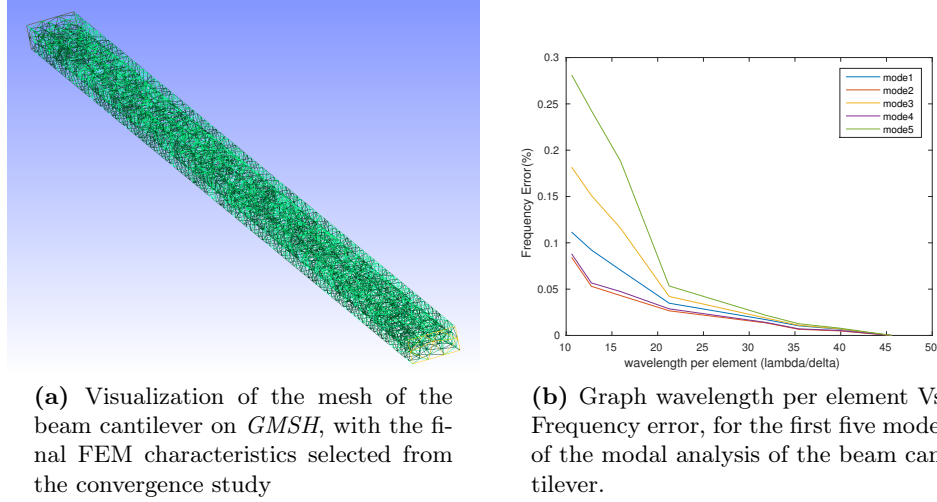


Figure 2.5: Beam cantilever convergence study

surface of the stem (Figure 2.6). Some nodes are affected by this stiffness, and the rest of the nodes are free.

The reaction force on node i of the stem writes:

$$F_i = k_i * u_i \quad (2.1)$$

where k_i is the stiffness of an individual spring and u_i is the displacement vector of the node i .

The variable stiffness K (the equivalent stiffness of the whole contact surface) is applied perpendicularly to the contact surface of the mesh of the stem, and distributed homogeneously over the surface in question by adjusting k_i . A study was done with a simple beam cantilever to verify that the stiffness is in fact distributed homogeneously on the surface and not applied individually to each node.

Different approaches of this same method are used for the FE studies in Chapters 4, and 3, for representing the interface stiffness that corresponds to each study.

2.5 Registration of HU densities on the mesh

The current 3D preoperative method is a black-box, the relationship between what happens in the bone-implant interface and the visual information of the HU is unknown. We have started to work on the creation of a color map with our own mechanical criteria directly from the preoperative planning.

From the 3D planning we obtain a cloud of points with an associated HU density, in order to convert these HU densities into boundary conditions for the FEA, these density values need to be associated to its corresponding node on the mesh.

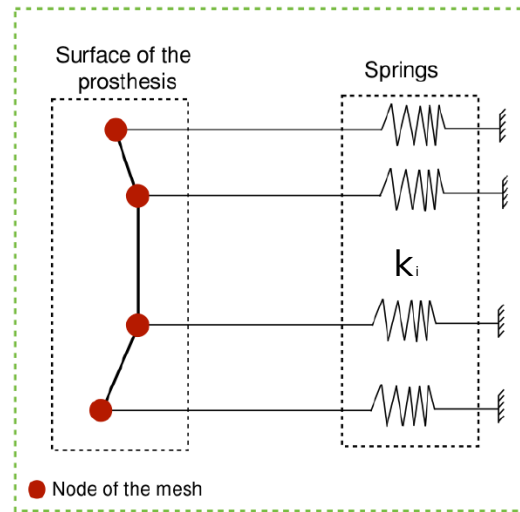


Figure 2.6: Springs stiffness effect attached to the nodes of the stem.

Different techniques were proposed for this association of values to each node, among them: the values contained in a normal of a certain length on each node, the values within a certain radius, and the nearest value, see figure 2.7 for an example; we observe how the distribution changes according to the registration method implemented. One difficulty for the application of these methods is that the mesh obtained from the CAO object of the stem and the cloud of points obtained from the 3D planning are expressed in different coordinate systems, and a transformation matrix is needed to make the right registration, this matrix defined in the 3D planning software is not easily accessible. For the moment this registration is done manually.

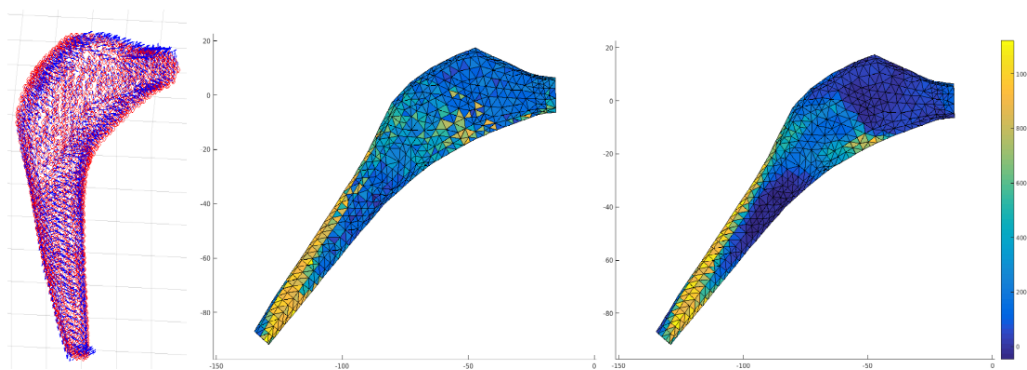


Figure 2.7: Registration of HU values from the 3D planning on the FE mesh. Left: Illustration of normals defined on each node for association of HU values. Middle: example of an HU density distribution with the "nearest value" method. Right: example of an HU density distribution with the "nvalues within a radius" method

CHAPTER 3

Modal analysis of clinical cases

3.1 Introduction

In this chapter we present an exploratory study dedicated to assess the applicability and advantages of implementing numerical modeling methods to analyze the vibrational behavior of a cementless hip implant for the determination of primary stability in preoperative 3D planning. Based on a few clinical cases, and making use of the numerical model presented in 1; we present the application of a modal analysis of the stem, specifically modal frequencies and modal shapes, subjected to boundary conditions defined by the contact with the surrounding bone in the femoral cavity, obtained from CT-Scan information of a 3D planning.

As presented in chapter 1, multiple studies ((Qi et al., 2003; Pastrav et al., 2009a,a; Varini et al., 2010; Perez and Seral-Garcia, 2013), among others) have been presented proposing different vibration techniques for the analysis of stability in THR, both preoperatively and perioperatively. These experimental and numerical works propose various methods for the discrimination of stability defined as a function of the frequency response of the bone-implant system, and the mode shapes. It has been demonstrated that a shift towards higher frequencies is related to a better stability. Furthermore, these studies have shown how this enhancement of stability is due to an increase in the contact surface and the quality of the anchorage of the implant in the femoral cavity.

Our approach has two main advantages which shape the originality of this work. Firstly, we associate the HU densities from CT-Scan images of the bone with stiffness values, this allows to implement a simple model which involves attaching springs to the contact area of the stem with their corresponding stiffness. This way we simulate the effect of contact with the bone without having to include the bone in the geometrical model. And second, we establish a relation between indicators of instability from the numerical analysis and clinical indicators of unstable patients (i.e. patients in pain post-surgery).

Our hypothesis is that the modal analysis, namely modal frequencies and modal shapes, of the implant under boundary conditions obtained from the preoperative planning can serve to discriminate stable and unstable cases.

3.2 Materials and Methods

Figure 3.1 displays the main steps that were followed for the completion of this exploratory numerical study. First, CT-Scans of each patient were acquired before the surgery, the CT-Scanner was calibrated to maintain consistency with the scans after surgery. The preoperative CT-Scan images were used for the 3D preoperative planning performed by the orthopedic surgeon. These plannings were used as a reference for performing the THR surgery by the same surgeon. Post-surgery 3D plannings of six patients were used for the numerical study. These post-surgery plannings were used to superpose and verify the position planned with the preoperative planning CT-Scan images of the patient, and make sure that the planned position was achieved. Also, these plannings are done after the surgery to run the numerical study with the bone-implant conditions obtained after the surgery is performed. The finite element modal analysis was done on *Code ASTER* following the method described in chapter 2.

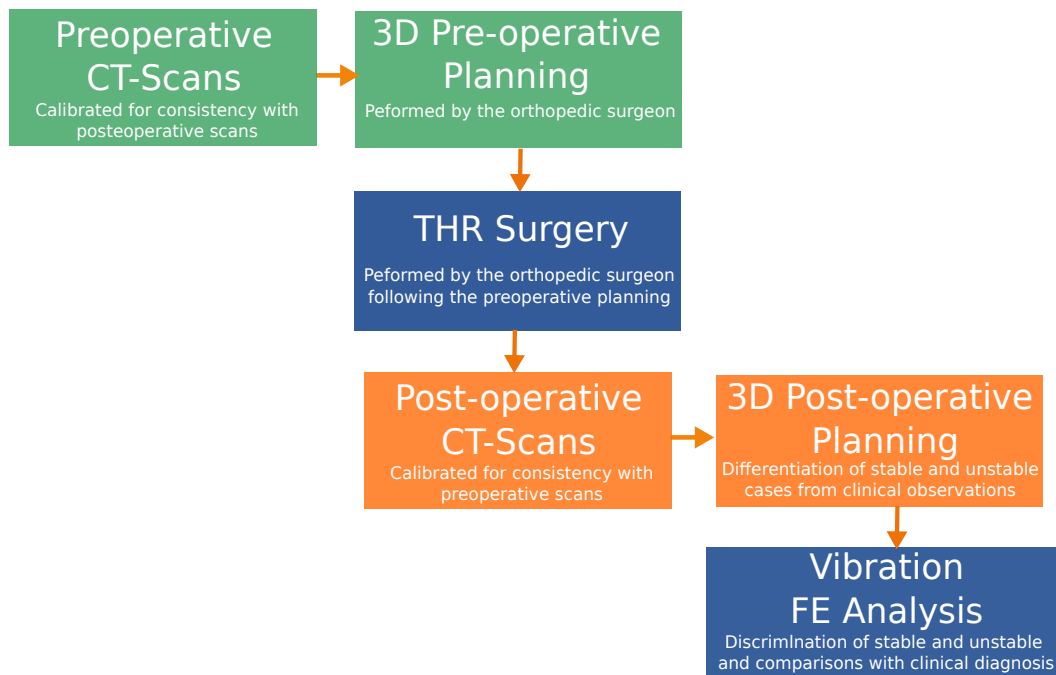


Figure 3.1: General scheme with the different steps of the procedure

Presentation of study cases

The six cases (Hôpital Pitié Salpêtrière, Orthopedic Service Department) were selected by the surgeon and classified as stable or unstable, by taking into account common clinical parameters, such as the presence of pain, limping, difficulties to switch from sitting position to standing position, or the inability to walk. The first

group (stable) exhibits a good osseointegration of the implant in the bone three months after the operation, while the second group (unstable) is formed by patients for whom the implant did not attain the stability condition as observed several months after the surgery.

The first group (patients A, B and C) correspond to a good osseointegration and a satisfactory implant-femoral stability, while the second group (patient E and F) present unstable implants with an insufficient level of anchorage of the implant in the femur. Finally, patient D was classified as having a good implant stability but presenting post-surgery pains. The six plannings are presented in table 3.1.

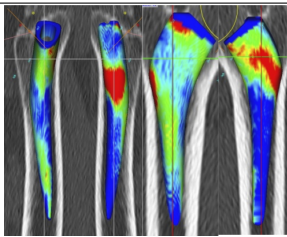
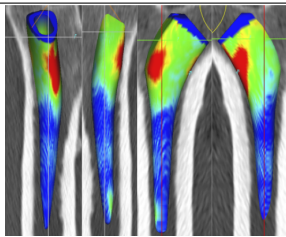
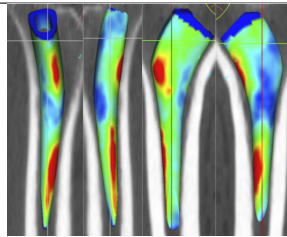
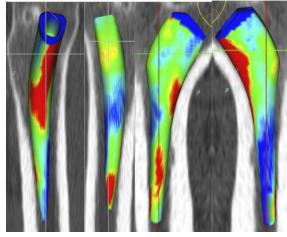
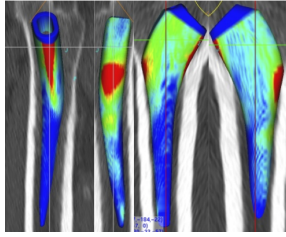
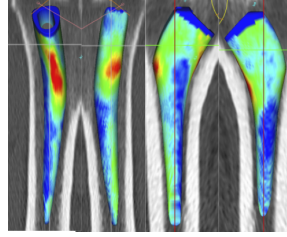
	Patient A - stable	Patient B - stable	Patient C - stable
P3D			
	Patient D - stable with pain	Patient E - unstable	Patient F - unstable
P3D			

Table 3.1: Images taken from the postoperative three-dimensional plannings (P3D) of patients A - F. The plannings of patients A, B, C and D correspond to stable prostheses, with presence of pain for patient D, the plannings of patients E and F correspond to unstable prostheses.

It should be noticed that patients A, B, C, D and F were operated with the same prosthesis model SPS® modular (Symbios), size C; left side for patients A and D, and right side for B, C and F. Patient E was operated with a size D implant, right side.

Extraction of boundary conditions from the 3D planning

In this chapter we deal with the issue of converting Hounsfield density values of the bone in contact with the stem obtained from CT-Scan images of the patients in the planning, into a physical parameter that simulates the effect of the contact conditions in the bone-implant interface. For this, we apply the following reasoning, with the introduction of the implant into the femoral canal, a displacement of the

bone is imposed by a force exerted by the implant. The relation between this force and displacement is given by the apparent stiffness of the bone-implant interface. Hence, the physical parameter we search to convert the Hounsfield values into, is nothing but the contact stiffness in the interface.

From the work of Auperrin (2009) we obtain an equation to relate the Hounsfield density measured by X-rays and the volumetric mass of the bone. This relation is given for a volumetric mass equivalent to those we deal with in our study.

$$\rho = 0.0009d_{HU} + 0.8336 \quad (3.1)$$

with ρ the volumetric mass, and d_{HU} the Hounsfield density.

In multiple studies it has been established that the Young's modulus can be related to an apparent volumetric mass of the bone (Keller, 1994; Wirtz et al., 2000; Helgason et al., 2008). For this study the following relation was implemented:

$$E = 10.5 \times (0.55\rho)^{2.29} \quad (3.2)$$

Where E (GPa) and ρ ($g.cm^{-3}$) are the Young's modulus and the apparent volumetric mass of the bone, respectively. This expression was obtained from the studies of Keller (1994) regarding relations between elastic properties and the volumetric mass of the femur.

With equation 3.2 we can calculate a local Young's modulus for different zones of the prosthesis associated to different HU values. It follows that, for a determined thickness of the femoral bone e , a stiffness K can be obtained for different zones of contact, by implementing the following equation:

$$K = E_{HU} \times \frac{S}{e} \quad (3.3)$$

with K ($N.m^{-1}$) the equivalent stiffness (see relation with equation 2.1 in chapter 2), E the Young's modulus (Pa), S (m^2) the corresponding area of the contact zone in question, and e the considered thickness in the bone-implant interface.

Equation 3.3 is derived from the following reasoning:

$$\begin{cases} F = k \times x \\ \sigma = E \times \varepsilon \end{cases} \Rightarrow \begin{cases} \sigma = \frac{F}{S} \\ \varepsilon = \frac{x}{e} \end{cases} \Rightarrow \begin{cases} E \times \varepsilon = k \times \frac{x}{S} \\ E \times \frac{x}{e} = k \times \frac{x}{S} \end{cases} \Rightarrow k = E \times \frac{S}{e}$$

with F an applied force, on an element of length e , and surface S , causing a displacement x , originating an strain ε , and a stress σ .

Definition of contact surfaces

The 3D preoperative planning tool that we used (HipPlan, Symbios) allows to extract the values of the Hounsfield density of the bone in contact with the implant from the preoperative QCT scan of each patient.

On the 3D planning every point on the surface of the implant is associated to a value of Hounsfield density.

A linear scale of Hounsfield densities is established, first a lower threshold of 400 was defined for the HU densities, which corresponds to the minimum HU density of cortical bone which was set in the range of 400 to 1000 (Shapurian et al., 2006). The points of the surface of the implant associated to HU densities below 400 would be considered as free of contact.

The Hounsfield densities are converted into volumetric masses with the equation 3.1. Then a scale of volumetric mass is established by defining three different ranges as shown in Figure 3.2 (left), which correspond to the assumed level of contact between the prosthesis and the bone, low contact in blue, medium contact in green, and high contact in red.

These three ranges of volumetric mass, for different contact areas are defined as follows:

$$D = \max(\rho) - \min(\rho) ,$$

$$\begin{cases} \rho_{blue} \in [\min(\rho) ; \min(\rho) + D/3] , \\ \rho_{green} \in [\min(\rho) + D/3 ; \max(\rho) - D/3] , \\ \rho_{red} \in [\max(\rho) - D/3 ; \max(\rho)] , \end{cases}$$

These three ranges of volumetric mass allow to define three groups of points on the surface of the implant corresponding to three levels of contact (Figure 3.2, left). The volumetric mass of one zone corresponds to the average of the volumetric masses of the points of the associated range. The local values of stiffness for each zone are then calculated by using the equations 3.2 and 3.3.

The proposed contact model consists of attaching one spring representing a local stiffness (Figure 3.2, middle) to each one of the nodes of the mesh located on the three contact zones (Figure 3.2, right).

To calculate the area of each of the three contact zones, we calculate the individual areas of each surface element of each contact zone. These are computed as the area of a triangle formed by one node and the two closest neighbor nodes, then we make the summation of each individual triangle in each contact zone to obtain the total area of each surface.

Finally, with each total area for each zone S , the Young's modulus E calculated for the corresponding zone, and assuming the unit value for the thickness of the bone e , the equivalent stiffness k_{eq} of each contact zone is obtained.

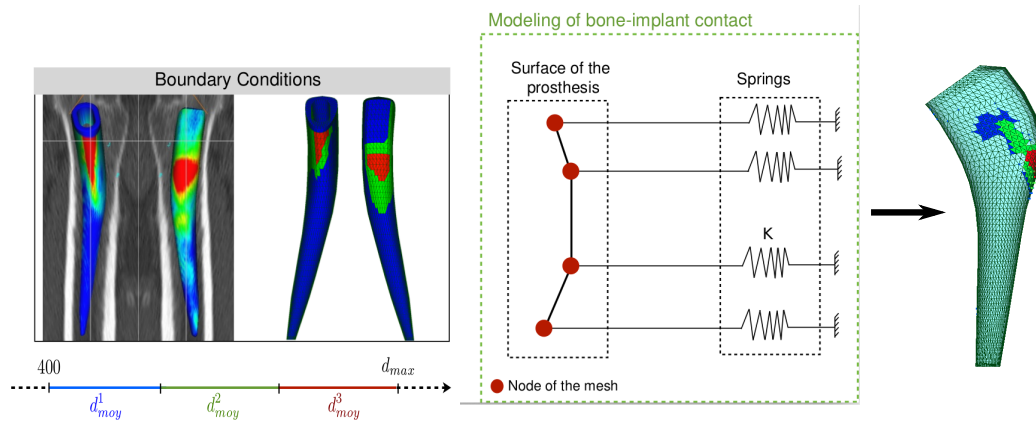


Figure 3.2: Left: Contact zones defined of the prosthesis with a 3D planning. Middle and Right: Bone-implant contact modeling principle.

3.3 Results

In table 3.2 we present the modal shapes and modal frequencies for the first five eigen-modes for one stable patient and one unstable patient, both with implant size C, in a frequency range $[0 : 20]$ kHz. Two of the stable patients (A and B) presented a total of 5 and 7 modes respectively, and the unstable patients (E and F) a total of 7 modes and 9 modes, respectively. The frequencies for the stable patients go from around 2-18 kHz, while for the unstable patient the frequencies range from around 2-16 kHz. The range of frequencies and the number of modes seem to present very variable patterns for stable and unstable cases. This is observed for all the 6 patients that we studied.

The information contained in the modal shapes is richer (see images in Table 3.2). For the unstable patient the modal shapes show a proximal bending, particularly in modes three and four, indicated by the variation of color on the top of the implant (not blue). For the stable patient the obtained modal shapes do not display this proximal bending. Similar patterns were observed in the other studied cases, with some exceptions in some of the patients where the modal shapes did not follow that pattern (see appendix A).

3.4 Discussion

The appearance of a stem bending mode concentrated on the proximal part seems to be the signature of an undesired fit, and as a result of bad primary stem stability. These results are coherent with the clinical experience, that indicates that excessive proximal motion of the stem is associated with a bad fit of the implant. Based on this preliminary results, and having found certain patterns of stability discrimination (presence of proximal bending) we have considered of importance to measure and

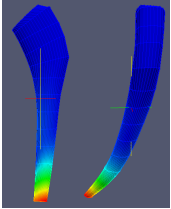
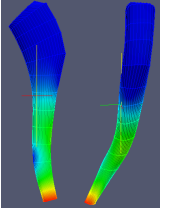
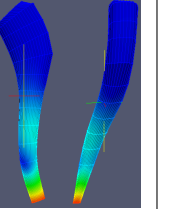
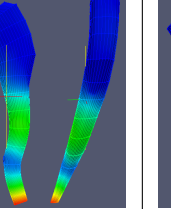
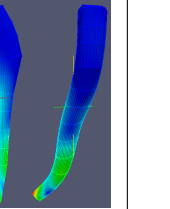
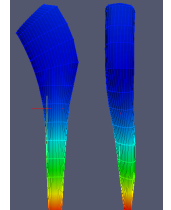
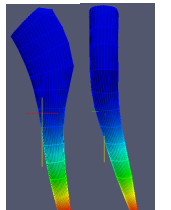
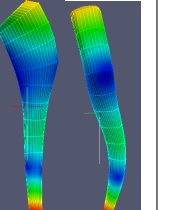
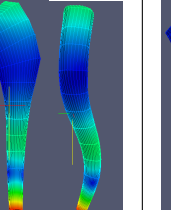
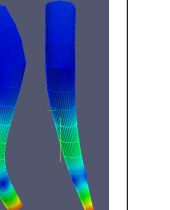
	Number of Modes	Eigen modes					
		1	2	3	4	5	
A	5	8110	10525	11189	16213	17918	Hz
							
F	9	2357	2940	7418	9271	16137	Hz
							

Table 3.2: Modal shapes of the first five modes of two patients of the study, as well as the number of modes and modal frequencies in the frequency range $[0 : 20]$ kHz. Proximal bending modes indicated by variation of color at the top of the implant (not blue).

characterize the effect of the magnitude of the contact stiffness and the size of the area on which it is distributed, to establish stability thresholds that can be used as a reference in preoperative planning. Furthermore, we consider crucial to be able to measure this proximal motion in the modal shapes with a numeric value, for this we have proposed to calculate the elastic potential energy ratio of the proximal part of the stem. These ideas are explored and presented in Chapter 4.

Our method applying local stiffness values through the use of springs to emulate the effect of the contact between bone and implant is a simple technique for running numerical simulations. However, one limitation is that in our analysis we consider a thickness e equal to the unit for obtaining the equivalent stiffness k_{eq} of each contact zone. The effect of the actual thickness is unknown, in fact even the physical definition of this thickness represents a challenge. With the goal of finding possible answers to these questions, in Chapter 6 we investigate a little further and discuss different considerations related to this thickness and its complexity.

Another limitation of this first exploratory study is that only six patients were analyzed. The method needs to be implemented on a larger group of patients to assess consistency of the observation.

CHAPTER 4

Modal analysis of controlled cases

The material presented in this chapter was submitted for publication in the journal "Medical Engineering Physics". Title of the article: "Modal analysis for the assessment of cementless hip stem primary stability in preoperative THA planning".

Ideally, a THR 3D planning software should provide a clear indication of the expected primary stability for a given stem in a given femur. In order to achieve this, a patient-specific mechanical analysis of stem stability must be done. Several factors play an important role in the press-fit condition of a cementless implant in THR, which ultimately define the primary stability. Among these factors, the contact zone size (CZS) and the apparent stiffness of the bone-implant interface are critical. This stiffness is found to be highly variable in patients, which must be taken into account in the planning. This can be achieved by using the densitometric information in the CT-scan which provides an indirect measure of stiffness (Helgason et al., 2008).

This chapter elucidates the relationships between the modal response of a hip stem (modal frequencies and modal shapes) and the boundary conditions on the stem in terms of area of contact zone (CZS) and the apparent stiffness at the bone-implant interface. This work is based on the hypothesis that variations in CZS and apparent stiffness are reflected in the modal behavior of the stem and that the latter converges to specific patterns characteristic of a stable stem as CZS and interface stiffness increase. If this hypothesis is true, a patient-specific modal analysis in the framework of the 3D planning could potentially discriminate between stable and unstable stem positions.

4.1 Materials and Methods

This chapter is dedicated to describe a study based on a finite element (FE) modal analysis of a cementless stem (SPS® size C, length 120 mm, Symbios, Yverdons-les-bains, Switzerland) and its implementation to assess the effect of CZS and contact stiffness. Implementing the FE modeling methods using the software *Code Aster*, as described in chapter 2.

In order to evaluate the effect of the size of the contact area between bone and the stem, four different CZS of surface elements were defined on the surface of the stem mesh (Figure 4.1, Left): Small (400 elements $\approx 5cm^2$), Medium (800 elements

$\approx 10,5\text{cm}^2$), and Large (1200 elements $\approx 15,6\text{cm}^2$), a fourth intermediate CZS was included later for verification (SM, 600 element $\approx 7,5\text{cm}^2$). The CZS's positions and shapes were defined by an experienced orthopaedic surgeon, by taking into account the typical contact patterns that are observed in common clinical cases when a 3D preoperative planning is performed (Sariali et al., 2012b).

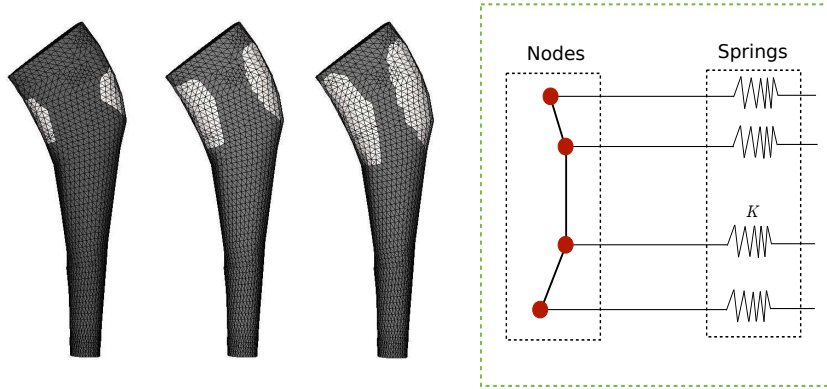


Figure 4.1: Left: Large, Medium, and Small contact zones represented on the stem. Right: springs stiffness effect attached to the nodes of the stem.

The stiffness of the bone in contact with the stem is simulated by springs attached to each node of the contact zone surface (Figure 4.1, Right), as described in chapter 2, equation 2.1. The apparent stiffness K of each contact zone was chosen to range between $10^1 - 10^{10}$ N/m which accounts for the whole spectrum of reasonable stiffness values. The apparent stiffness K is distributed evenly on the contact surface by adjusting k . Free conditions (no contact, i.e. $k = 0$) vibration modes were also computed for reference.

The FE modal analysis was conducted with Code Aster (Code_Aster, EDF R&D, license GNU GPL, <http://www.code-aster.org>) implementing the Sorensen method for modal computation. The outputs of the computation are the modal frequencies and shapes calculated in the frequency range [0 – 21 kHz].

4.2 Data Analysis

The number of modes in the range [0 – 21 kHz] and the frequencies and shapes of the first five modes were investigated with respect to contact apparent stiffness and contact area.

Similarities between modal shapes were quantified with the modal assurance criterion (MAC), a quantity which is used extensively in structural vibration analysis. The MAC is a scalar constant between 0 and 1 that relates the degree of similarity (collinearity) between two modal vectors (shapes) (Allemang, 2003). For each mode of number n (n varies typically between 1 and 5 in the present study), the MAC was

calculated to compare the modal shapes for the different cases of CZS and contact stiffness. The purpose was to follow the modal shape changes associated to a given mode number as CZS and contact stiffness vary. The extreme values of MAC may be interpreted as follows, $MAC = 0$ corresponds to non-collinearity, and $MAC = 1$ corresponds to perfect collinearity (identical modal shapes).

Clinical experience suggests that the presence of excessive proximal motion of the stem in the bone may be an indicator of instability for the metaphyseally fixed stems such as the SPS® (Sariali et al., 2012b). Within the framework of the modal analysis, the relative motion of the proximal part of the stem for the different modal shapes is investigated as a proxy for the stem proximal motion in a clinical setting. In other words, we hypothesize that the stem would likely be stable for a given CZS and contact stiffness, if the modal shapes display a relatively small motion in the proximal part.

This motion in the proximal part is quantified by the ratio rEPE of the elastic potential energy (EPE) in the proximal part of the stem (≈ 1400 elements in the utmost proximal part) to the EPE in the entire stem's volume. We investigate three thresholds values of rEPE as possible markers of a sufficiently good anchorage. We then analyze the relationships between CZS and contact stiffness for these thresholds.

4.3 Results

The number of modes in the frequency range [0-21 kHz] is reported in Figure 4.2 for all the different CZS and contact stiffness. For all the CZS cases 11 modes were obtained for low stiffness values, ranging from $10^1 - 10^6$ N/m. After this point, the number of modes decreases to reach a minimum of 5 modes for the highest stiffness values for all CZS, This minimum however is reached at different values of stiffness with each CZS, with 10^7 , 10^8 , and 10^9 N/m for CZS of decreasing size. This evolution of the number of modes with increasing stiffness shows two plateau values, corresponding to the high and low stiffness values, and a sharp transition for stiffness around $10^7 - 10^8$ N/m, suggesting a transition between two essential behaviors. Similar transitions are reported below for other modal quantities. In the latter, we refer to *State A* (limiting behavior for low stiffness) and *State B* (limiting behavior for high stiffness). We will later discuss the possible relationships between States A vs. B and unstable vs. stable stem anchorage.

Modal frequencies increased consistently with stiffness values and CZS (Figure 4.3). Similar to the evolution of the number of modes (Figure 4.2), there is a zone of low frequencies (*State A*) for low stiffness and a zone of high frequencies (*State B*) for the high stiffness and a transition zone with a sharp increase in the frequency values occurring in a relatively narrow stiffness range around $1^4 - 10^6$

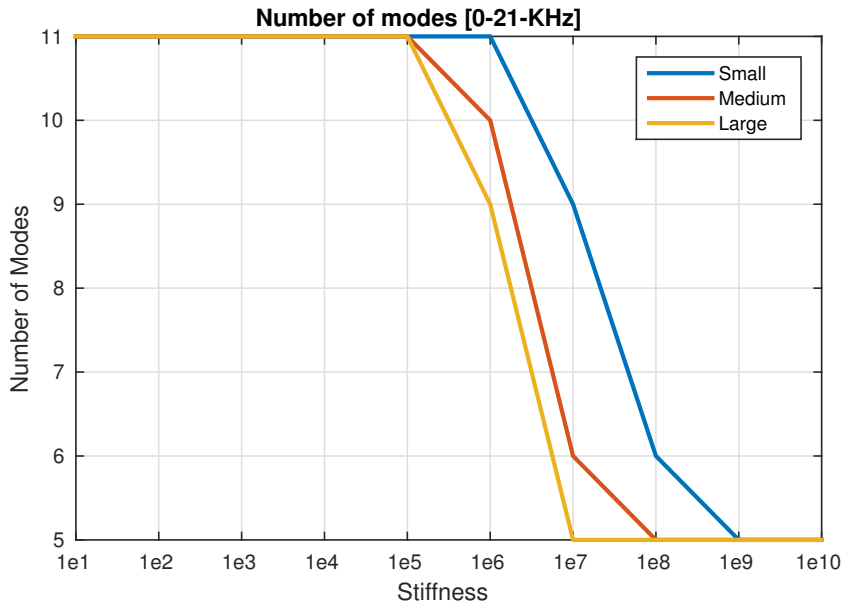


Figure 4.2: Evolution of the number of vibration modes in the frequency range 0-21 kHz vs. contact stiffness for each of the contact zone sizes (CZS).

for all the modes and CZS. Between stiffness $10^4 - 10^8$ N/m the relative frequency of mode 5 varies in a larger interval ($60.81 - 20.33 \cdot 10^3$ Hz), compared to other modes ($11.90 - 3.25 \cdot 10^3$ Hz for mode 1 for instance), hence the frequency of mode 5 appears to be much more sensitive to variations in contact conditions.

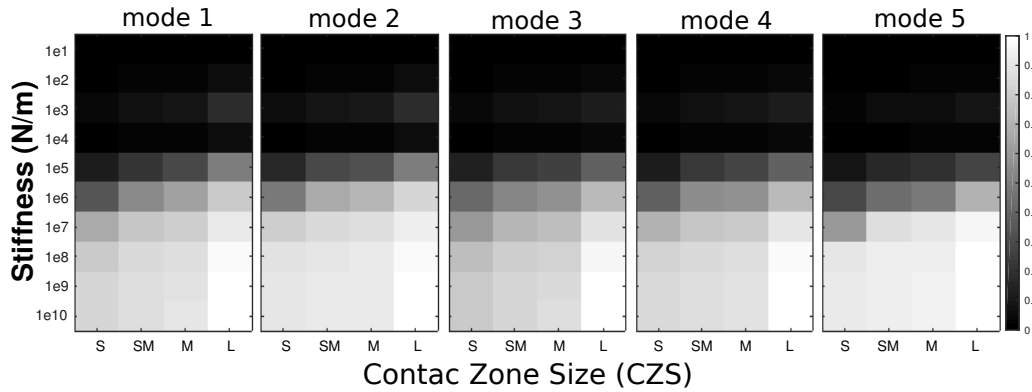


Figure 4.3: Modal frequencies of the first five modes (frequency range 0-21 kHz) of the stem plotted against stiffness (N/m) and contact zone size (S, SM, M, L). Values are normalized with respect to the highest frequency for each mode. The maximum frequencies obtained for each mode are, mode 1: 3.25 kHz, mode 2: 3.91 kHz, mode 3: 12.36 kHz, mode 4: 14.21 kHz, mode 5: 20.33 kHz.

Figure 4.4 gives for each of the CZS the result of the MAC analysis comparing the modal shapes of contact stiffness value 10^i versus 10^{i+1} ($i = 4 - 9$); results for contact sizes S, M, and L are shown, SM presented the same result as the M contact

size. Similarity of the modal shapes is quantified with the MAC number. A white diagonal in a sub-figure signifies that the modal shapes of the first five modes do not change (i.e. high collinearity) for a multiplication of the stiffness by a factor 10. For low values of stiffness, the modal shapes are close to rigid body modes. For all modes these shapes are very similar for stiffness smaller than 10^5 . It must be noticed that the shapes of modes 1 and 2 remain grossly invariant across all the range of stiffness, as evidenced by the first two diagonal terms of each sub-figure which remain close to one (white squares). For modes 3 to 5, the figure reveals a transition zone between $10^5 - 10^7$ N/m, indicating an important change in the modal behavior. Overall, the MAC analysis indicates that, for a given CZS, before (State A), and more interestingly, after the transition zone (State B) $10^5 - 10^7$, each mode has a unique shape whatever the contact stiffness. Hence, even though after the transition zone the frequency continues to increase (Figure 4.3), the modal shapes remain invariable. It can be noticed on the MAC figure that the behavior of State B is reached for higher values of stiffness for the Small CZS compared to larger CZS. See Appendix B for a summary of the modal shapes of the implant.

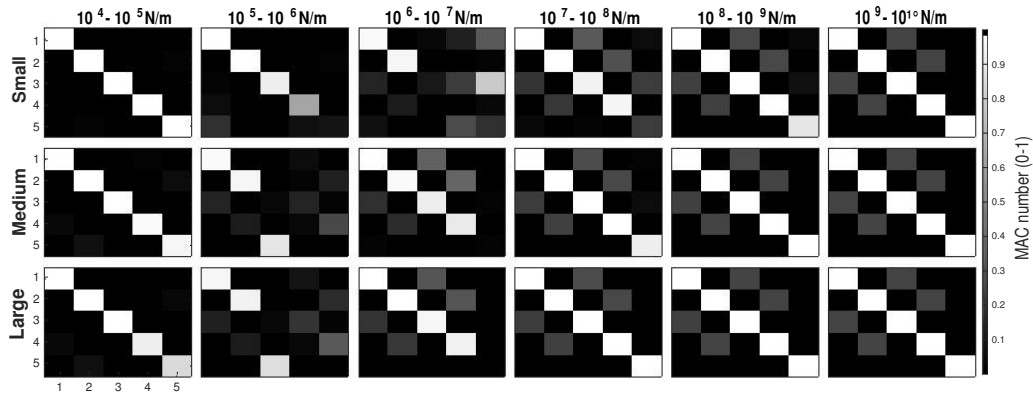


Figure 4.4: Each box contains the MAC correlation of modes 1-5 for for different cases of CZS (row 1: Small, row 2: Medium, row 3: Large) and stiffness in ascending order pairs between 10^4 and 10^{10} N/m.

For all the modes and all CZS, rEPE values are close to zero (State A) below a threshold stiffness value around 10^4 N/m, grow more or less rapidly to a peak value for stiffness ranging between $10^6 - 10^8$ N/m and rapidly decrease (Figure 4.5, top row) to reach plateau values characteristic of State B. For all modes, the smaller the CZS, the larger the stiffness for the peak rEPE value, which is consistent with the idea that, for a smaller contact zone, a stiffer contact is necessary to prevent proximal motion. Frequency values (same data as in Figure 4.3) as a function of stiffness are also shown for comparison (Figure 4.5, bottom row). The peak rEPE value is consistently found to correspond to the transition zone in the frequency behavior, also corresponding to the transition zone for the number of modes (Figure

4.2). Towards the largest contact stiffness, the frequency values reach a plateau and rEPE values become small (State B). The physical explanation for small rEPE values at low stiffness on the one hand and high stiffness on the other hand are different. At low stiffness, the observation of modal shapes reveals that the motion of the implant resembles rigid body motion, with small deformations overall for all the modes, this leads to low rEPE values as rEPE is a marker of the deformation of the proximal part of the stem relative to the entire deformation of the stem. At high stiffness, the modal shapes resemble partially constrained body motion showing a relatively large deformation in the distal part, while the proximal part, being just above the contact zone, is blocked, resulting in low rEPE.

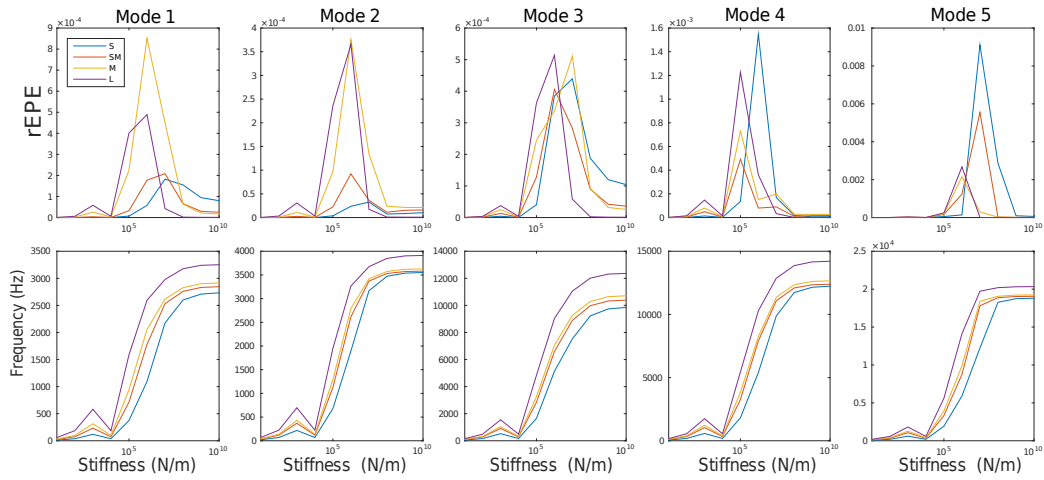


Figure 4.5: rEPE (top) and natural frequencies (bottom) vs. stiffness, of the first five modes (sub-figures left to right) for all CZS (S, SM, M, L).

Mode 5 shows the largest range of variation of rEPE. Also, for this mode, the evolution of rEPE (and particularly the stiffness value corresponding to peak rEPE) for CZS L and M on the one hand, and of SM and S on the other hand are clearly different. This suggests that mode 5 is a good candidate marker of the transition in vibrational behavior from State A to State B with increased contact stiffness and CZS.

In the transition zone $10^5 - 10^7$ N/m (Figure 4.5, top row), it can be observed that between 10^5 and 10^6 N/m the rEPE increases with stiffness and CZS. Subsequently, at 10^7 N/m and after, rEPE decreases as the CZS and stiffness increases, revealing the thresholds where the contact stiffness starts reducing the proximal motions.

The sensitivity of mode 5 to contact stiffness variations can be verified by comparing Figures 4.5 and 4.6. The patterns of the total sum of the modes happen to match that of mode 5, suggesting that mode 5 is the most representative of the stem's model.

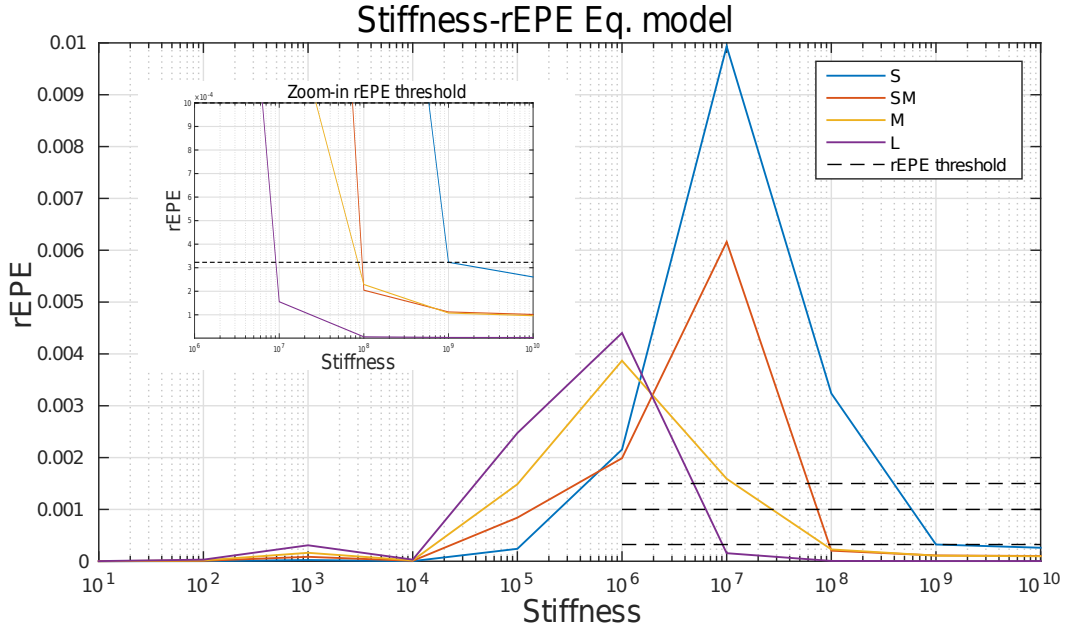


Figure 4.6: rEPE Vs. Stiffness for each CZS (S, SM, M, L) with reference values of rEPE thresholds (dashed lines) in decreasing tendency ($1.5 \cdot 10^{-3}$, $1 \cdot 10^{-3}$) and rEPE convergence value ($3.2 \cdot 10^{-4}$).

Three candidate stability thresholds were defined for the summed rEPE (sum of rEPE for all modes): $1.5 \cdot 10^{-3}$, $1 \cdot 10^{-3}$, and $3.2 \cdot 10^{-4}$ (Figure 4.6). The first two thresholds ($1.5 \cdot 10^{-3}$, $1 \cdot 10^{-3}$) correspond to the zone where the rEPE has a decreasing behavior, that is, the rEPE transition zone. And the third threshold ($3.2 \cdot 10^{-4}$) has been identified as a common rEPE convergence value for minimal proximal motion considering all the CZS and stiffness values. For each of these thresholds, corresponding stiffness values were obtained by linear interpolation based on the data presented in Figure 4.6 and are reported in Figure 4.7 as a function of the number of elements of the CZS. A linear equation model that fits the CZS-stiffness relations obtained is represented in Figure 4.7.

Figure 4.7 illustrates the CZS-Stiffness trade-off associated to a given rEPE value for the different choices of the rEPE threshold value. Under the assumption that a given threshold is associated to a stable stem, the data in Figure 4.7 gives the couple of minimum values (CZS, contact stiffness) for which the stem would be stable. Alternatively, the data serves to predict the range of apparent stiffness necessary to achieve stability for each contact zone size. As expected, the larger the CZS, the smaller the required contact stiffness. For CZS equal or larger than SM, the stiffness required for stability grossly lays within a decade between 10^7 and 10^8 . Considering that the stiffness rapidly increases with decreasing CZS, for a smaller CZS the stiffness may be 10 to a 100 times more depending on the threshold chosen.

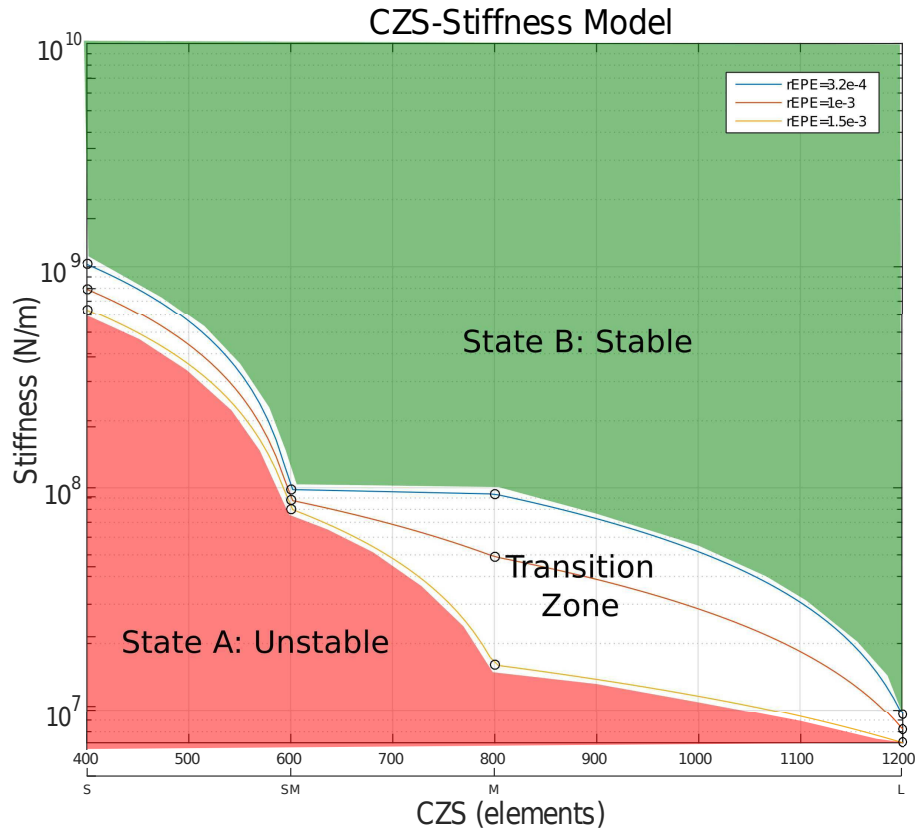


Figure 4.7: Stiffness Vs. CZS relation models for three different thresholds of rEPE ($1.5 \cdot 10^{-3}$, $1 \cdot 10^{-3}$, $3.2 \cdot 10^{-4}$).

4.4 Discussion

The objective of this work was to assess the sensitivity of RP3D to modifications of boundary conditions corresponding to various qualities of bonding of the stem to the bone. The resistance of the bone to the motion of the stem surface was modeled by a reaction force created by springs. The latter act on defined contact zones whose location and dimension were decided according to the surgeon's experience (Figure 4.1, Left). The modal response of the stem was analyzed for a range of spring stiffness and four sizes of contact zones (CZS). The chosen range of stiffness and CZS is supposed to include clinically relevant situations of a loose fit of the stem (relatively small CZS and/or small stiffness) and strong fit (relatively large CZS and/or large stiffness).

The modal response was investigated in terms of the number of modes in the range $[0 - 21 \text{ kHz}]$ (Figure 4.2), the modal frequencies, and the modal shapes (Figure 4.5). Changes of modal shapes were quantified with a MAC analysis (Figure 4.4) and the proportion of the proximal motion was quantified with the rEPE, the

relative elastic potential energy in a proximal region of interest. All these characteristics of the modal response had a consistent behavior when stiffness and CZS were changed, clearly exhibiting two limiting behaviors, respectively for small and high stiffness values, irrespective of CZS. We referred to these limiting behaviors as State A, representative of an unstable stem, and state B, representative of a stable stem. Between states A and B there is a transition zone (stiffness range $10^4 - 10^7$) where the number of modes below 21 kHz drops from 11 to 5, frequencies of all modes increase sharply before reaching a plateau value towards State B, the modal shapes change, and the rEPE goes through a maximum. The modal responses for the different CZS cases follow the same trend but have slightly different behaviors as stiffness increases: as expected, the convergence towards the plateau state B (number of modes, frequency values, modal shape) occurs for respectively higher values of stiffness as CZS decreases.

It appears important to summarize all the modal information to give the clinician an indication of the stability that could be achieved for a certain combination of contact stiffness and CZS. First, we note that modes 1 and 2 are less sensitive to changes of boundary conditions than other modes, and that mode 5 is the most sensitive (Figure 4.4). Furthermore, given the absolute values of rEPE for the different modes, the sum of rEPE for all modes is dominated by the contribution of mode 5. Hence, we proposed the summed rEPE as a privileged marker of stability because of its relatively high sensitivity to changes of boundary conditions and because it is related to the proximal motion of the stem, which is of clinical relevance. The summed rEPE was used to define areas in the plane CZS-stiffness that correspond to a more or less stable stem (Figure 4.7). The plane CZS-stiffness can serve to identify the regions in which proximal motion of the implant is avoided, or in other words, to predict the range of apparent stiffness necessary to achieve stability for a given contact zone size.

We investigated rEPE thresholds that correspond to rEPE convergence approximations for all the CZS, and for which stem anchorage is likely to be acceptable. We used three threshold values to exhibit the sensitivity of the chosen threshold on rEPE values. We found that for CZS between $7.5 - 15.6 \text{ cm}^2$, and stiffness between $10^7 - 10^8$ ensures convergence to State B. For CZS smaller than 7.5 cm^2 , a higher stiffness would be required.

In the past decade, a few authors have documented the vibrational behavior of hip stems anchored to bone for various contact situations between the stem surface and the bone. (Qi et al., 2003; Pastrav et al., 2009a; Perez and Seral-Garcia, 2013) conducted finite element modal analysis to compute modal frequencies of the stem and femur bone assembly. They all found that increasing the area of the contact is associated with an increase of modal frequencies. This is expected and is also

what we have observed in this work which considers the modal response of the stem isolated from the femur.

Our findings that mode 5 is more sensitive to changes of contact conditions is in line with the results of previous works suggesting that higher order modes are more sensitive because they are associated to more complex motions (Pastrav et al., 2009a; Perez and Seral-Garcia, 2013). Also, (Pastrav et al., 2009a) already pointed that the vibrational behavior is most influenced by contact changes in the proximal zone, which is the part of the stem on which we consider a contact with bone in the present work, consistent with clinical observation.

The aforementioned studies have investigated the influence of different contact interface conditions in the vibrational response of the bone-implant system, finding significant effects on the stability of the system. These studies attempt to simulate the vibrational behavior that can be measured perioperatively (Pastrav et al., 2009b). The present study, to our knowledge, is the first attempt to explain the modal behavior of the stem alone (the bone is not considered in the vibrating system) subjected to typical contact boundary conditions. The results of our simulations can not be compared to an experimental quantity because in reality, the bone attached to the stem vibrates together with the stem, hence producing a very different vibrational response. The present study uses the vibration of the stem alone as a potential marker of stability in the framework of 3D preoperative planning. The implementation of our model is significantly less complicated than models cited above in which the bone is considered. In the latter, the geometry and mechanical properties of the bone must be carefully modeled. In previous studies aimed at modeling an experimental quantity, namely a set of resonance frequencies, only the effect of contact conditions on frequencies has been formerly investigated (Qi et al., 2003; Pastrav et al., 2009a; Perez and Seral-Garcia, 2013). In the present work we have also investigated the number of modes and the modal shapes in detail, exhibiting rEPE as an promising quantity to reflect various levels of stability.

This study has a number of limitations. The study provides a thorough analysis of the modal behavior of a particular type of cementless stem with a metaphyseal proximal fixation (SPS®). The specific values of frequencies, and modal shapes may to a certain extent be different for another stem geometry. The positions of the contact zones were defined by the surgeon according to his experience in the operating room and also as a user of 3D planning software. We have favored the definition of these idealized zones over more realistic zones (that could be obtained through e.g. the planning software) in order to facilitate the analysis of the results. The trends of the modal behavior for more realistic contact zones is expected to be similar to the trends described in this study. The distribution of stiffness on the contact zones was assumed uniform. An inhomogeneous, possibly more realistic distribution, is not expected to modify the results to a large extent because the

modal behavior is an overall mechanical response weakly sensitive to the details of the spatial patterns of boundary conditions. The criterion for assessing stability from the numerical modal response uses rEPE (Figure 4.7), whose value is set to be sensitive to proximal motion. This follows our hypothesis, derived from clinical experience, that implant primary stability is obtained for a small proximal mobility of the stem. Other quantities in the modal response (such as specific modes, frequencies, or modal shapes) may also be strongly related to stability. However, it was not the purpose of the study to perform an extensive analysis of these relationships.

The conclusion of the present technical study, is that RP3D is very sensitive to changes of boundary conditions and could help discriminate stable versus unstable stem-bone assembly prior to surgery. This, however, remains to be proven in a clinical context. This could be performed as follows. Experienced surgeons can realize a series of both 'good' and 'bad' simulated trials of P3D using existing databases of patients CT-scans. The results of RP3D should be consistent with the classification of the surgeon as good or bad planning. Experienced surgeons can also perform several P3D for one patient corresponding to different sizes of stem, when only one would give a good primary stability. Again the results of RP3D should be consistent with the actual stem size chosen by the experienced surgeon. Finally, plannings of patients who have had THR can be processed with RP3D, the outcome of surgery for these patients is known and could be confronted to RP3D results.

In order to perform RP3D based on a patient's CT scan, the contact zones and stiffness values must be defined. Contact zones can be delimited using a threshold on HU values; these HU values should be converted to stiffness as bone is expected to offer a resistance to the motion of the stem according to its density. In the numerical model, the physical significance of the specific values of stiffness of the contact zones is not straightforward. Although relationships exist between Hounsfield units (or apparent density) and bone elasticity (Helgason et al., 2008), these cannot be used as such for our purposes. Indeed, as the model uses a spring stiffness (force per unit distance), we need to introduce a reference dimension (to be multiplied by the elastic modulus) which does not have a straightforward physical meaning. We propose that the stiffness values prescribed in the numerical model be proportional to HU values in the CT scan and that the conversion law between HU and stiffness be calibrated based on clinical cases.

We anticipate that RP3D could contribute to improve the reliability of THR procedures by providing a mechanical criterion to assess stability preoperatively. Typically, the surgeon will have an indication on the possibility to obtain sufficient primary stability for a patient considering the different possible stem sizes (allocating more or less large contact zones) and the density of the bone. RP3D would be particularly helpful in cases for which a choice must be made between a standard or custom cementless stem, or a cemented stem. RP3D could foster the use of 3D

planning in THR by providing a simple indicator of stability and by reducing the time necessary to complete the planning. Note that the computation time required to do a modal simulation could be of the order of a few seconds and is not expected to be a limitation. RP3D, in line with its use as a preoperative planning tool in general, could also be useful for training of surgeons.

Characterization of broaching effect on bone-implant interface from μ CT-Scan images

5.1 Introduction and Context

As previously described in Chapter 1, when cementless implants are used, primary stability is an essential requirement for achieving a proper osseointegration and a long-standing fixation (Albrektsson and Albrektsson, 1987; Viceconti et al., 2006). This primary stability will depend on the press-fit of the bone-implant pair which is influenced by the properties of the bone at the interface (Karachalios, 2014; Ramamurti et al., 1997). THR involves a broaching procedure in which the orthopedic surgeon utilizes a set of broaching tools (Figure 1.5) to open the femoral canal by removing and compacting the trabecular bone. Different sizes of broaches are used, the surgeon gradually increases the size of the broach inserted until obtaining the desired cavity size for the selected implant. To the best of our knowledge, variations of the bone properties in the bone-implant interface region due to this broaching procedure have not been studied and defined to this date. The compression and subsequent reorganization of the trabecular bone in the interface caused by the broaching could have a decisive effect on the press-fit of the bone-implant pair, and, as a result, on the primary stability and inherent long-term integration of the system.

In Chapter 1 it was discussed how 3D preoperative planning software can help the orthopedic surgeons to make the selection of size and location of the implant prior to the surgery and reduce the risk of errors (Sariali et al., 2009b); the surgeon navigates with the implant in the cavity of the femur until finding satisfactory conditions indicated by a cartography given by the Hounsfield density of the bone in contact with the implant. As these software are used for planning the surgery, evidently the CT-Scans it utilizes are obtained prior to the operation, and do not take into account the effect of the broaching.

In this chapter we measure variations of the bone structure in the bone-implant interface due to the effect of the broaching in micro-Computed-Tomography Scan (μ CT-Scan) images of cadaveric samples. Regions of interest (ROI) are defined by an orthopedic surgeon based on clinical observations that indicate what areas are more important for the anchorage of the implant. These ROIs are used to measure and characterize changes inside the cavity of the bone left by the passing of the broach, with variations of bone mineral density (BMD) as the parameter

of reference. Different image processing techniques are implemented on μ CT-Scan images before and after broaching to obtain those variations.

The consideration of structural variations of the bone in the bone-implant interface due to the broaching procedure may have an important influence in implant selection in 3D preoperative planning. Moreover, the characterization and understanding of BMD variations with broaching can help to predict the outcome of a procedure if we take into account that certain minimal BMD conditions need to be met to obtain a satisfactory implant anchorage. These predictions can help the surgeon in the decision of the type of implant to be used and the implantation method (cemented or cementless implant) based on the initial BMD of the patient (before broaching).

5.2 Materials and Methods

5.2.1 Overview of the protocol

Figure 5.1 displays an overview of the protocol followed for this part of our study, which are explained in details in the different sections of this chapter. In a nutshell, this protocol goes like this: first, the samples for the study were selected (27 samples) using a 3D preoperative planning tool. Then, the selected samples (4 samples) are prepared to be scanned. μ CT-Scan images are acquired with a calibrated scanner. The broaching procedure is performed by the surgeon on the selected cadaveric samples. μ CT-Scan images are acquired after the broaching procedure is performed, this are used to observe variations by comparing with the scans before broaching. The images area treated using image processing techniques of registration and segmentation. Finally, the variations of BMD observed between both sets of scans (before and after broaching) are analyzed to characterize and describe the broaching effect on the bone cavity.

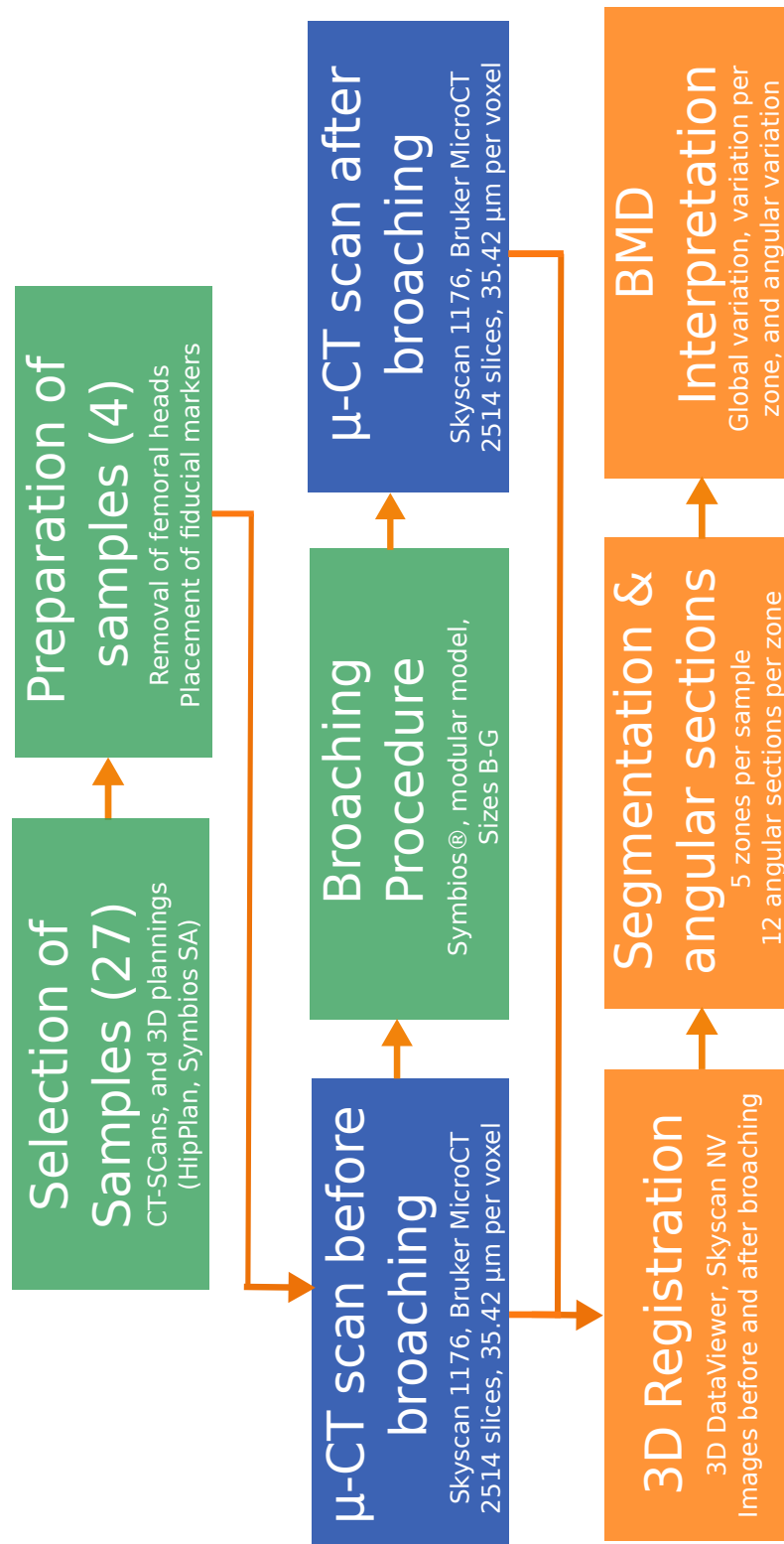


Figure 5.1: Scheme of the protocol followed for the image analysis study of μ CT-Scan images of the bone after the broaching procedure.

5.2.2 Samples handling and preparation

- **Obtainment of the adult bone samples.** For this study 27 human femur bones were collected, 15 female and 12 male adults aged between 71 and 99 years-old, obtained from : the UFR of Medicine of the Université Paris Diderot (Site B2OA UMR CNRS 7052). Before collecting them, the bones were stored frozen at -21°C in vacuumed plastic bags. The collected bones were previously cut and only the proximal part of the femur was available.
- **Bone Preservation** There are two main methods for preserving bone, freezing and chemical fixation. Multiple studies in human cortical bone have shown that a freezing temperature of -20°C allows to maintain most of the mechanical properties of the bone (including ultimate stress, modulus of elasticity, energy absorbed to failure, and hardness) (Martin and Sharkey, 2001).
- **Thawing and handling temperature** The samples must be thawed before the broaching procedure. The samples were thawed at 37°C and broached at room temperature (23°C) (Turner and Burr, 2001).
- **Manipulation during scan acquisition** The samples must be well wrapped and vacuumed to avoid leaking of fluids inside the chamber of the scanner, and as tight as possible to make the sample compact, this is of great importance considering the space limitations of the chamber. After the scan is done each sample is re-wrapped in a plastic bag, vacuumed and frozen.

5.2.3 3D Planning and selection of samples.

As the geometrical characteristics of the bone samples are highly variable, it was necessary to make a selection of samples that allowed to make comparisons between results and simplify the analysis of our observations. For this, the surgeon performed 3D plannings of all the 27 bone samples using the 3D planning computational tool *HipPlan* (Symbios SA, Yverdon Les Bains, Suisse). For this, Ct-Scans of the samples were obtained, using a CT-Scanner (Optima CT660, GE Healthcare, Buckinghamshire, United Kingdom). Eight (8) samples (Table 5.3) that presented similar characteristics and similarities with typical clinical cases (size and geometry of the femoral cavity) were selected from the initial group, based on observations of the surgeon during the planning.

The selection took into account the implantation of a stem (SPS®, Symbios). The stems sizes varied from size B to G, from smaller to larger, respectively. According to the surgeon in charge of doing the selection, in common practice the *E* stem size is the most frequently implanted, this and the correspondence with femurs that are closer to those of patients with normal conditions are the preferred criteria

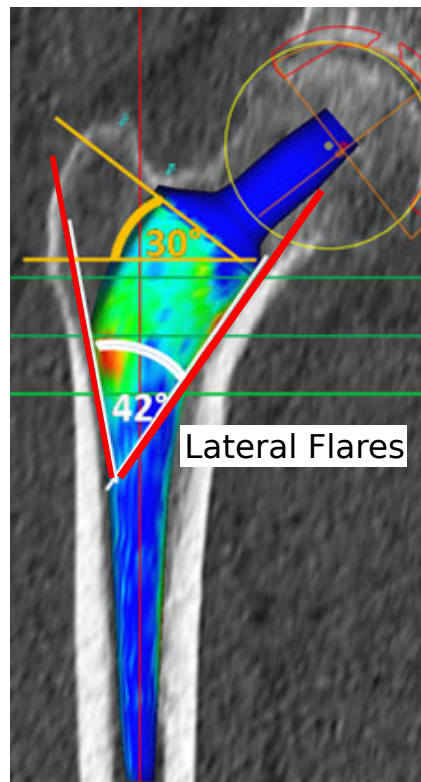


Figure 5.2: The red lines indicate the lateral flares (angle $\approx 42^\circ$) that were taken into account for sample selection. Reproduced from (Sariali et al., 2012b)

of selection, with bone that presents a higher density and morphotypes with more standard lateral flares (Figure 5.2).

At least four different stem sizes (D, E, F, G) with two samples each were obtained, seven corresponded to left side (L) and 1 to right side (R). One extra bone (size D) was incorporated as a test sample for testing each step of the protocol before using the study samples.

5.2.4 Preparation of samples.

Removal of femoral heads

Having certain dimension constrains, since the maximum diameter of the μ CT-Scan machine available was 72.5 mm, the femoral heads had to be removed before the procedure to adapt the size of the sample to the scanning chamber of the available machine. For this an electric oscillatory surgical saw was used.

The samples were fixed still frozen in a circular three-jaw self-centering chuck (Figure 5.4), the chuck is well fasten carefully to not damage the bone.

	Sample Id	Stem Size	Side
1	362	D	L
2	376	D	R
3	261	G	L
4	269	E	L
5	283	F	L
6	331	E	L
7	282	G	L
8	268	F	L
TEST	229	D	L

Figure 5.3: Bone samples selected by the orthopedic surgeon.



Figure 5.4: Circular three-jaw self-centering chuck mounted on a wood plank, used for holding the bone stable.



Figure 5.5: Cut of the femoral head

The cut line is drawn on the femoral neck by the surgeon with a marker (Figure 5.5 a), this line is obtained from linking anatomical reference points already established and known in THR practice. With the use of a goniometer it is verified that the angle described by the reference points measures $\approx 30 - 35$ degrees as shown in (Figure 5.5 b). The femoral head is then removed with the use of the surgical oscillatory saw, following carefully the reference line (Figure 5.5 c). After the femoral head is removed, the reference angle is verified again with the goniometer (Figure 5.5 d). A custom-made measuring device with the maximum size allowed by the micro-CT-Scan machine is used to measure the bone and to guarantee that it will fit in the scanning chamber (Figure 5.5 e).

Fiducial Markers

As μ CT-Scans are done before and after the broaching of the femur to compare both states, it is necessary to achieve a good correspondence of the scan slices, meaning that an appropriate image registration technique needs to be implemented. Fiducial markers were defined on the external surface of the bone in order to improve the coplanarity of the scan slices before and after broaching, and to facilitate the image registration. Two linear marks were made on the surface of the bone, for this a rotary tool was used (DREMEL® 4000, Dremel Europe, Breda, Netherlands) trying to place the marks outside the region of interest of 6 cm indicated by the surgeon (Figure 5.7), and making sure of keeping the mark as superficial as possible to avoid excessive damaging of the bone. At the moment of making the μ CT-Scans, two linear marks were also defined on the bed of the scanner following the same inter-mark distance defined for each bone sample, these marks were used to position the bone on the bed of the scanner and use the same reference for the scans before and after the broaching (Figure 5.6).

5.2.5 μ -CT Scan image acquisition.

The images for each sample were acquired before and after the broaching procedure with a μ CT-Scanner (Skyscan 1176, Bruker MicroCT, Kontich, Belgium). This scanner with a view field of 68 mm of diameter and a 200 mm length, allows the possibility to be used for scanning small animals used for experiments such as mice and rats, by setting the option of scanning in multiple parts with a length of 20 mm each. According to the experience and suggestions of the surgeon, the region of interest to observe the broaching effect is located in a zone of approximately 5 cm in length, with the lesser trochanter as the center reference (M), and $M+3cm$ and $M-2cm$ measured longitudinally from that reference (Figure 5.7). Hence, it took five consecutive scans, for a total length of 9.5 cm of the femur. For each femur a sequence of 2514 slices was obtained.

The total acquisition time for each sample was approximately 2 hours and 45 minutes. The parameters of acquisition are the following: Voxel resolution 35,425 μ m, isotropic, X-rays source 80 kV \hat{a} 291-300 μ A, exposition time 65 minutes, Rotation of 360° and a 0,500° step, filter of copper and aluminum. The same acquisition parameters were used before and after broaching, so the bone mineral densities can be compared. For the calibration of the attenuation coefficient of grey levels for the bone mineral density, two phantoms of concentration 0.25 and 0.75 g/cm^3 of CaHA (calcium hydroxyapatite) were scanned and analyzed using *CTAn* for obtaining a linear relation between the grey levels (HU) and the BMD, obtaining an HU calibration scale value of 65535.



Figure 5.6: Coincident reference lines, on bone (black lines), on scanner bed (red tape), for sample positioning in the scanner.

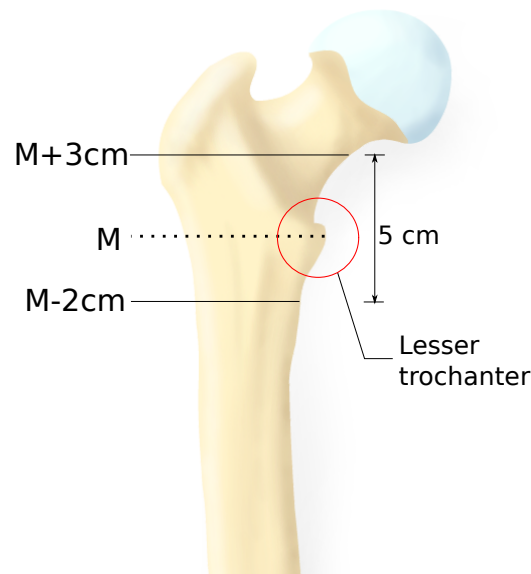


Figure 5.7: Illustration of the zone of interest of 5 cm for observing the bone-implant contact zones and the effect of the broaching, as indicated by the orthopaedic surgeon. Reproduced from: <https://images.radiopaedia.org/images>

The obtained images are a 360° sequence of radiographic images of the femur. These images were saved in format TIFF 16 bits (2^{16} grey levels). To be able to exploit these images, they had to be reconstructed first, for this we made use of the 3D reconstruction software *NRecon* (NRecon Software, V 1.6.10.4, Skyscan NV, Kontich, Belgium).

The parameters used for the 3D reconstruction are the following: view field 1968 x 1968 pixels, attenuation coefficient $0.000916 \hat{a} 0.025956$, correction of ring artifact 20%, correction of beam hardening artifact 45%. Each obtained slice is a 2D image saved in BMP - 8 bits - format (256 grey levels).

5.2.6 Broaching Procedure

For this part of the procedure the following materials were necessary: broaching set, fitting hammer, curettes, surgical oscillating saw, saw blades, circular chuck mounting system, water-bath machine, vacuum machine and bags, plastic foam, goniometer, markers, caliper, absorbent paper, scalpel, scissors. Before the operation the samples are thawed at a temperature of $37,5^\circ\text{C}$ in water-bath without removing from their plastic bag, with the purpose of bringing the samples to a temperature as close as possible to the natural body temperature at the moment



Figure 5.8: μ CT-Scan of the femur in progress.

of a THR surgery. For the mounting of the bone for the broaching operation, the self-centering three-jaw chuck is used to keep the bone in the desired position.

The bone needs to be well held with the chuck on the length of the region of 5 cm described in Figure 5.7. The surgeon broaches the bones using a THR broaching tools set (SPS® model, Symbios), with sizes from B to G Figure 1.5, only left side broaches were available for this operation. The broaching tools are introduced in the femoral cavity in a gradually size increasing fashion with the help of a hammer, to remove the trabecular bone, until obtaining the desired cavity size, which is defined on the 3D planning. Figure 5.9 illustrates the different main steps of the broaching procedure. The broaching of each bone took between 15 and 45 minutes, depending on the density of each bone.

5.2.7 Image Processing Procedure

Definition of measurement zones.

To evaluate BMD variations in the bone cavity due to the effect of the broaching, different measurement zones were established along the length of our region of interest (Figure 5.7) to be able to assess proximal and distal variations separately. Therefore, five different longitudinal zones of 1 cm each (L1, L2, L3, L4, L5) were defined as observed in Figure 5.10. This allowed us to evaluate BMD variations not only due to the effect of the broaching in different areas of the bone, but also to compare between different zones among different bone samples.



Figure 5.9: Main steps of the broaching procedure. From left to right: opening of the femoral cavity, introduction of the broaching tools with hammer blows, removal of trabecular bone with a curette.

The anatomic center of the lesser trochanter was taken as a reference point for the definition of longitudinal zones. Given the major relevance of the proximal part of the femur, three zones of 1 cm were assigned to the upper part, and two to the lower part, with reference numbers from 1 to 5, from distal to proximal zone locations.

3D image registration.

In order to be able to compare both states, before and after broaching, it is necessary to achieve a correspondence for each slice acquisition, that is, we must be able to find coincident bone information in the same slice before and after broaching (in the areas that were not touched by the broach).

With this purpose we implemented an image registration technique to each pair of set of images (two sets per sample, before and after broaching) we made use of the image registration software *3D DataViewer* (DataViewer Software, V 1.5.2.4, Skyscan NV, Kontich, Belgium). The images of the bone before broaching are set as reference images, and they stay fixed during the registration procedure. While the images after broaching are repositioned according to the reference images. This semi-automatic repositioning method is based on the comparison of the intensity of the grey level of the images, and it is done in two steps. Only rigid transformations are applied, to the target images (images after broaching), specifically translation and rotation operations in the three axes (x , y , z).

The first step of the repositioning method utilized comprehends a manual manipulation of the images that allows to simplify and reduce the processing time of the second part of the procedure (automatic repositioning in 3D).

For the 3D automatic repositioning, the *truly 3D registration* method of the software *DataViewer* was used. It generates iterative repositioning steps simultaneously



Figure 5.10: Five measurement zones of 1 cm each (L1, L2, L3, L4, L5), shown on an X-ray image of one of the femur samples on the 3D analysis software *CTAn*, the red line indicates the anatomic center of the lesser trochanter. The zones go from 1 through 5, from distal to proximal, respectively.

in the three different planes and compares at each iteration the grey levels of the images, the grey level matching threshold and number of iterations can be controlled by the user. The images of the broached bone after registration are saved, as well as the reference images before broaching. A typical result of the registration procedure can be observed in Figure 5.11.

Segmentation of trabecular and cortical bone.

The segmentation methods utilized in this study were applied with the use of the 3D analysis software *CTAn* (CTAnalyser Software V 1.16, Skyscan NV, Kontich, Belgium). This tool offers the possibility of executing different tasks, such as analysis functions (binarization, 2D and 3D morphometry), as well as image processing operations (morphological operations, denoising, etc.). The segmentation operations were applied to the whole sequence of images of each sample. A circular structural element was used for all the morphological operations.

Our interest was to make the measurements of variation of BMD in the trabecular bone of the femur affected by the broaching. Hence, a segmentation of the trabecular bone from the cortical bone had to be done. The objective was to obtain a mask of the trabecular bone of the sample. For this, successive morphological and bitwise operations were applied on the sets of images before broaching.

The trabecular masks were extracted from the reference images (before broaching), since they were intact and had not suffered any structural modification of the bone tissue, making it easier to do the extraction, as can be observed in Figure 5.11. Then this mask could be adapted to the target images (after broaching) thanks to the 3D registration operation. *CTAn* proposes a segmentation procedure for the trabecular and cortical bone (Bruker, 2015), which served as a basis for the method that we developed and implemented.

As in the original algorithm the region of interest is not defined, the mask contains the whole image, we started by adding to the algorithm a section to apply a global threshold to the image with the purpose of separating the bone from the rest of the image. Figure 5.12 shows a superposition of a trabecular mask over its corresponding slice.

Bone/implant interface mask.

It can be observed in the images after broaching that there is an accumulation of trabecular bone on the walls of the broached cavity of the femur (Figure 5.11, right). In order to calculate the BMD close to the contact surface between the bone and the implant, it was necessary to extract a mask that corresponds to the regions affected by the broaching. This mask is applied to both sets of images (before and

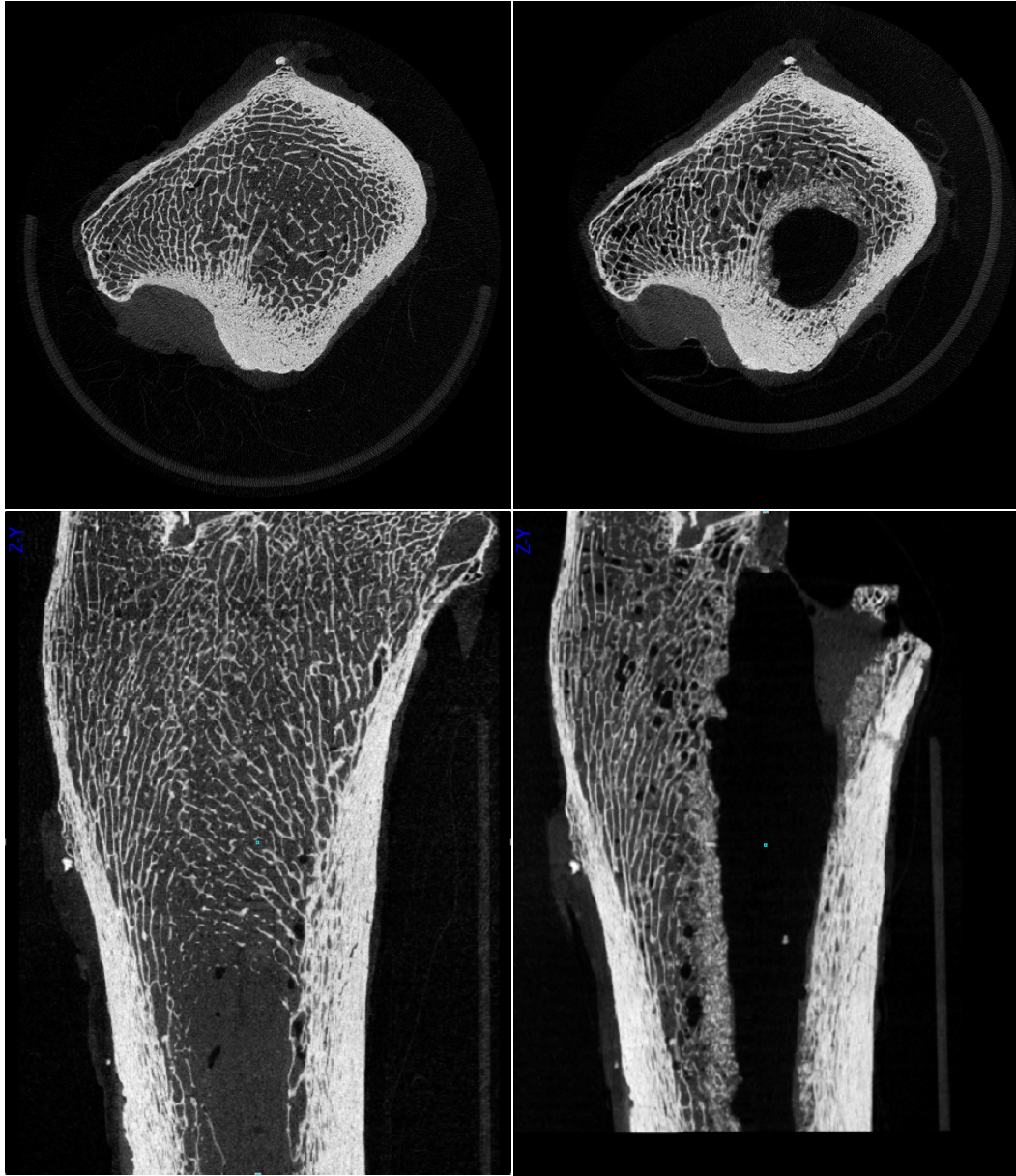


Figure 5.11: μ CT-Scan images of the sample 362, before broaching (left), and broached after the registration procedure (right). Top: axial views. Bottom: lateral views

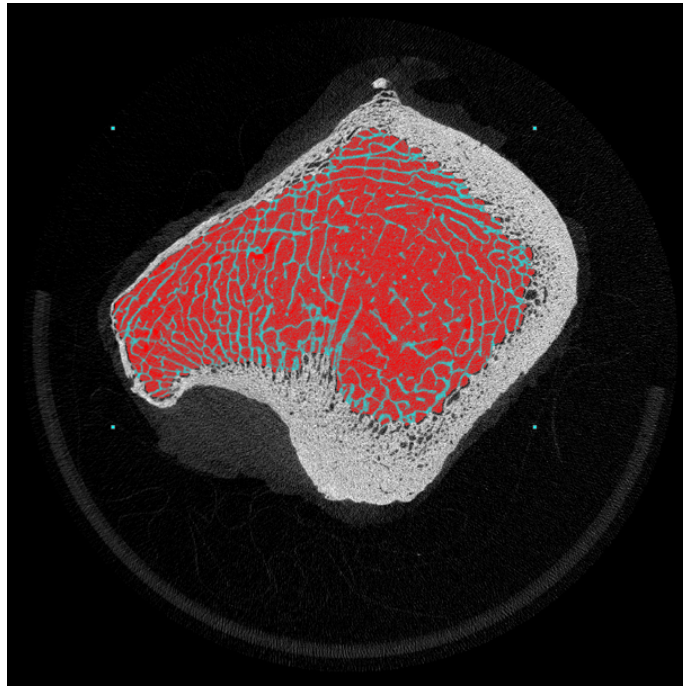


Figure 5.12: Trabecular bone mask over its corresponding μ CT-Scan image cut

after broaching) to measure the variation of BMD between both states. Figure 5.13 shows a superposition of these masks over their corresponding slices.

A succession of morphological and bitwise operations is executed on the images acquired after broaching for obtaining, first a mask of the whole broached region, and subsequently the mask of the compacted/crushed trabecular ring. Once the mask of the whole broached region was obtained, one more operation was implemented for obtaining the mask of the ring of compacted bone. A morphological operation of dilation of a size of 85 pixels was applied, which corresponds to an expansion of 3 mm ($85 \times 35,42 \mu\text{m}$). This size was defined by observing certain image slices from each sample on the software of 3D analysis *CTAn*, the rings of compacted/crushed bone had an average size (thickness) of 3 mm. From this point, the ring of 3 mm of broached bone will be denoted as *ring*.

Definition of angular sectors.

As previously stated, the analysis of the bone mineral density is done in the L1 - L5 zones along the region of interest of the broach. In order to obtain more precise results that reflect the distribution of variation in the contact zone between bone and implant, each one of the five zones is divided into 12 angular zones of 30 degrees each (Figure 5.14). Dividing each zone (L1 - L5) into different angular sectors allowed to characterize the local variation of the BMD for each sample. Separate

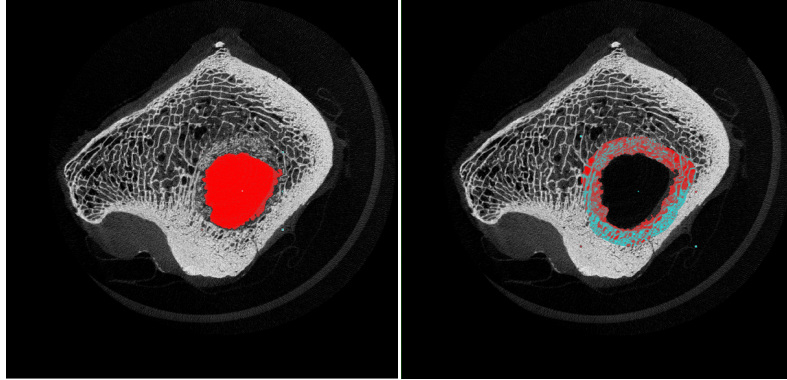


Figure 5.13: Example of a mask of the whole broached region on one slice (left). Example of a mask of the compacted/crushed bone ring on one slice (right).

masks were extracted for each of the angular sectors in the shape of an isosceles triangle with the main vertex in the center of the broached cavity (see Figure 5.14), due to the irregular geometry of the femoral cavity and the broaching tools (there is no axis of symmetry), it is not possible to define a common anatomic reference point in each slice of a sample, since this point will not have the same position in each image.

Furthermore, as the geometry of the broached area varies in each slice, in order to take into account these anatomical variations, the barycenter of the broached cavity was determined for each zone L1 - L5, which defines the center point of the triangles of the twelve angular masks (add figure barycenters). Another point to take into account for the extraction of the angular masks is that the analysis of the variation of the BMD is relative to the orientation of the prosthesis, or more specifically, of the broaching tool for that matter. In summary, each one of the five longitudinal zones has 12 angular masks of 30° , with an orientation axis defined in the largest zone (L5), this axis is obtained by calculating the major axis of the middle slice of the zone that passes by its barycenter. The orientation of this axis is then projected on the middle slice of each one of the other zones (L1-L4) to obtain the orientation axis of each zone, see figure ?? (bottom, right) for an illustration of these axes.

Masks operations

At this point, three different types of mask have been obtained. The first one is a mask that corresponds to the trabecular tissue, the second one is a mask that corresponds to the contact surface between the bone and the implant with a thickness of 3 mm, and the last one is a set of masks that corresponds to each of the 12 angular sectors. It should be noticed that the thickness of 3 mm is applied equally to all the masks and samples, and in most cases this region contains only compacted

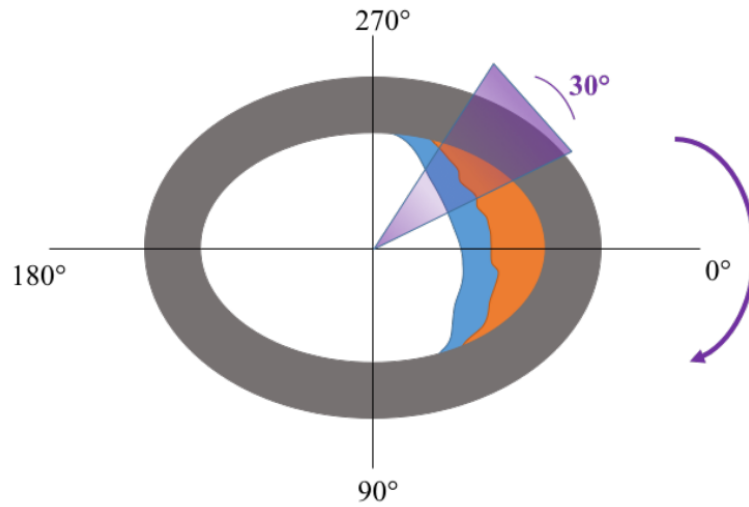


Figure 5.14: Scheme of the angular mask. The blue region corresponds to the trabecular bone before broaching. The orange region corresponds to the trabecular bone after passing the broach.

trabecular bone. However, in different regions of some samples it can be found that these 3 mm contain also parts of cortical bone, this can happen because in some cases the passing of the broach goes closer to the cortical wall, see Figure 5.15, left). As the purpose of the study is to assess the BMD variations in trabecular bone only (the region compacted with the broach), it was important to develop a technique to exclude the cortical bone in the required cases.

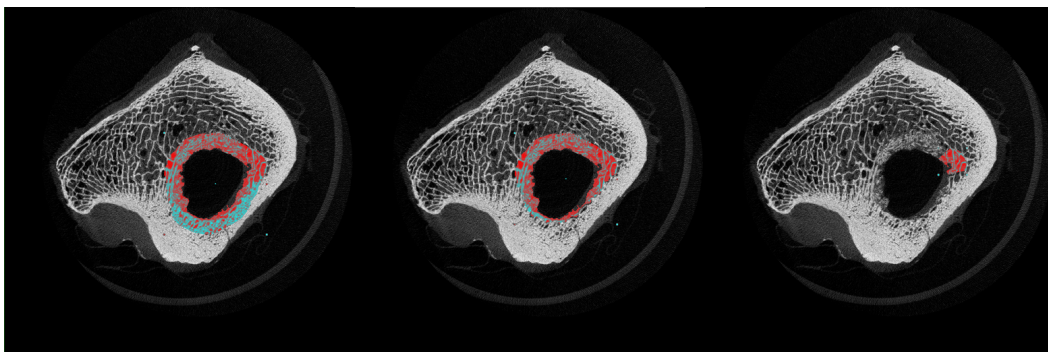


Figure 5.15: Masks of the middle image slice of the sample 362. Left: A = mask of the trabecular ring. Middle: B = A + whole trabecular mask. Right: C = B + angular mask 0-30°

5.3 Results

Samples 282, and 268 were excluded due to time constraints. Sample 376 was excluded because the day of the procedure only left-side broaching tools were available. Sample 261 was finally excluded due to technical issues with the bone segmentation algorithm with this sample. Leaving us with 4 samples in the end (362, 269, 283, and 331).

All samples experienced an overall increase of BMD in the ring with the broaching (Figure 5.16). Sample 362, presented the highest initial BMD (before broaching), and presented the highest BMD increase as well. This sample had been previously identified by the surgeon as a necrotic bone.

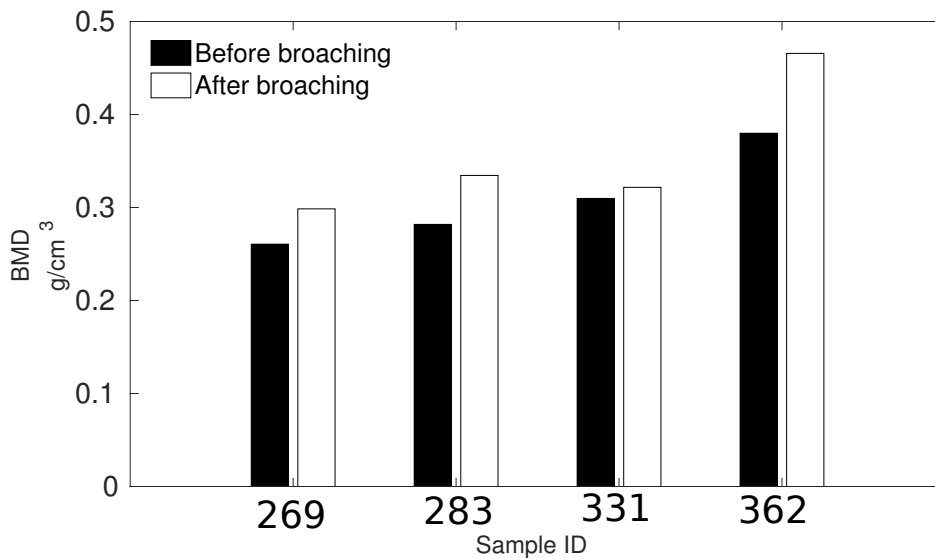


Figure 5.16: Total BMD per sample in the ring before and after broaching

In Figure 5.17 it can be observed that there is a higher BMD after broaching in each longitudinal zone (1-5). Zone 5 registers a smaller variation for most samples, except for sample 283, for which the variation of zones L1 and L5 are approximately the same. The BMD variation is negative in one case only, zone 5 of sample 331 and close to zero for zone 5 of bone 269. There seems to be a trend of variation with zones with higher to lower variations from distal to proximal zones; this trend is not observed for sample 283.

In Figure 5.18 we can observe the BMD distribution before broaching and the relative variation for sample 362, and for each one of the 12 angular sectors, for L1 - L5. It can be noticed that BMD concentrations due to broaching appear to reach higher levels in the farthest lateral locations of the broach (between angles 0° - 30° and 330° - 360°, and at the opposite side between angles 180° - 210°; this

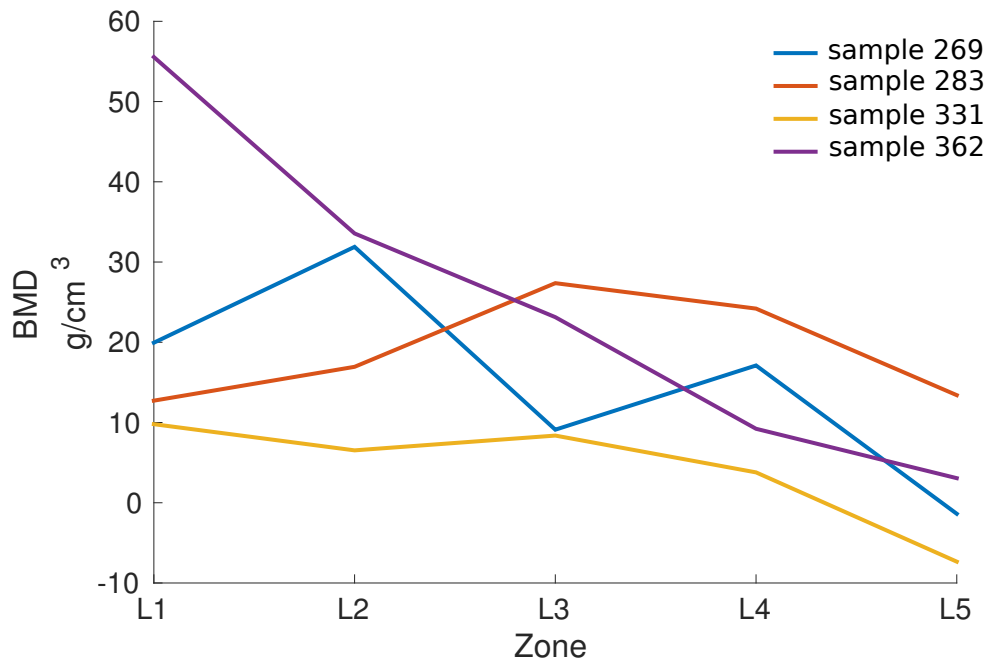


Figure 5.17: BMD variation for each sample and longitudinal zone (L1-L5)

observation applies for all the samples. In Appendix C we show the results for the rest of the samples in figures C.1, C.2, C.3.

Figure 5.19 shows the angular relative variations of all the samples for each zone L1 - L5 separately. It can be observed that all the zones present higher positive variations (in green) than negative variations (in red). It can be noticed too that the negative variations increase from distal to proximal zones, that is highest negative variation for L5 and lowest negative variation for L1; similar patterns were observed for all the samples. The blue line indicates the predominant BMD concentration axis, for all the zones the highest concentration was obtained at the lateral side between 300° and 360° . See Appendix D to observe the angular distribution of BMD (g/cm^3) before and after broaching, and the relative variation of BMD, of each sample separately.

5.4 Discussion

As far as we know, the results presented in this chapter are the first to describe the modification of bone microstructure due to broaching.

The presented results show that the broaching procedure causes an overall augmentation of the BMD levels in a 3 mm ring of trabecular bone around the cavity, particularly on the lateral areas (corresponding to 0° and 180° in Figure 5.18), with

higher concentration in the distal zones (L1, L2) which could be interpreted as a result of trabecular bone accumulation caused by the broach moving downwards. The lateral and medial concentration (at 0° and 180° , respectively) of BMD observed in all the samples is coincident with the location of the contact zone sizes defined in Chapter 4, which illustrates why these areas are often considered in the 3D planings as critical for proper implant anchorage. During the broaching procedure the surgeon had identified the sample 362 as a "necrotic bone", which means that its tissue is harder, which was clearly observed during cutting of the sample and the passing of the broaching tool, requiring a bigger effort for opening the cavity. This sample presented as well the largest overall BMD variations (figure 5.16); which suggests that larger BMD variations are associated to larger initial BMD levels.

As a limitation, we need to point out that in this study we used the same region of interest for all the samples (a longitudinal region of 5 cm of length) although the samples and broaches used were of different sizes, it should be noticed that this could have an effect in the assessment of variations.

Our findings reveal how the broaching procedure may have an effect on 3D surgical planning, which is done with preoperative CT-images without considering the broaching effect. In other words, the overall positive variation of BMD originated by the broaching procedure renders the contact area possibly more stiff and adequate for a good anchorage, this actual bone quality in the contact surface is as a result underestimated by the planning, which uses scanned images that are obtained before the broaching is done. However, modifications of surface mechanical properties (stiffness) can hardly be deduced from the BMD values because part of the bone is crushed, and this is not detected in the scanned images.

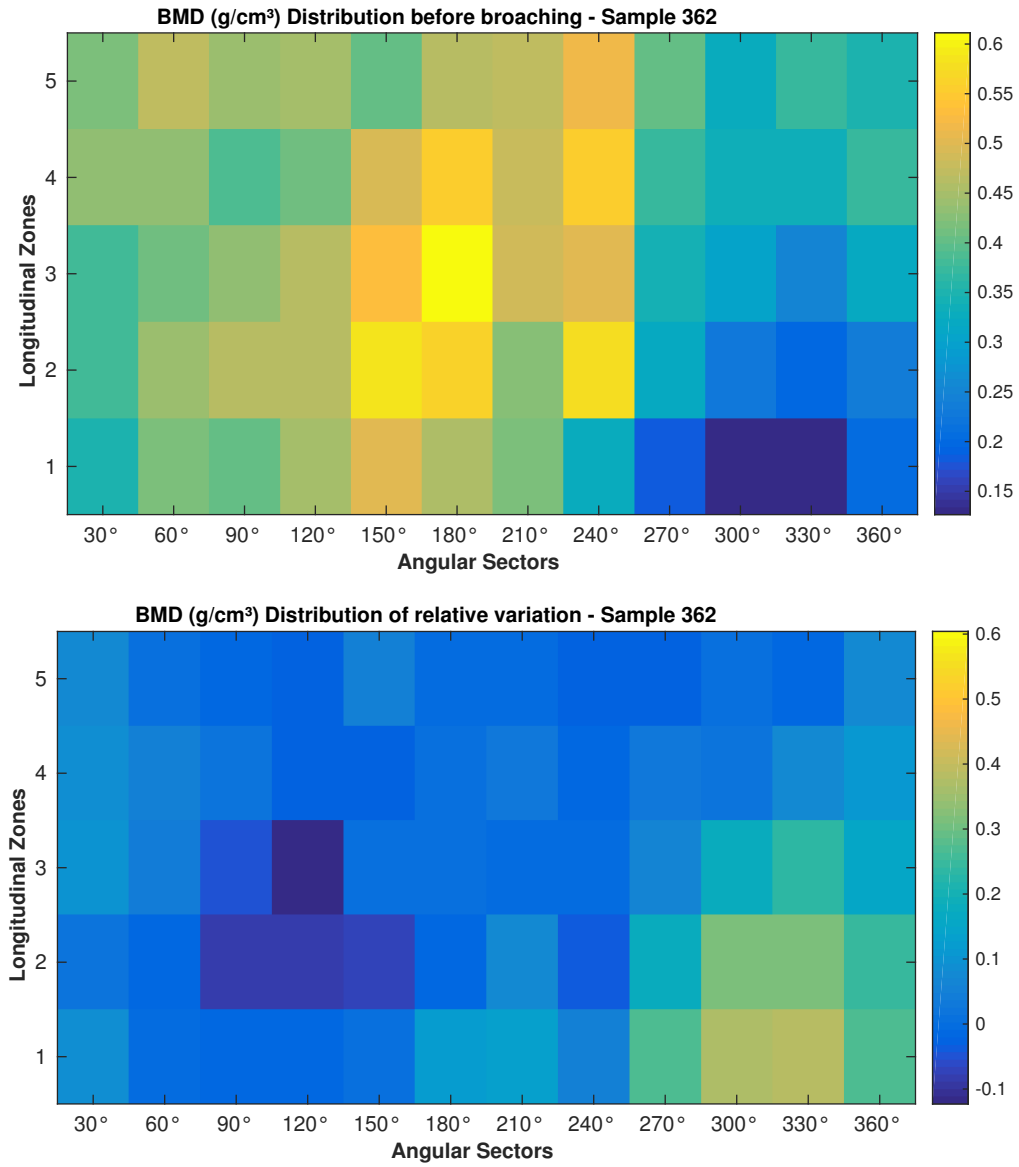


Figure 5.18: BMD Distribution before broaching (top) and relative variation after-before broaching (bottom) - normalized for sample 362

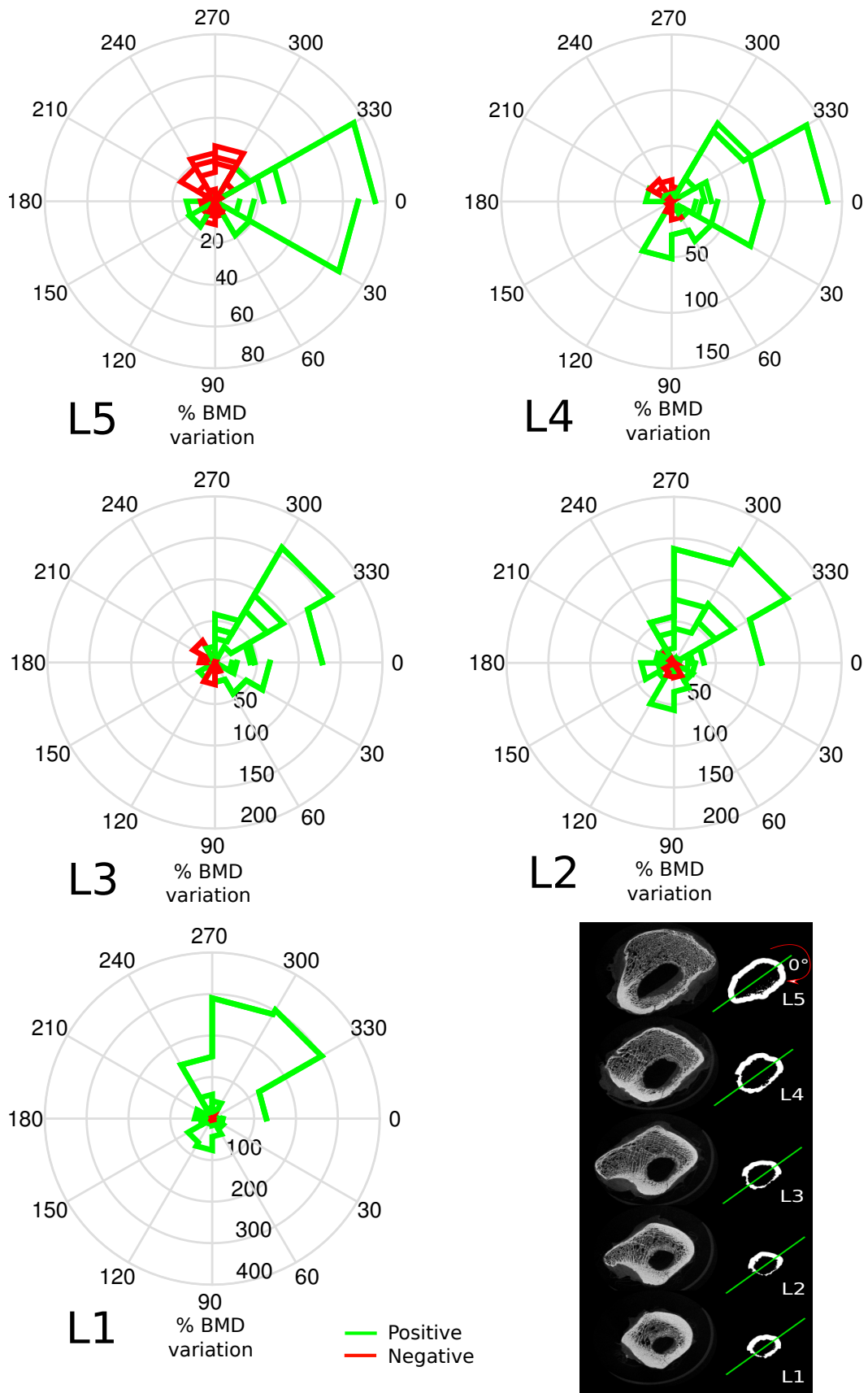


Figure 5.19: Angular BMD relative variation for each zone L1 - L5, for all the samples, positive variations are shown in green and negative variations in red. The image at the lower right side illustrates the middle slices that correspond to each zone L1 - L5, for the sample 362 as a reference, with the axis (in green) that indicates the 0° angle of measurement for each zone.

Mechanical characterization of the bone-implant interface after broaching

6.1 Introduction

In chapter 5 we introduced the idea and context for the study and characterization of the broached femoral cavity through the analysis of the BMD distribution obtained from μ CT-Scan images, for potential applications and considerations in 3D preoperative planning of THR. Now, in this chapter, following the same purpose of characterization of the broached bone for THR; we present a study concerned with the measurement and analysis of the mechanical properties of the trabecular bone compacted in the femoral canal by the effect of the broaching procedure for THR.

We are interested in the characterization and analysis of the mechanical properties of the compacted trabecular bone, 1) in a localized manner to be able to construct a mapping of the mechanical properties that the compact bone exhibits after being broached, 2) at a millimeter scale, since what we search is the mechanical properties that affect the stiffness of the bone-implant interface.

With this purpose we developed a protocol for local measurement of mechanical properties of the bone through a mechanical test of indentation to characterize the bone-implant interface zone after the broaching procedure. In a nutshell, it consist of the local measurement of force-displacement relations by means of indentation, and subsequent relation with the Young's modulus through different equations proposed in the literature.

It is important to mention that usually the studies involving mechanical tests of the trabecular bone are done on controlled samples, that is, extracted from some specific bone site for the experiment, with well controlled geometrical properties and measurement orientations, and following different existing protocols for the measurement of mechanical properties of the bone. Our case is particular in this sense though, since we are interested in the local measurement of mechanical properties of the compacted bone as it is left in the cavity by the passing of the broaching tool. Our samples cannot be cut and extracted from the bone specimens, since this would most likely affect the original configuration of the compacted bone.

The present study was developed the following main goals:

1. To determine the real mechanical properties of the bone in contact with the prosthesis after a THR surgery, which to this date are unknown.

2. To find relations between the BMD distribution findings of chapter 5 and the mechanical properties of the broached bone.
3. One implicit objective was to build an indentation device using an universal testing machine.

Just as the study of BMD variations presented in chapter 5, the assessment of mechanical properties in the bone-implant interface zone after broaching and subsequent correlation to BMD values obtained from CT-Scan images, could also provide great advantages for the advancement of 3D preoperative planning techniques, and THR implantation protocols in general, since this would reveal the boundary conditions of the broached/compacted bone that affect the anchorage of the implant inside the bone; to this date this information is completely unknown and could have an important impact in the accuracy of these procedures.

6.2 Bone Preparation and preservation

The same samples described in Chapter 5 were used for the indentation study. Same temperature handling, and thawing considerations as in 5 apply for this chapter too.

As part of the protocol, the bones were cut longitudinally in two halves and defatted to get them prepared for the indentation test.

Longitudinal section of the bone

A longitudinal lateral section of the bone is made to leave exposed the surface where the mechanical tests will be executed, as shown in Figure 6.1.

The samples were previously thawed, and then securely fastened with a bench vise to the desired position to make the cut, the surgeon used a surgical oscillatory saw to make a lateral cut of the bone and expose the internal surface, the length of the samples was also reduced by removing the distal part to better adapt the samples to a mounting system for the indentation test (Figure 6.2).

Defatting

Bone specimens were defatted according to the standard procedure used in our laboratory and validated by other ex-vivo studies (Tang et al., 1996; Granke et al., 2011). This protocol prevents the risk of infections and guarantees the sample conservation at room temperature. Briefly, the procedure consists of the following steps: (1) rinsing in saline at ambient temperature; (2) defatting for 18 hours using a chemical bath of diethylether and methanol (1:1) at room temperature; (3) removing the excess of chemical fluids rinsing in a distilled water bath and draining-off in absorbent paper.

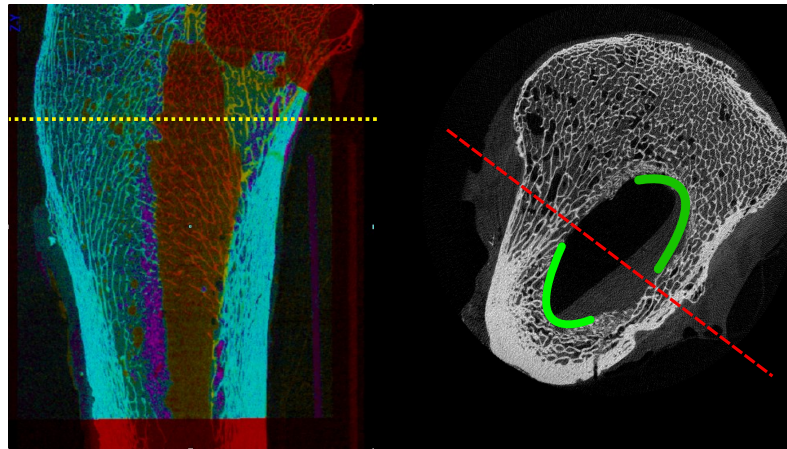


Figure 6.1: Scheme of the longitudinal cut of the bone and anatomical references identified by the surgeon. The red dotted line indicates the line of the longitudinal cut, that separates two anatomical reference spots (curved lines in green) which indicate the areas of interest to be indented.

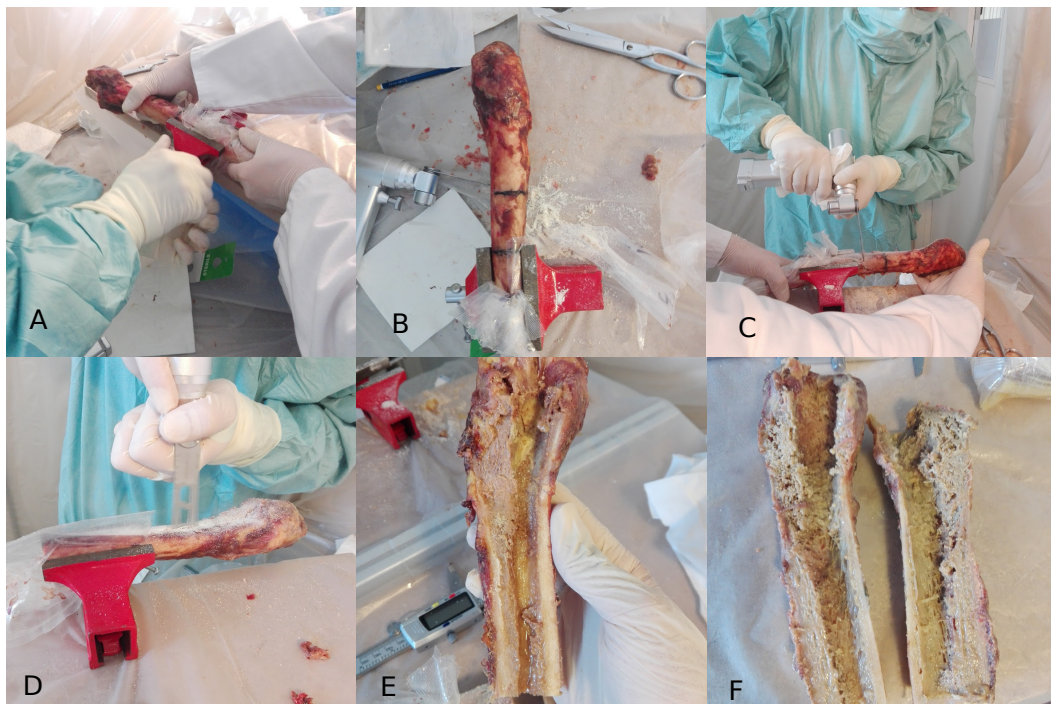


Figure 6.2: Different steps for the longitudinal and length cut of the samples. Fixation of the bone with the vise (A,B). Cut to reduce length of the bone (C). Longitudinal cut of the bone (D). Internal surfaces of the bone cavity after the cut exposing the broached region (E, F).

Bone Hydration

When bone is dried, the Young modulus increases but the toughness decreases. Its ductility can be recovered by re-wetting in buffered physiological saline. It takes about 3 hours to recover their wet weight completely (Turner and Burr, 2001). In this study, several stages during testing involved lost of hydration.

As samples of large size are used in this work, they were left to hydrate during 18 hours approximately before any test was done.

6.3 Overview of indentation testing

The indentation test was performed with the use of a universal testing machine. Adaptations of this machine were required for proper sample holding. Spherical indenters were used to penetrate perpendicularly in the broached bone and acquire load-displacements relations.

6.3.1 Sample mounting and testing devices

6.3.1.1 Bone holding device

As the bone possesses a very irregular shape, it could not be easily mounted on the base of the mechanical tests machine, thus, it was necessary to create a holding device to keep the bone in the desired position for the test, making sure that the configuration is stable enough to avoid noise during the indentation, but not too tight to prevent excessive compression effects over the sample.

An u-shaped half steel - half aluminum profile cut to the length of the indentation area of the bone was used to create a holding base. It was important to have half of the holding device made of steel to guarantee proper attachment to the mobile magnetic system used for mounting the sample on the test machine, and which allowed to set different orientations for the test. The u-shaped base was partially filled with epoxy resin, the bone sample (each cut side separately) is introduced and positioned in the epoxy (Figure 6.3), the external surface of the bone is sprayed with *teflon* before positioning to avoid excessive adherent effects.

Once the bone was introduced in the desired position, four hexagonal bolts are introduced close to the bone to fix it in that position, the heads of the bolts are inserted in the epoxy and positioned closely to both lateral sides of the bone, then the rest of the u-profile is filled resin reaching a level high enough to maintain both bone and screws secured to their position, finally the assembly is left to dry. Plain washers and nuts screwed to the bolts were used to fasten the bone.

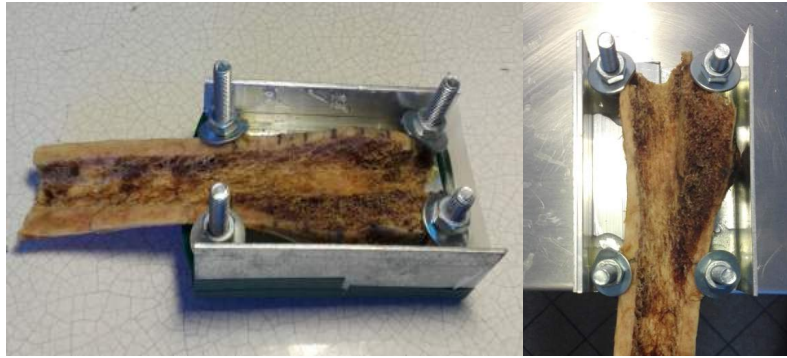


Figure 6.3: U-shaped half steel half aluminum bone holding system, with a bone sample held in place with epoxy and four hex-bolts.



Figure 6.4: Set of screwed indenters ranging from M4 to M24 (indenter diameter 2,5 mm to 18 mm).

6.3.1.2 Indenters and their adaptation device

According to the literature, bone indentation tests are usually done with the use of a blunt-end indenter ranging from 2,5 to 6 mm in diameter, at a displacement rate of 2 mm/min and to a depth of 0,2 to 0,5 mm. A load-displacement curve is created as the indenter penetrates the sample (Turner and Burr, 2001).

For our test it was decided to use a set of spherical indenters, a set ranging from M4 to M24 - indenter diameter 2,5 mm - 18 mm (Figure 6.4) was available for our use.

As the MTS mechanical tests machine that we used does not provide the option of adapting indenters, a connecting device was designed and manufactured for this end; the proposed design is presented in (Figure 6.5). One screwed plug was manufactured in steel for each one of the indenters, these plugs go inserted into a

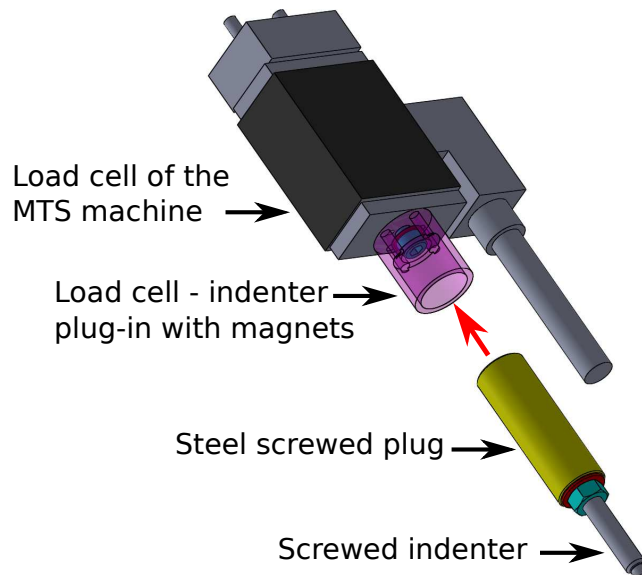


Figure 6.5: Different parts of the indenter connecting device.

connecting piece common for all the indenters which goes screwed to the load cell of the machine, small magnetic rods are inserted in the connecting piece and serve to attach the iron screwed plugs to the system.

6.3.1.3 Orthogonality verification system

A 2-degree-of-freedom magnetic mounting system allows to set the bone to the desired positions aligning the indenter orthogonally to the marked indentation points on the bone. A circular magnetic chuck (Figure 6.6, top left) and an inclinable magnetic base (Figure 6.6, top right) are used to fix the samples to the desired position. Both devices together provide rotation around one axis and horizontal translation, making possible to access orthogonally, and with relative ease, most of the desired spots on the internal surface of the bone (Figure 6.6).

In order to verify the orthogonality between the indenter and the bone's surface, a laser pointer is centered and adapted to the indenter plug-in device. A reflecting marker, a 4,5mm diameter mirror obtained from an endoscopic camera (Figure 6.7, top left and top middle) is located over the desired test spot on the surface of the bone so it reflects back the laser beam (Figure 6.7, top right), and by making it coincide with the beam source the orthogonality is verified (Figure 6.7, bottom).

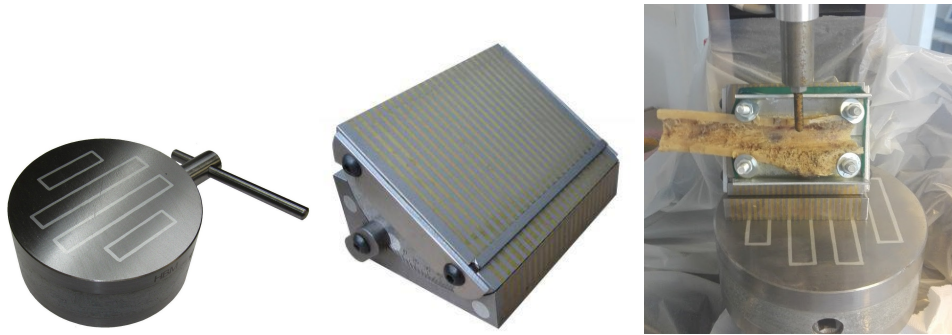


Figure 6.6: Circular magnetic chuck (left - Source: <http://www.rdgtools.co.uk/acatalog/>). Reclinable magnetic base (middle). Assembly of the components for sample mounting on the machine (right).

An orthogonality test was performed to determine the amount of error generated by a deviation from the perpendicular axis.

6.3.2 Definition of indentation spots

A grid of 15 points (3 columns, 5 rows) was selected for all the samples (Figure 6.8). The internal surface of the bone was carefully marked with a permanent marker, creating a grid of spots of the places where the indentation tests had to be done (Figure 6.8, middle). The indentation spacing should be 1,5x - 2x the length of the diameter of the indentation mark (An and Draughn, 1999), in our case an indenter with a diameter of 4 mm was used, and a spacing of ≈ 1 cm was selected.

It is worth mentioning that a visual inspection was done by making use of the μ CT-Scan images, to make sure that the definition of indentation spots were as close as possible to the segmentation of the region of interest done in chapter 5, which would simplify later on the association of mechanical properties values from the indentation and the BMD values from the imaging work.

6.3.3 Mechanical test of indentation

Theoretical considerations for indentation.

Different relations and theoretical considerations found in the literature were considered for obtaining the Young's modulus of the bone from force-displacement relations measured by means of an indentation test. The preliminary tests with materials with known mechanical properties (Young's modulus) served to determine what equation provided the best results for our protocol.

For the application of these relations the following hypothesis are taken into account: homogeneous, isotropic, semi-infinite linear elastic-plastic half-space, no



Figure 6.7: From left to right (top): mirror of an endoscopic camera - VOLTCRAFT - 4,5 mm diameter (top left and middle - Source: <http://www.fonetip.cz/>). Laser beam pointed at the mirror placed on the bone's surface on a test spot. Laser beam reflected back to the beam's source with the mirror to verify orthogonality (bottom).



Figure 6.8: Different steps for the definition of indentation spots. A fine rope with evenly separated marks is used to make the grid (left). A permanent marker is used to mark the spots for the indentation, 3 columns, and 5 rows (middle). Reference names are associated to each spot with numbers from 1 - 5 for the rows, and the letter L, O and R for the columns (right).

time-dependent deformation mechanisms such as creep or viscoelasticity, and frictionless contact.

Turner and Burr (2001) state that when the indenter penetrates the bone and a force-displacement curve is created, the Young's modulus can be calculated by making use of the relation proposed by Timoshenko (1970) for a load distributed over a part of the boundary of a semi-infinite solid:

$$E = S \times \left(\frac{1 - \nu^2}{d} \right), \quad (6.1)$$

with S the slope of the load-displacement curve; ν the Poisson's ratio of the bone; and d the diameter of the indenter.

This theory does not comprehend specific considerations for: spherical indenter, unloading stage at the top of the slope.

Sumner et al. (1994) performed an indentation test on canine trabecular bone of the proximal tibia (indenter diameter 2.49 mm, indentation velocity 2 mm/min, and maximum indentation depth 0.2 mm). They obtained load-displacement curves that related to the Young's modulus by implementing equation 6.1. They made comparisons with mechanical properties of the human trabecular bone (compared with regional averages for healthy young human ~ 400 MPa) and established correlations with the measurement sites. Concluding that the use of the equation proposed by Timoshenko (1970) (equation 6.1) provided results highly correlated with non-destructive results on bone specimens, and that indentation load-displacement measurement is useful for obtaining the Young's modulus of the trabecular bone.

The method proposed by Oliver and Pharr (2004) also allows to obtain the Young's modulus from indentation mechanical test data. It applies for a variety of mechanical indenters, including spherical ones. This method is set for the unloading stage after indentation, since it is assumed that only the elastic displacements are recovered during unloading, facilitating the analysis since it excludes plasticity effects. The proposed equation is based on what they called the *effective Young's modulus* (E_{eff}), which takes into account the fact that elastic displacements may occur in both, the specimen, and the indenter. With the Young's modulus of the specimen given by equation 6.2.

$$E = \frac{1 - \nu^2}{\frac{1}{E_{eff}} - \frac{1 - \nu_i^2}{E_i}} \quad (6.2)$$

With E and ν , and E_i and ν_i , the Young's modulus and Poisson's ratio of the specimen and the indenter, respectively.

The *effective Young's modulus* is obtained from the following equation (Eq. 6.3), which relates the stiffness during unloading S and the E_{eff} ;

$$S = 2\sqrt{R} * E_{eff} \times (h - h_f)^{1/2} \quad (6.3)$$

In this equation (equation 6.3) with applications to spherical indentation (spherical indenter), considerations of Hertzian elastic contact are taken into account meaning that R relates the radius of the indenter R_1 and the radius of the indented surface R_2 , as follows:

$$R = (1/R_1 + 1/R_2)^{-1} \quad (6.4)$$

For plane-sphere contact according to Hertz theory (Aublin, 1992), $R_2 = \infty$, then R is simply the radius of the indenter.

In equation 6.3 the displacement h is taken as the maximum displacement of indentation for unloading case considerations, and h_f is obtained from geometrical relations of displacement illustrated in figure 6.9 presented in Oliver and Pharr (2004).

Figure 6.9 shows an schematic representation of the geometrical parameters that are taken into account for the unloading analysis of indentation, and used in equation 6.3

These equations take into account application for spherical indenter, unload stage, top of the slope. This upper part of the slope (circled in red) of the curve also known as the contact stiffness, see Figure 6.10.

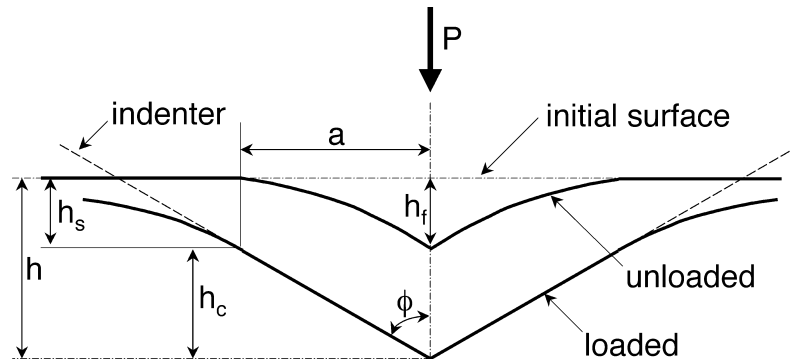


Figure 6.9: Schematic illustration of the unloading process showing parameters characterizing the contact geometry. Source: Oliver and Pharr (2004).

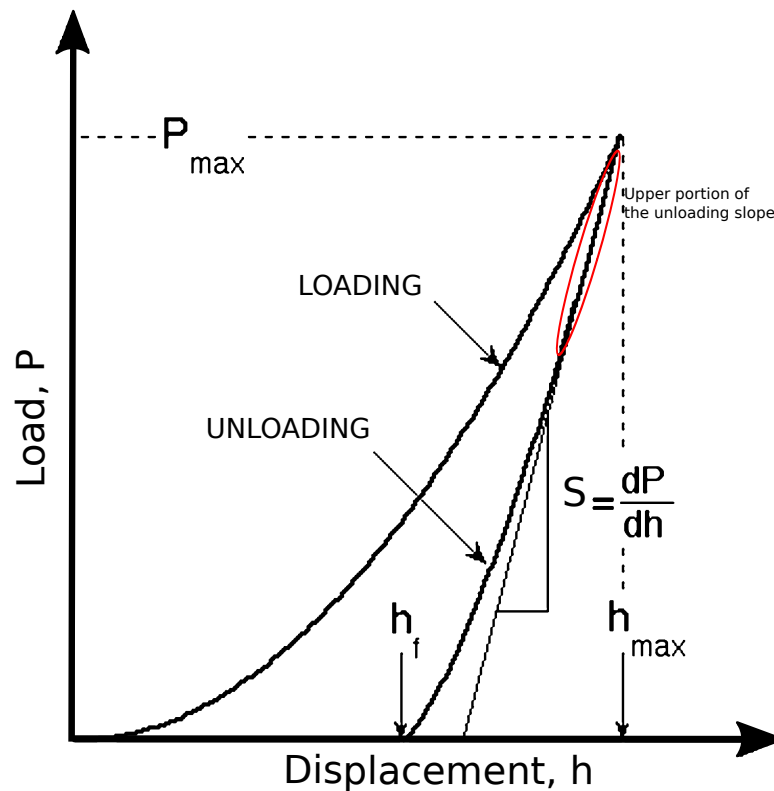


Figure 6.10: Schematic illustration of indentation load vs. displacement data showing the upper portion of the slope of the unloading curve. Reproduced from: Oliver and Pharr (2004).

The results were also analyzed in terms of the contact stiffness, which involves a simple calculation of the slope of the upper portion of the unloading stage of the load-displacement curve (Figure 6.10), and defined as:

$$S = \frac{dP}{dh} \quad (6.5)$$

With S the contact stiffness, dP the load variation in that portion of the slope, and dh the displacement related to that portion of the slope.

6.3.4 Preliminary mechanical tests

A series of preliminary mechanical tests were performed in order to gain a better understanding of the functionality, advantages and limitations of the universal test machine, and to test the protocol to be implemented in the following stage of the study with the actual bone samples. The preliminary tests were done on different types of material: first on sawbone (biomechanical test material which is primarily used in testing of orthopedic implants, instruments and instrumentation as an alternative testing medium to human cadaver bone - sawbone catalog, www.sawbones.com), polycarbonate, aluminum, then on bovine bone, and finally a test on a broached bone sample that was not part of the cohort.

For these preliminary tests, different parameters involved in the indentation tests were identified, such as: diameter of the indenter, displacement rate (velocity of indentation), maximum depth of the indentation (Oliver and Pharr, 2004).

Overall, the tested parameters were the following:

- Diameter of the indenter (Di): 3, 4, 5, 6 (mm).
- Displacement rate (v): 2, 3, 5, 10 (mm/min)
- Maximum indentation depth (Mid): 0.3, 0.4, 0.5, 0.6 (mm).

The ranges of values of the tested parameters were taken from suggested values found in the literature and other indentation works on bone (Oliver and Pharr, 2004; Turner and Burr, 2001; Sumner et al., 1994). They were also defined by observation based on repeatability and convergence to known Young's modulus values, particularly that of the polycarbonate.

Different combinations of parameters were tested to evaluate consistency and repeatability. The first trials were done on flat samples of sawbone and polycarbonate to verify repeatability and the optimal combination of testing parameters to obtain a Young's modulus close to a known value for this materials. Subsequently, we performed tests on bovine bone to learn how the protocol adapts to bony material.

Then, finally we did the test on the sample of broached femoral bone, making the necessary adjustments of parameters and verifying repeatability.

Additionally, a study based on the Hertz theory was carried out to verify results of the experiments and analytical solutions.

All combinations of Mid and v were tested with each Di , and force-displacement data was acquired at a rate of 1000 data points per second. Five repetitions were done for each combination of parameters to evaluate repeatability. The five repetitions were executed on the same indentation spot, with the aim of assessing two different indicators, repeatability and effects of resilience time (viscoelastic effects). A grid was created on the sample to define the indentation spots. These were selected leaving a minimum of twice the diameter of the indentation between spots.

We registered both loading and unloading stages and controlled the time between repetitions, and the time of penetration. More specifically, the indenter descends and stays in loaded position a time $t = 5$ sec, then unloads going back to the initial position and pauses for 5 seconds again, same process for a number of $N = 5$ repetitions. The purpose of doing this is to account for viscoelastic effects and control the resilience time, giving the time for the sample to "recover" before continuing with the next repetition.

The criteria for identification of the correct combination of parameters was based on the convergence of load vs. displacement values obtained with five repetitions on the same spot, using bone as the testing material.

6.4 Results

6.4.1 Results preliminary tests

Tests with sawbone

The following parameters were taking into account: $Di = 3$ mm, $v = 1$ mm/min, $Mid = 0.2, 0.3, 0.4$ (mm). Lack of consistency was found in some cases in the preliminary tests with sawbone, with very variable values of Young's modulus, probably due to its orthotropic characteristics.

Tests with polycarbonate

The second round of tests was done on polycarbonate, this material is expected to exhibit more isotropic characteristics as compared to sawbone. With a Young's modulus between 2.0 - 2.44 GPa (Materials Data Book, 2003 Edition, Cambridge University).

For indenter diameter 3 mm, velocity 2 mm/min, indentation depth was varied between 0.6 - 0.9 mm, obtaining convergence to a value of $E = 2.15$ GPa, at indentation depth 0.9 mm, and obtaining a maximum force around 700 N. Figures 6.11 shows an example of the curves load-displacement obtained for the polycarbonate,

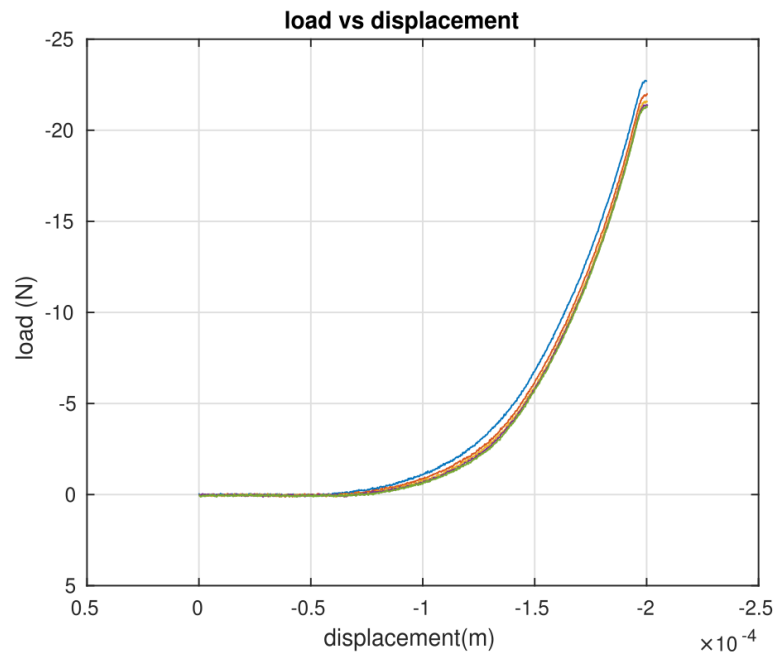


Figure 6.11: Load vs. displacement curves, unload stage, five repetitions, material: polycarbonate

and 6.12 the segment of the top of the slope selected for calculations of Young's modulus and contact stiffness. The extent of the segment of slope was selected visually based on considerations of how straight the segment is, required for the use of the equations proposed by Oliver and Pharr (2004).

One thing that was noticed in the tests with sawbone and polycarbonate samples was that for larger sample surfaces, the uneven areas between the holding surface used and the sample provoked noise in the test, we cut the samples into smaller pieces and the noise was reduced. This gave us an example of the necessary level of flatness when designing the mounting system for the real bone samples. The high repeatability of the results obtained with the polycarbonate, allowed to verify the robustness and accuracy of the indentation protocol.

Tests with bone sample

The data obtained from the preliminary tests with the bone sample was processed using the different indentation theories found in the literature and previously presented in this chapter, a summary of some of the obtained results is presented.

From equation 6.1 (Timoshenko, 1970; Turner and Burr, 2001):

Diameter: 3 mm, Velocity: 1 mm/min, Penetration: 0.4 mm. The average Young's modulus obtained was: 0.24 GPa

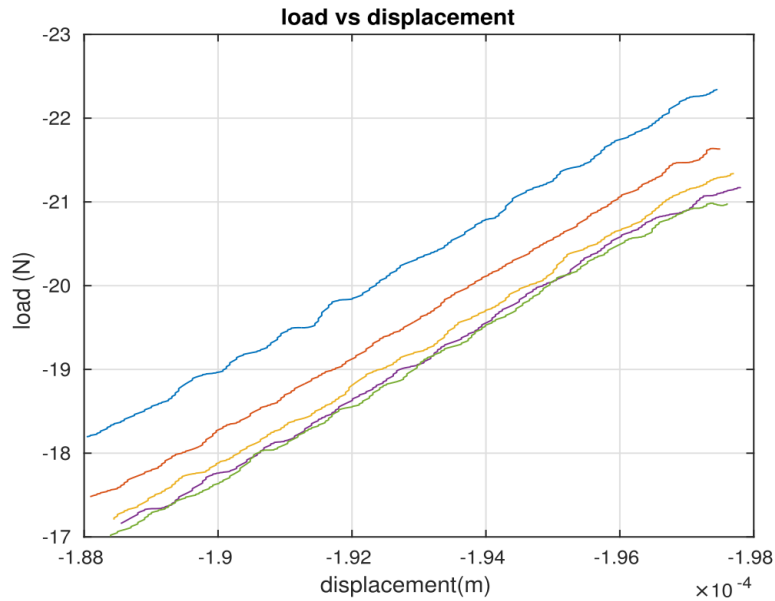


Figure 6.12: Upper portion of the load vs. displacement curves, unload stage, five repetitions, material: polycarbonate.

From equation 6.2 (Oliver and Pharr, 2004):

Diameter: 3 mm, Velocity: 1 mm/min, Penetration: 0.4 mm.

Obtaining an average Young's modulus of: 0.49 GPa

It is not an easy task to compare the obtained values of Young's modulus of the trabecular bone with values reported in the literature. First, there are still major debates about the ranges that can be taken into account for the trabecular bone (Rho et al., 1998), a reference study on trabecular bone at the proximal tibia reported values around 0.65 GPa (Hvid1985). Second, our indentation study was performed on a surface where the trabecular bone has been compacted by the passing of the broaching tool, making it even more challenging to compare our values with other reported values from studies done on intact bone. For these reasons it was decided to select our testing parameters based on repeatability and convergence of our results from the tests.

Finally, the best convergence and repeatability with the bone sample was obtained for a diameter of the indenter (D_i) of 4 mm, displacement rate (v) of 2 mm/min, maximum indentation depth (M_{id}) of 0.3 mm. Also, it was decided to make use of the equations proposed in the works of (Oliver and Pharr, 2004) (equation 6.2), since they are designed to take into account a majority of factors that could have an impact in our study, such as viscoelastic and plastic effects, and possible deformations of the indenter.

The study of the orthogonality effect, which measured the amount of error obtained if the indenter does not penetrate perpendicularly into the bone surface, showed that a deviation 5° from the perpendicular axis would generate an error of the maximum load of around 6%, while a deviation of 10° would generate a maximum load error of around 100%. However, the Young's modulus was not affected by this load changes generated by angular deviations of 5° and 10° , for both cases the Young's modulus was around 2 GPa, which corresponds with the result obtained with zero angular deviation, and also the close to the values reported in the literature for the polycarbonate. However, as this results were obtained for a flat surface of polycarbonate, for the experiments with the bone we decided to limit the deviation to a maximum of 5° . In other words, the laser beam had to be projected inside an area of 3.5 mm of radius maximum located at a distance of 15 cm from the sample to ensure that the error does not exceed 5° (see Figure 6.7). For more details see Appendix E.

6.4.2 Results of broached bone - study samples

These results are presented in two parts, first we use the contact stiffness, obtained with equation 6.5, to describe the range of stiffness values obtained with our tests. Then we use the Young's modulus, obtained with equation 6.2, to describe the spacial distribution of the obtained results. Notice that both contact stiffness and Young's modulus are directly proportional, and we could use one or the other to explain our results.

6.4.2.1 Range of stiffness values

Figure 6.13 shows the distribution of stiffness values for each one of the samples. All the samples show a concentration of values around a stiffness of 10^4 N/m, with some values in the range of 10^5 N/m, except for the sample 362; for which the majority of the indentation spots presented values around 10^5 N/m. Figure 6.14 shows the stiffness values distribution for all the samples together, with a minimum and maximum stiffness values of $3.51 \cdot 10^3$ N/m for the sample 283, and $1.02 \cdot 10^6$ N/m for sample 362, respectively.

6.4.2.2 Young's Modulus - Spacial distribution

Results are presented for each one of the samples (Figures 6.15, 6.16, 6.17, and 6.18). A Young modulus mapping was obtained by making use of the equations presented previously and proposed by Oliver and Pharr (2004). The mapping is presented in two images for each sample, as side 1 and side 2, corresponding to the two halves obtained after the longitudinal cut.

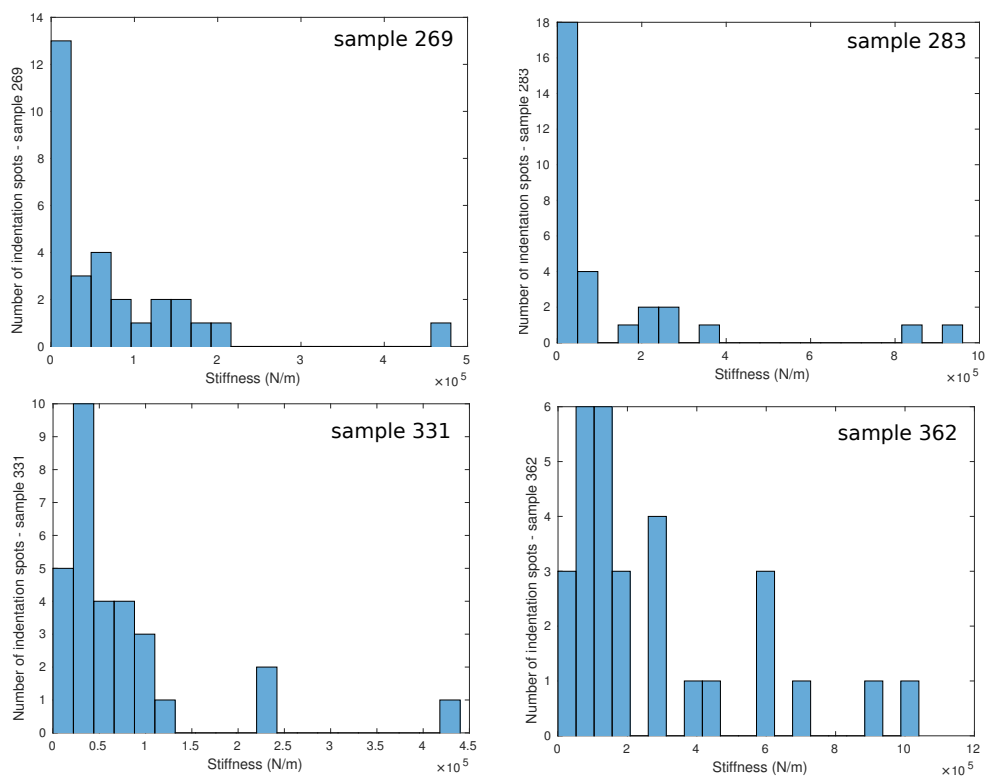


Figure 6.13: Histogram of the stiffness (N/m) distribution of each one of the samples separately

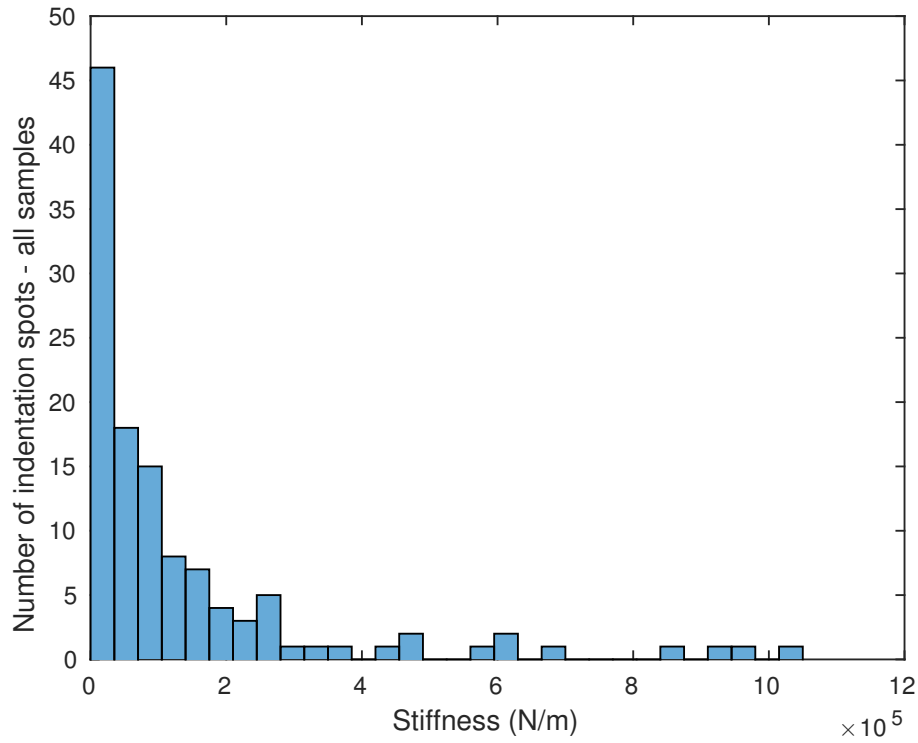


Figure 6.14: Collective histogram of the stiffness (N/m) distribution of all the samples

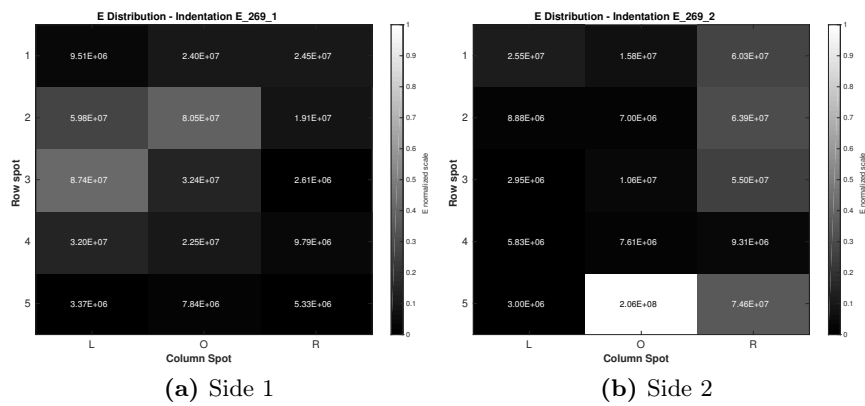


Figure 6.15: Young's modulus (E) distribution obtained from the indentation results - sample 269, both sides.

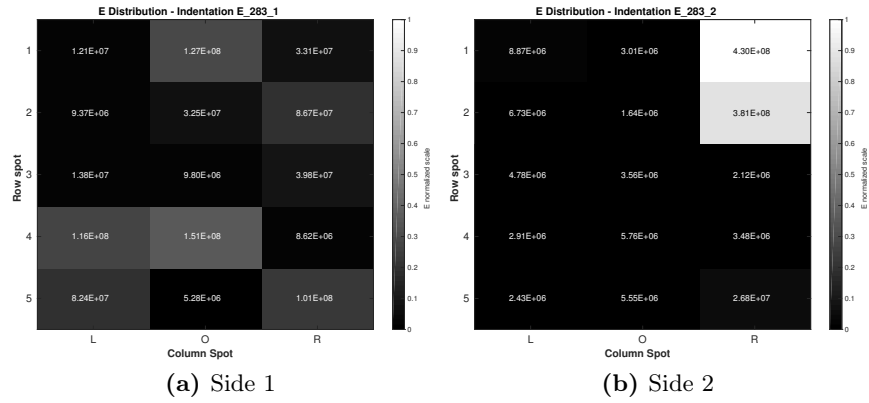


Figure 6.16: Young's modulus (E) distribution obtained from the indentation results - sample 283, both sides.

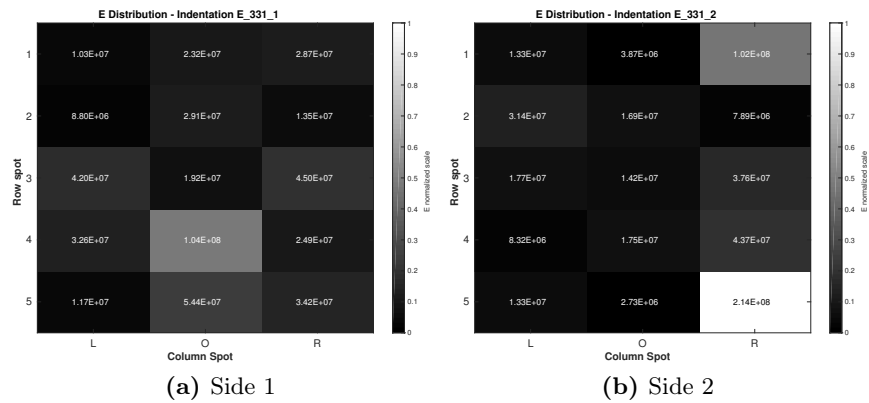


Figure 6.17: Young's modulus (E) distribution obtained from the indentation results - sample 331, both sides.

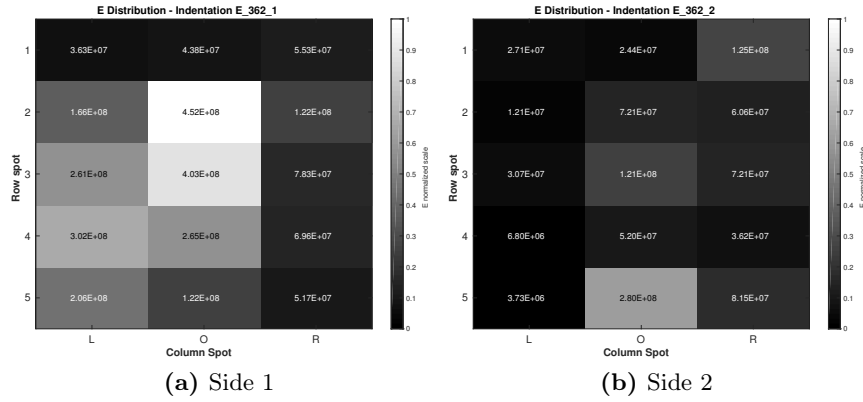


Figure 6.18: Young's modulus (E) distribution obtained from the indentation results - sample 362, both sides.

The highest E values were obtained for the sample 362 ($4.52 \cdot 10^8$ Pa). For this sample in particular it can be observed that the highest values are mostly concentrated in the "O" column. The rest of the samples present a rather heterogeneous distribution of E .

6.5 Discussion

6.5.1 Analysis of contact stiffness results

Let's consider the results obtained for the contact stiffness and presented in figure 6.13, as previously mentioned the majority of stiffness values were obtained in the range between 10^4 N/m and 10^5 N/m for the ensemble of the bone samples. Now if we consider that these values were obtained with a local measurement of the load-displacement curve, with the use of an indenter, we could assume that each separate measured value of contact stiffness corresponds to the area of the spot of measurement.

This area corresponds to a segment of surface of a sphere (the indentation sphere) and can be calculated as:

$$A = 2\pi * r * h \quad (6.6)$$

Where A is the area of the indented surface, r is the radius of the indenter (4 mm), and h is the penetration of the indenter which in this case corresponds to the maximum depth of penetration which was set to 0.3 mm. This calculation corresponds to an area $A = 3.78 \cdot 10^{-6} m^2$

If we take into account the results obtained in chapter 4, we can observe in figure 4.5 that the transition from unstable to stable conditions occurs approximately between 10^6 N/m and 10^7 N/m depending on the size of the contact surface, and that after 10^8 N/m stability is achieved for the majority the cases. And these values were obtained for CZS (contact zone size) of these approximate magnitudes: $S \approx 5 \text{ cm}^2$, $SM \approx 7,5 \text{ cm}^2$, $M \approx 10,5 \text{ cm}^2$, $L \approx 15,5 \text{ cm}^2$.

Now, if we take the range of local contact stiffness ($S = 10^4$ N/m - 10^5 N/m) obtained with the indentation test for an contact area $A = 3.78 \cdot 10^{-6} m^2$. We can estimate the range of contact stiffness K_{inden} values that correspond to the contact surfaces S, SM, M, and L from chapter 4.

$$3.78 \cdot 10^{-6} m^2 \Rightarrow 10^4 - 10^5 \text{ N/m}$$

$$S, SM, M, L \Rightarrow K_{inden}$$

$$\text{For S, } K_{inden} = 1.32 \cdot 10^7 - 1.32 \cdot 10^8 \text{ N/m}$$

$$\text{For SM, } K_{inden} = 1.98 \cdot 10^7 - 1.98 \cdot 10^8 \text{ N/m}$$

$$\text{For M, } K_{inden} = 2.78 \cdot 10^7 - 2.78 \cdot 10^8 \text{ N/m}$$

$$\text{For L, } K_{inden} = 4.11 \cdot 10^7 - 4.11 \cdot 10^8 \text{ N/m}$$

From this we can observe the following: Numerically, we have found a transition zone for contact stiffness between 10^7 and 10^8 N/m, where the implant becomes stable for average size of contact zones as defined by an orthopedic surgeon (chapter 4). The contact stiffness values measured experimentally, translated into an area of the same size as those defined by the surgeon, give values between $1.32 \cdot 10^7$ N/m and $4.11 \cdot 10^8$ N/m. This demonstrates that the range of stiffness values, and the threshold values of stiffness for stability obtained with the implementation of our numerical model, are in the correct order of magnitude; which serves as a partial validation of our model.

6.5.2 Analysis of Young's modulus spatial distribution

The spatial distribution of Young's modulus on the broached surface of the bone showed a high heterogeneity for most samples, with most of the indentation spots displaying Young's modulus values in the range 10^6 - 10^8 N/m, but without a clear pater of compaction.

However, the distribution of sample 362 shows higher levels of Young's modulus concentrated in the central part (section O) in both sides of the sample. Sample 362 also presented the highest magnitudes of Young's modulus as compared to the

other samples, most likely due to the necrotic nature of this sample; this trend was also observed in chapter 5 where we obtained the highest levels of BMD for sample 362.

We compared the spatial distribution of Young's modulus obtained in this chapter with the spatial distribution of BMD obtained in chapter 5 for each sample with the purpose of finding possible correlations.

The patterns obtained for the distribution of BMD and Young's modulus are not coincident, and no correlation is observed. However, sample 362 (figure ??, bottom) presented a somewhat similar pattern for BMD and Young's modulus, with values slightly more correlated as compared to the rest of the samples.

Some possible explanations for this pattern mismatch are:

There is no correlation between the sectors where the BMD was measured in chapter 5, and the indentation spots described in this chapter. An attempt of associating these areas was only done in a visual manner. It is necessary to make a more precise image analysis to be able to correlate properly the regions from the scanned images and the indented zones.

Also, in the indentation test the maximum indentation depth is known but the resulting load-displacement relation is affected by the properties of the material surrounding the indentation spot; in other words, an indentation spot surrounded by mostly trabecular bone will display lower stiffness than an indentation spot that is closer to cortical bone, even if they both are indented at a maximum depth of 0.3 mm. This fact is not taken into account in the evaluation of BMD from the scanned images, since only the trabecular bone is taken into account in the ring of 3 mm, and the effects of the surrounding material are ignored.

CHAPTER 7

Conclusion and Perspectives

With this thesis work we have proposed a method that we called Three-dimensional Resonance Planning (RP3D), which implements numerical modal analysis for the assessment of stability of cementless implants in THR preoperative planning.

The main question that motivated the development of this project was whether or not it was possible to improve the accuracy of THR preoperative planning tools through the introduction of mechanical criteria obtained from a coupling of CT data and a vibration analysis.

In this thesis divided into two main branches, numerical and experimental, first we explored the applicability of numerical modal analysis for two things: the definition of mechanical criteria related to stability from a study of clinical cases, and the implementation of the mechanical criteria for defining stability thresholds with a study of controlled cases. And second, the assessment of the effect of the broaching procedure on the mechanical properties of the bone-implant interface through experimental studies. Thanks to these studies, we were able to:

1. Propose thresholds of contact conditions in terms of area of contact surface and contact stiffness to discriminate stable and unstable implants numerically.
2. Characterize the anchorage properties in the bone-implant interface after the broaching procedure. More specifically, we were able to describe the effect of broaching on the microstructure of the trabecular bone. We observed compaction zones consistent with implant design and we quantified in terms of BMD the local modification of the trabecular bone due to broaching.
3. Characterize the apparent stiffness of the bone surface originated by the broaching. This stiffness was in the order of $10^4 - 10^5$ N/m, for an indenter apparent area of about $3.78 \cdot 10^{-6} m^2$. Moreover, we were able to find an agreement between the contact stiffness in the bone-implant interface measured experimentally and the contact stiffness threshold for stability obtained numerically, which serves to partially validate the principles of our proposed method (RP3D).

From the biomechanics point of view, this finding suggests that a numerical analysis of stability based on vibration methods has potential to discriminate between stable and unstable implants.

Certain limitations come from the fact that for the numerical study only a small cohort of patients was considered for determining the discrimination parameters.

Moreover, the controlled study considered only four different sizes of contact zone and only one type of prosthesis, though for the different contact sizes considered no major changes were observed and most of the variations in stability were defined by the values of apparent contact stiffness.

Likewise, in the experimental study to assess the effect of the broaching, only four samples were considered. In addition, issues related to a possible inconsistency between the definition of the region of interest in the imaging analysis and the indented area in the mechanical test prevented us to establish a relation between the parameters measured in each study.

For the determination of interface stiffness for a given subject from CT data, a conversion law between Hounsfield units and stiffness is necessary. Such a law could not be obtained.

With further development it is expected to find correlations between the bone properties contained in μ CT-Scan images (described in chapter 5) and the mechanical properties of the bone measured experimentally in chapter 6. This would allow to run the numerical analysis during the preoperative planning with the actual mechanical properties of the bone of the patient obtained merely from a CT-Scan.

From the orthopedic point of view, our results could have an important impact in the conception of preoperative planning moving forward, highlighting the advantages of re-engineering the existing preoperative planning tools, specifically, the introduction of a finite element analysis component, that provides the surgeon with mechanical criteria obtained from the vibrational analysis to enhance the accuracy of the planning.

APPENDIX A

Appendix: Modal shapes, clinical study

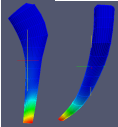
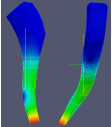
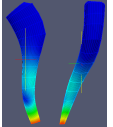
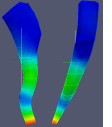
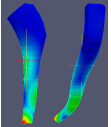
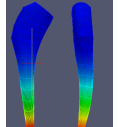
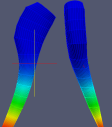
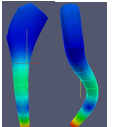
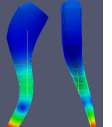
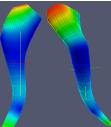
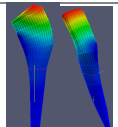
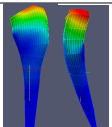
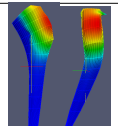
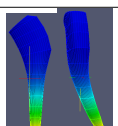
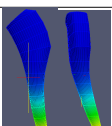
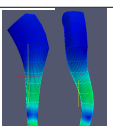
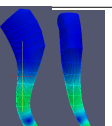
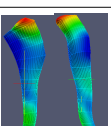
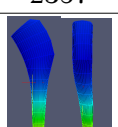
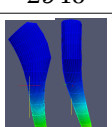
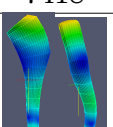
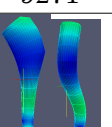
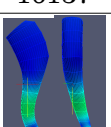
	Nb Modes	Eigen modes					Hz
		1	2	3	4	5	
A	5	8110 	10525 	11189 	16213 	17918 	Hz
B	7	2309 	2830 	8326 	10312 	10813 	Hz
C	2	9591 	17693 	X	X	X	Hz
D	1	19828 	X	X	X	X	Hz
E	7	2371 	2910 	8504 	10538 	16429 	Hz
F	9	2357 	2940 	7418 	9271 	16137 	Hz

Figure A.1: Modal shapes of the first five modes of the six patients of the clinical study, as well as number of modes and modal frequencies in the frequency range [0 : 20] kHz.

Figure A.1 shows a summary of the results of the modal analysis of clinical cases presented in Chapter 3 for all the six subjects. A, B, C were identified by the surgeon as stable cases, D as stable with presence of pain, and E, and F as unstable. Number of modes and frequency values does not discriminate between stable and

unstable cases. Proximal motion was observed in higher modes of all the unstable cases, in the stable cases was not always present.

APPENDIX B

Appendix: Modal analysis, controlled study

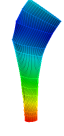
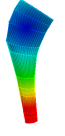
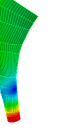
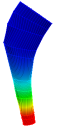
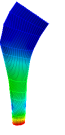
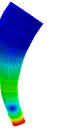
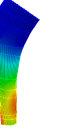
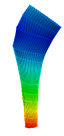
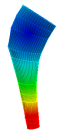
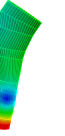
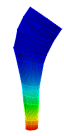
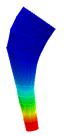
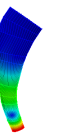
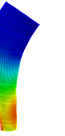
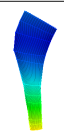
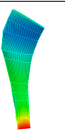
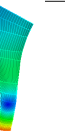
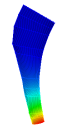
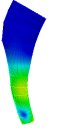
CZS	Stiffness (k)	# modes	Modal Shapes and Frequencies [0-20kHz]				
			1	2	3	4	5
Small	1×10^5	5/11	1.1357	1.8516	5.0712	5.7779	5.9419
							
Small	1×10^{10}	5/5	2.9849	3.8571	10.9030	13.4635	19.2059
							
Medium	1×10^5	5/11	1.6085	2.2129	5.9438	6.5614	6.8127
							
Medium	1×10^{10}	5/5	3.2876	4.0564	12.3721	14.6927	19.926
							
Large	1×10^5	5/11	2.2922	2.8670	7.2288	7.6107	8.2253
							
Large	1×10^{10}	3/3	9.83261	13.9428	17.0514		
							

Figure B.1: Modal shapes and modal frequencies of the first five modes of for Small, Medium and Large CZS and two values of apparent stiffness (N/m) in the frequency range [0 : 20] kHz.

Figure B.1 shows a summary of the results of the modal analysis of controlled cases presented in Chapter 4 for three different sizes on contact zone (CZS) and two values of apparent stiffness for each CZS. It can be observed how for all the CZS for a lower stiffness value there is presence of proximal bending in the modal shapes,

and for the higher values of stiffness the proximal bending disappears. It can also be noticed that the proximal bending is lower for higher CZS.

APPENDIX C

Appendix: Broaching BMD spatial distribution, μ CT-Scan images

Figures C.1, C.2, and C.3 show the BMD (g/cm^3) variation of samples 269, 283, and 331, produced by the broaching effect, and measured from μ CT-Scan images. Similarly to the results presented in Chapter 5 for the sample 362, it can be noticed how the variations of BMD mostly occur in the farthest lateral zones between $300^\circ - 0^\circ$, and around 180° . It can also be observed that the variations are higher at the distal longitudinal zones (L1-L2), except for sample 283, where the distribution is more or less equally distributed along the five zones.

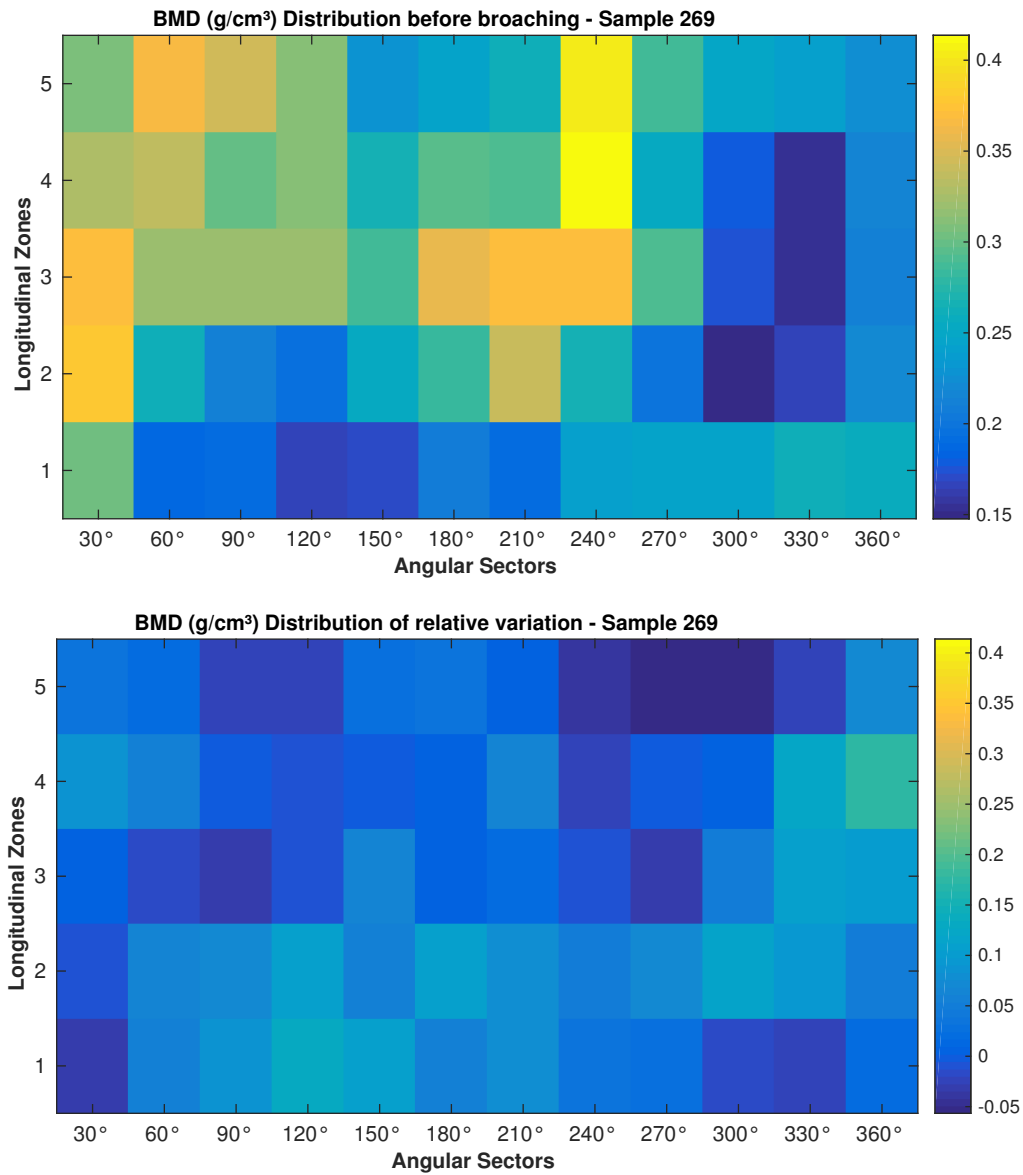


Figure C.1: BMD Distribution before broaching (top) and relative variation after-broaching (bottom) - normalized for sample 269

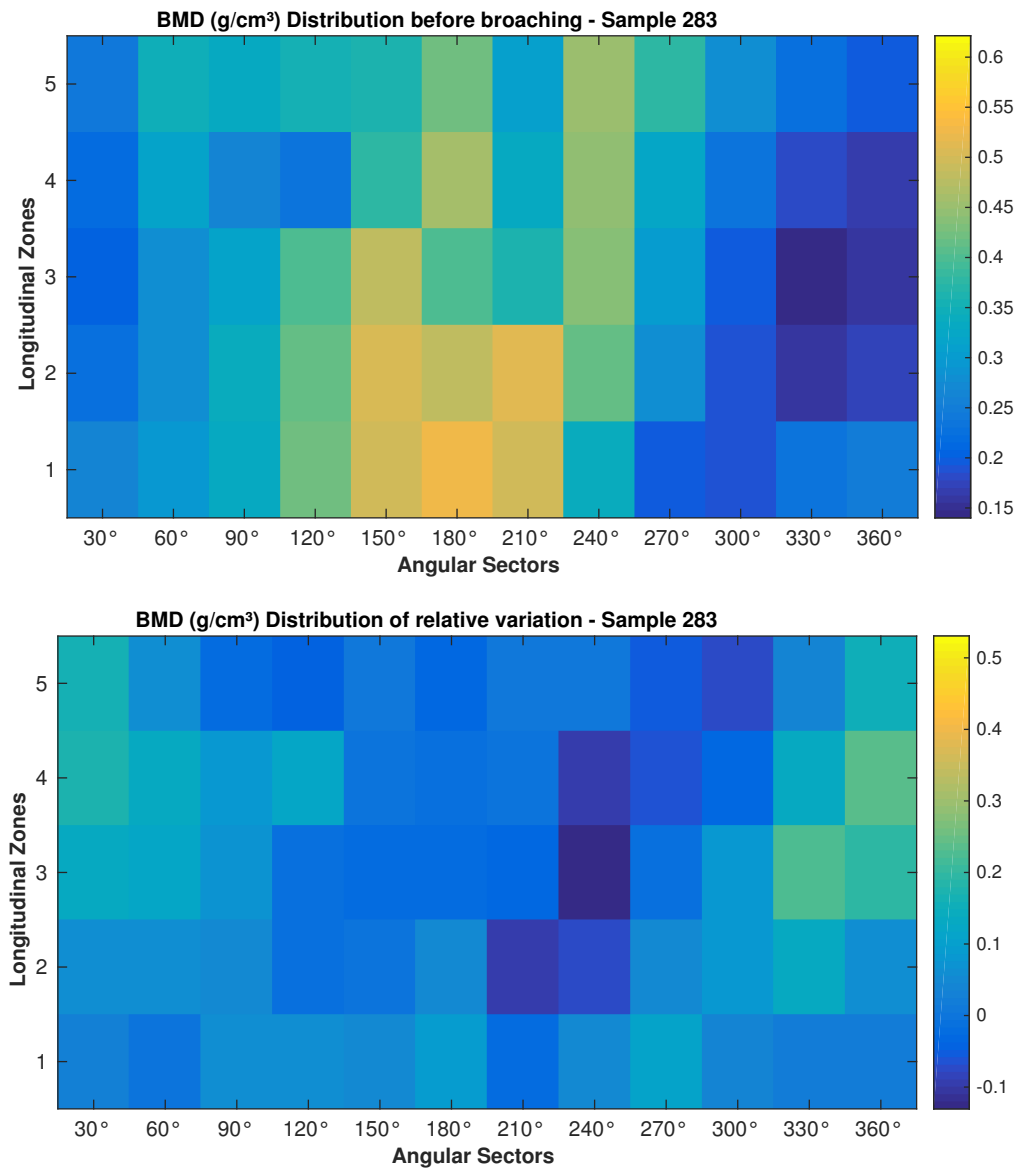


Figure C.2: BMD Distribution before broaching (top) and relative variation after-broaching (bottom) - normalized for sample 283

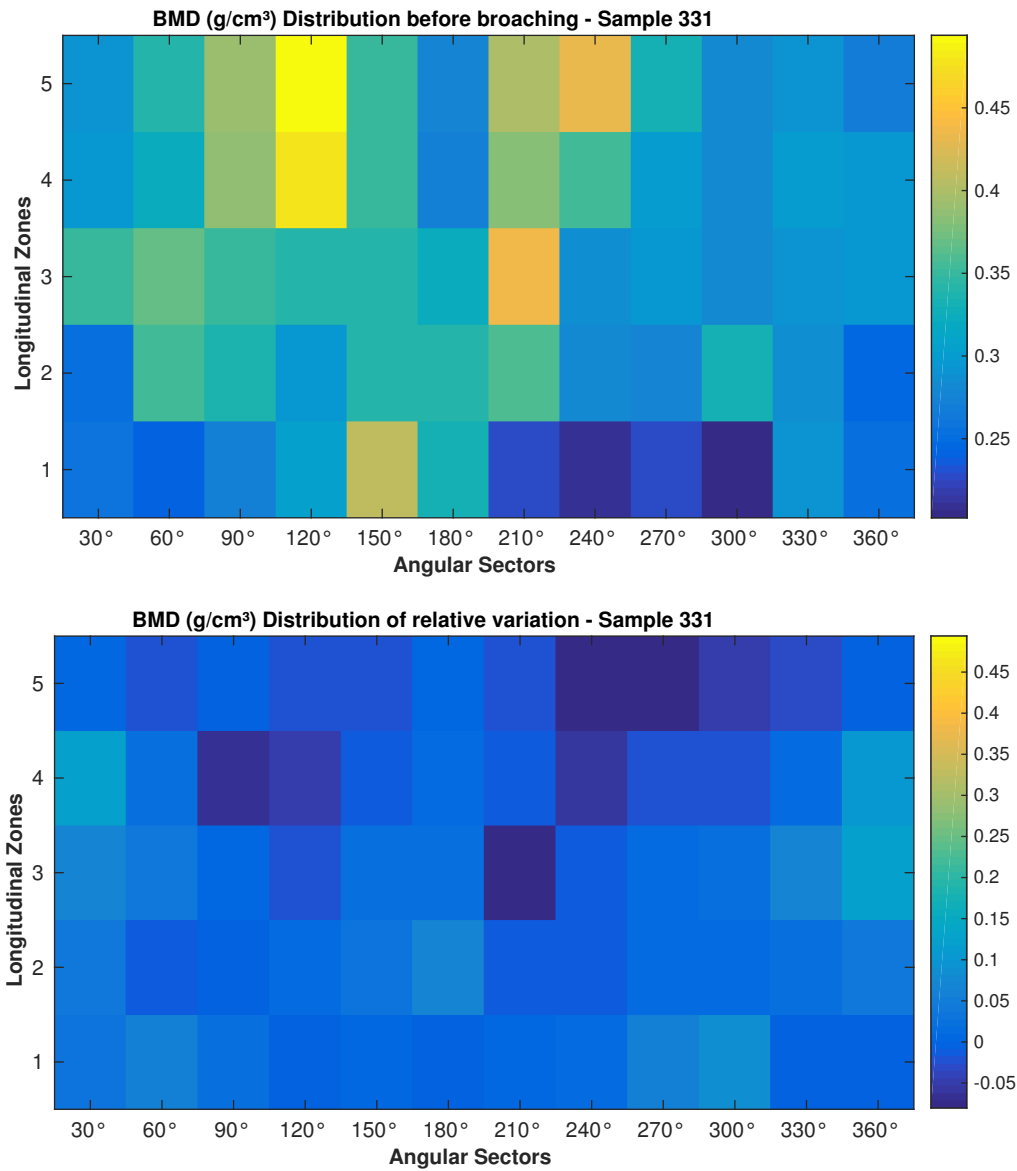


Figure C.3: BMD Distribution before broaching (top) and relative variation after-before broaching (bottom)- normalized for sample 331

APPENDIX D

Appendix: Broaching BMD angular variation, μ CT-Scan images

In this appendix we show angular relative variations (% BMD) and angular values of BMD (g/cm^3) before and after broaching obtained from μ CT-Scan images for sample 269 (Figures D.1 and D.2), sample 283 (Figures D.3 and D.4), sample 331 (Figures D.5 and D.6), and sample 362 (Figures D.7 and D.8). As presented and discussed in Chapter 5, it can be observed that the highest variations of BMD are obtained in the distal zones (L1-L2), in almost all the cases the positive variations were more significant than the negative variations due to the broaching, except for zone L5 of samples 331, and 269. Also, most of the concentration of BMD after broaching is obtained between $300^\circ - 0^\circ$ and around 180° .

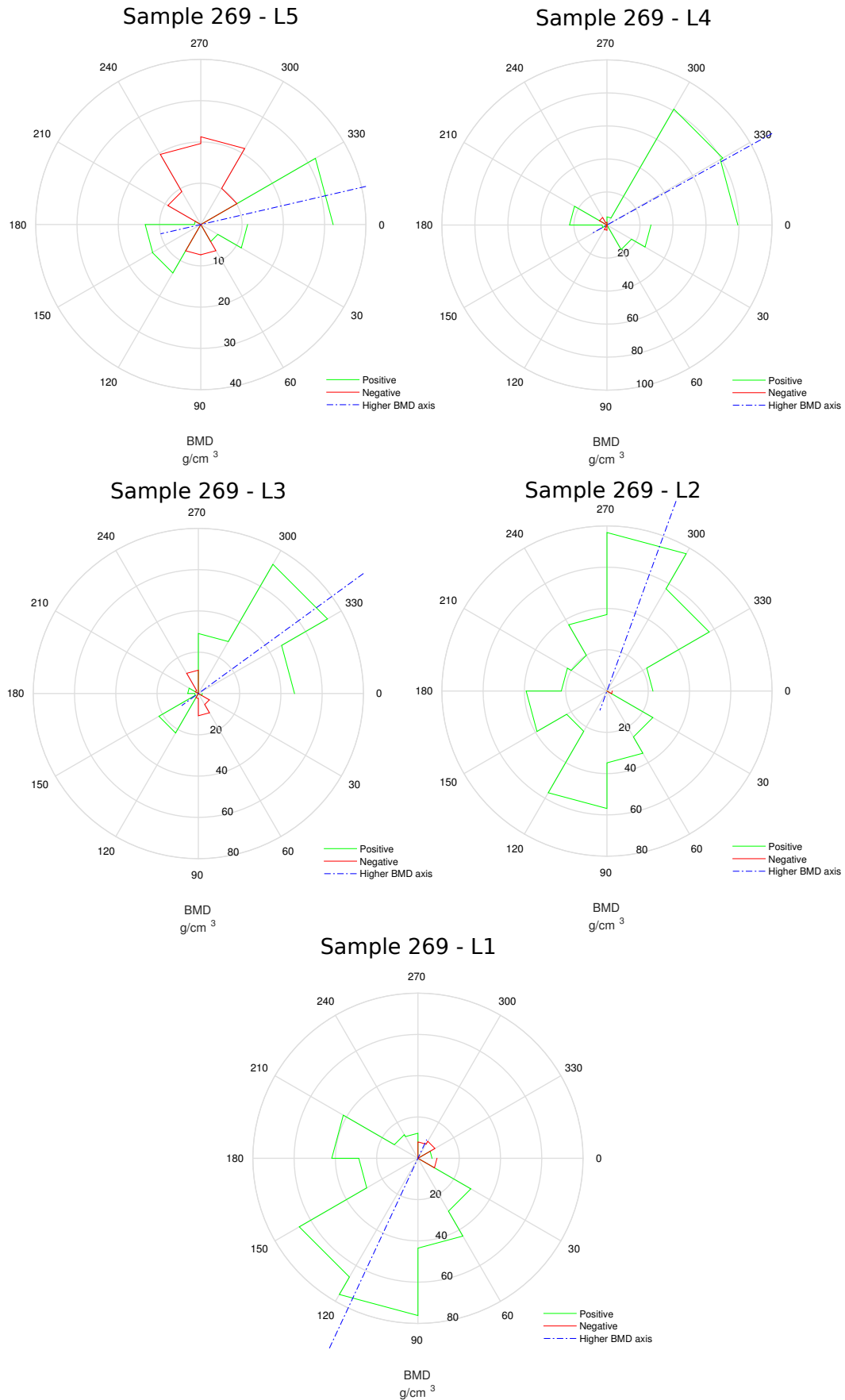


Figure D.1: % BMD angular relative variation for zones L1 - L5, sample 269.

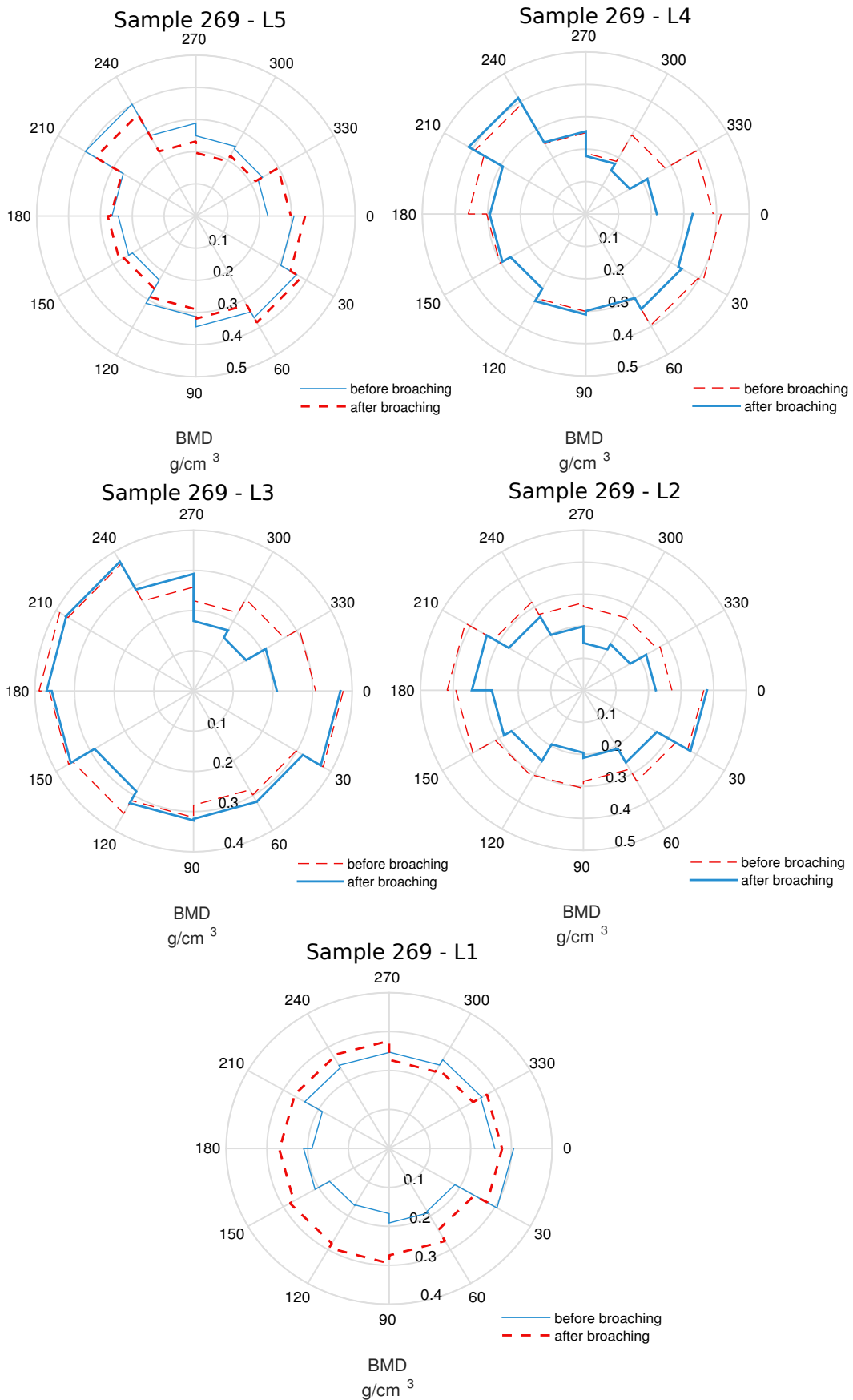


Figure D.2: BMD (g/cm^3) angular distribution before and after broaching for zones L1 - L5, sample 269.

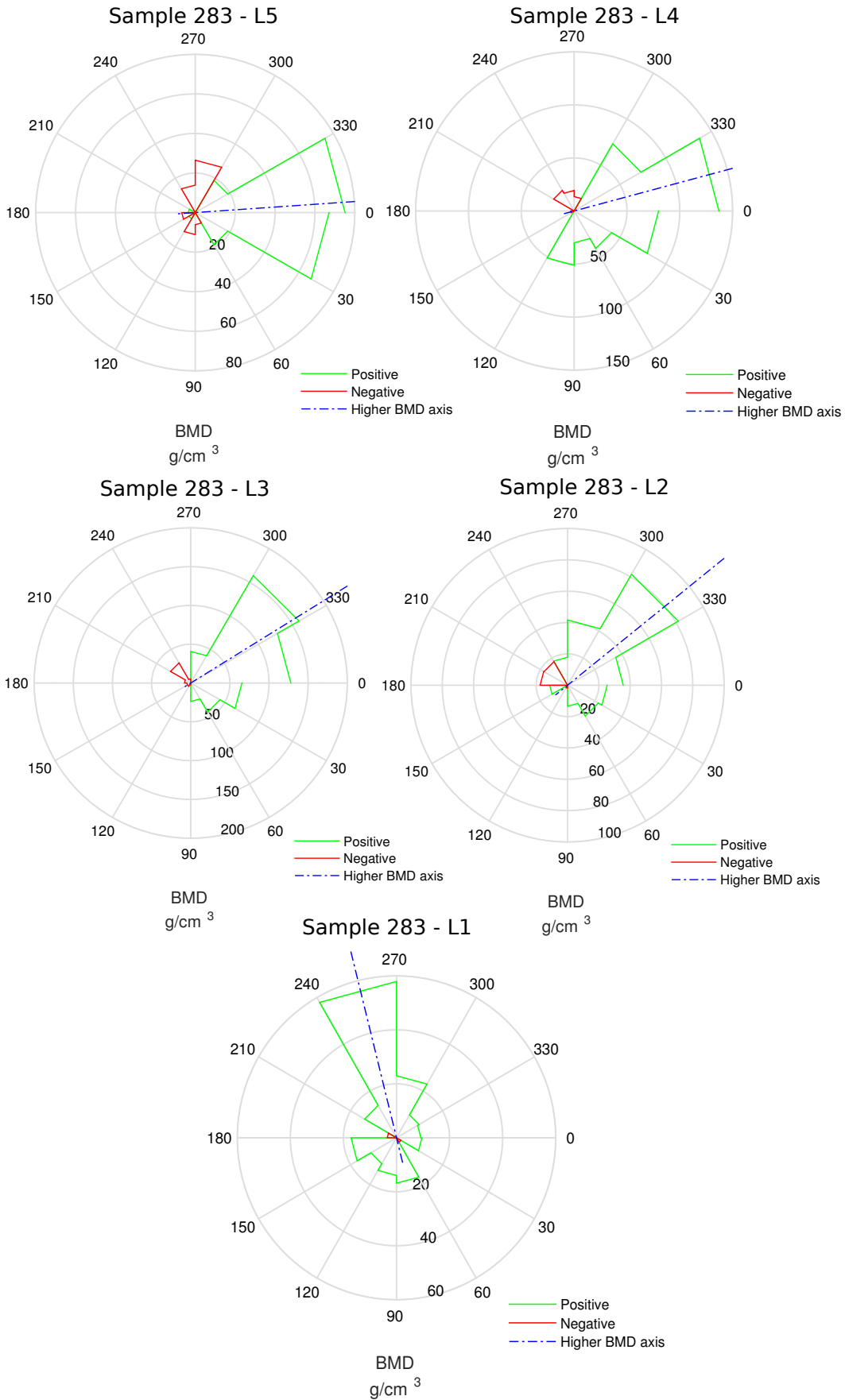


Figure D.3: % BMD angular relative variation for zones L1 - L5, sample 283.

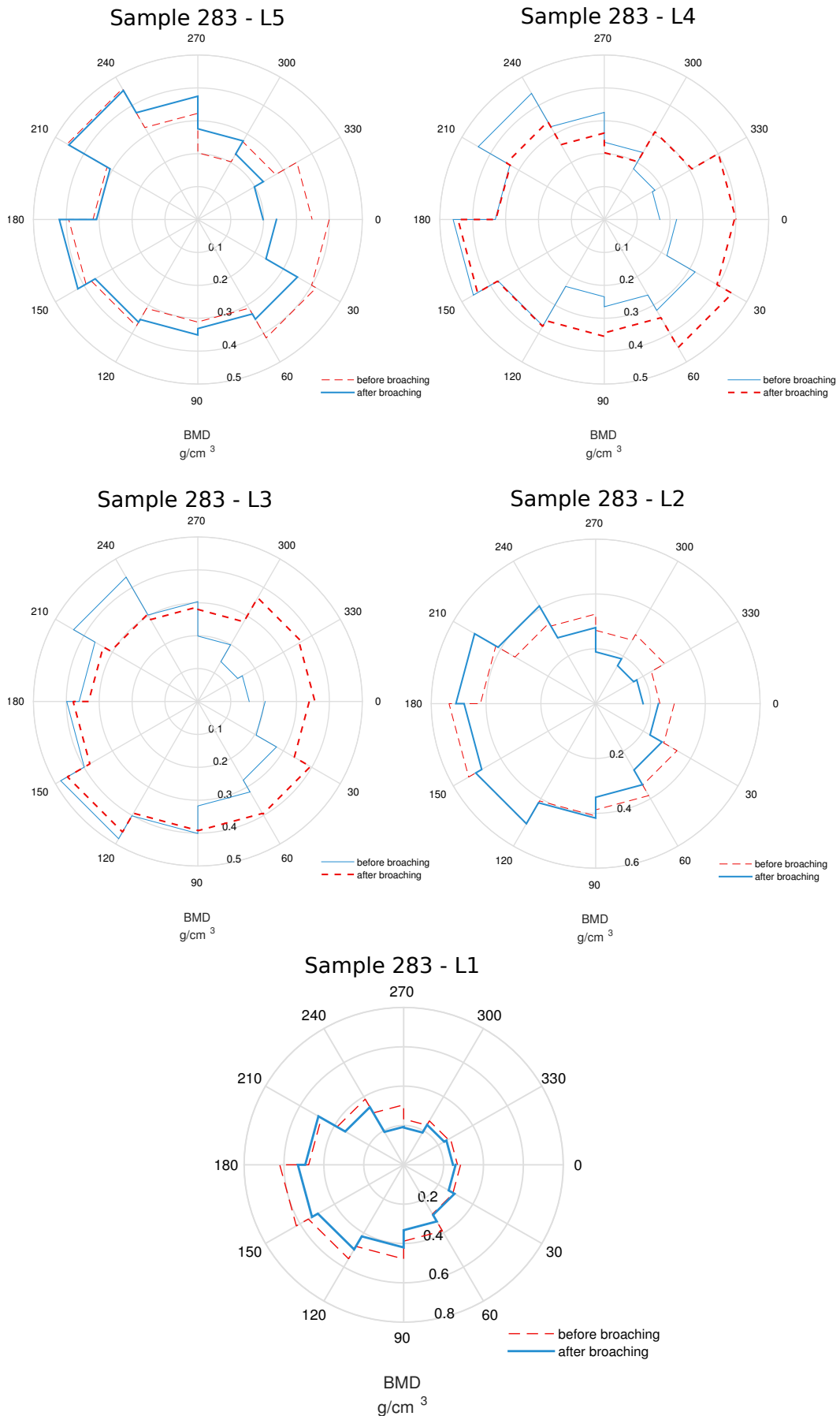


Figure D.4: BMD (g/cm^3) angular distribution before and after broaching for zones L1 - L5, sample 283.

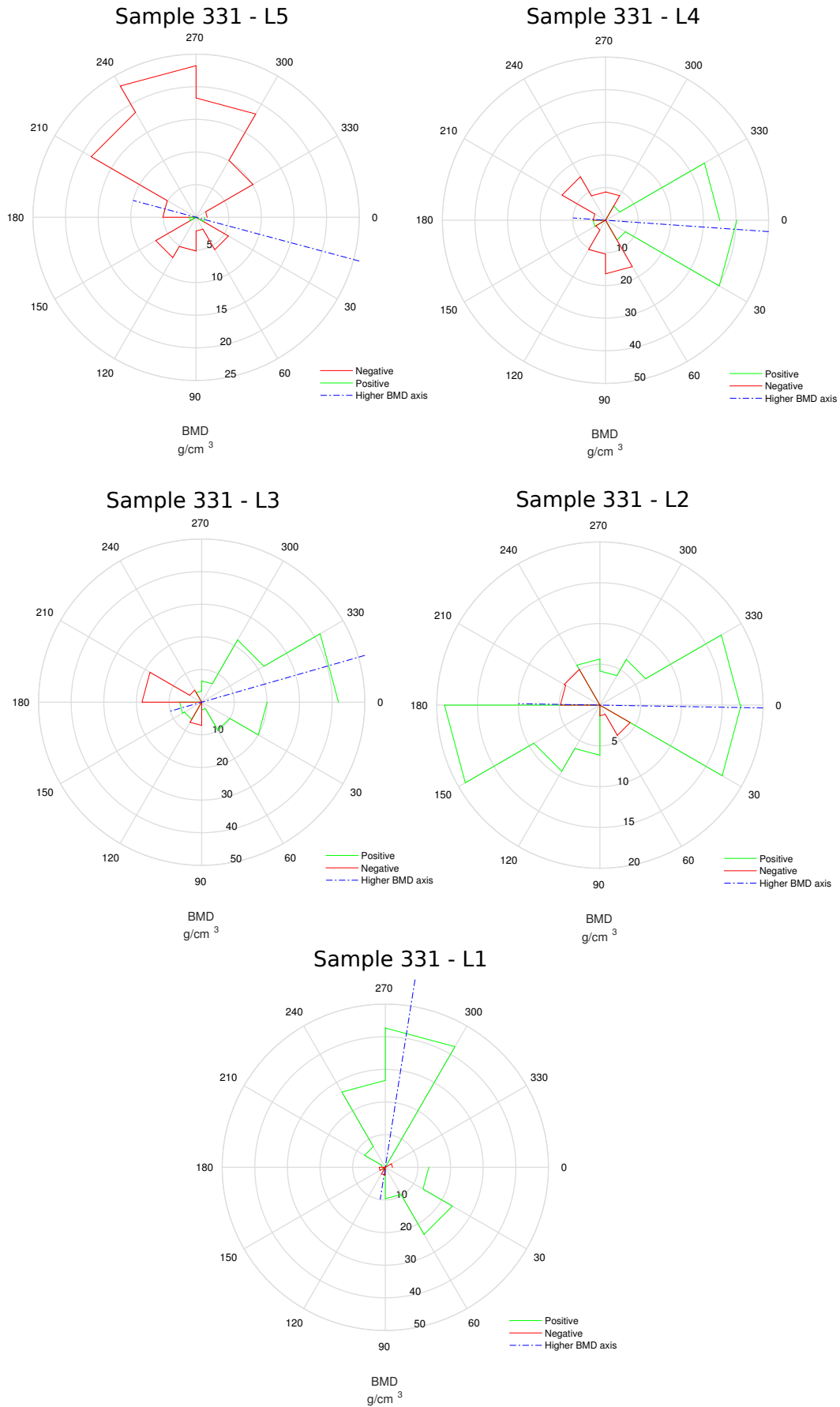


Figure D.5: % BMD angular relative variation for zones L1 - L5, sample 331.

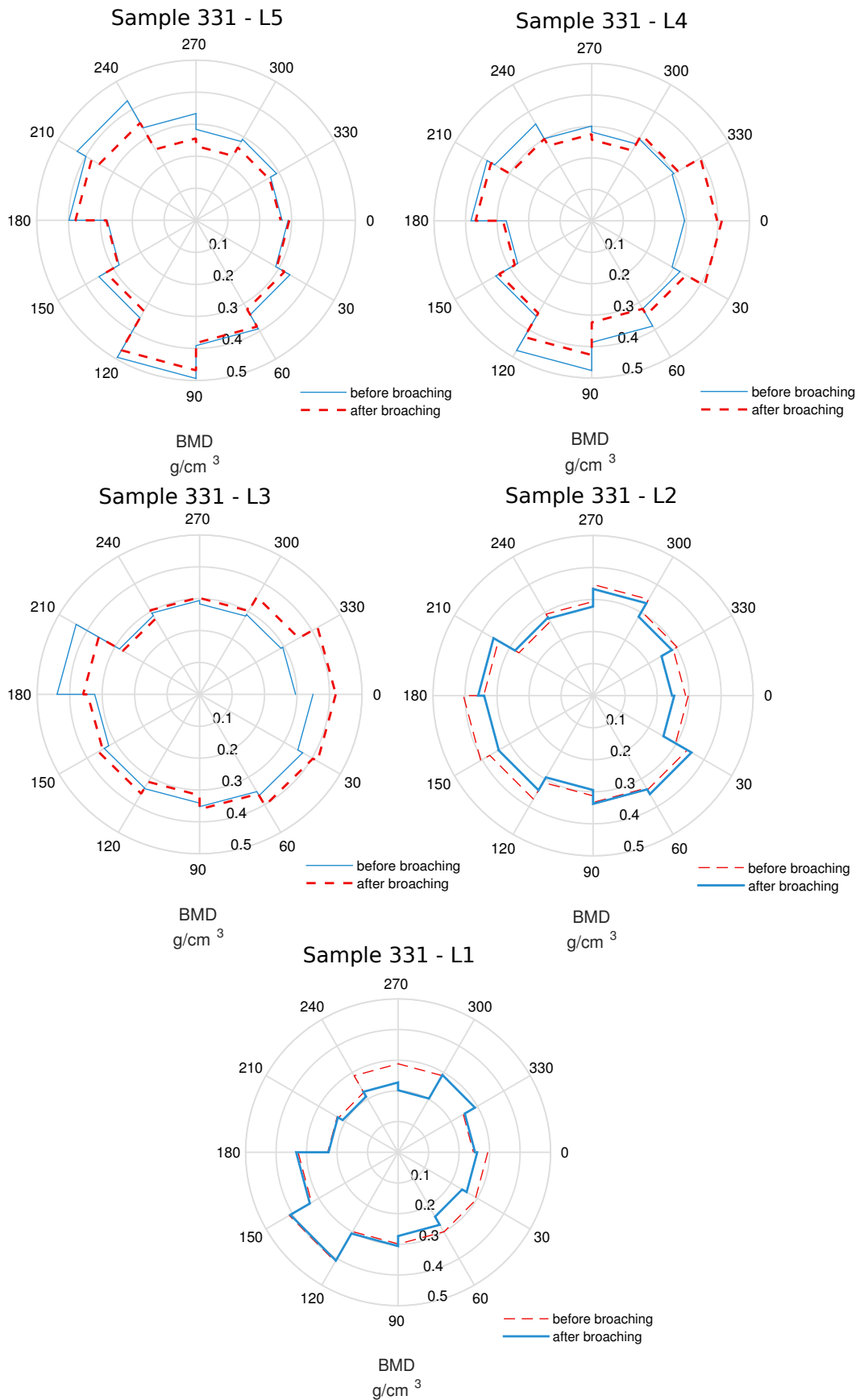


Figure D.6: BMD (g/cm^3) angular distribution before and after broaching for zones L1 - L5, sample 331.

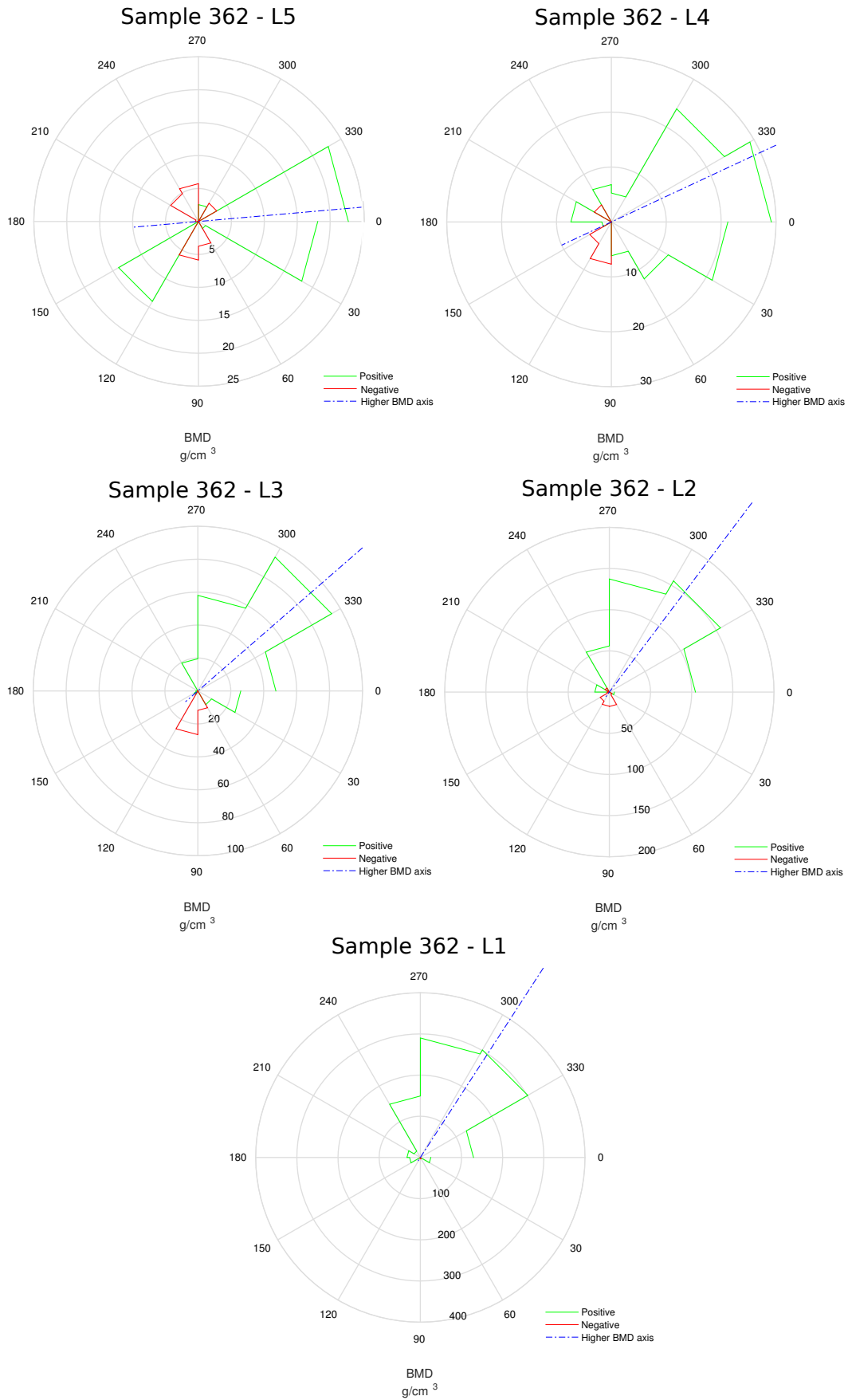


Figure D.7: % BMD angular relative variation for zones L1 - L5, sample 362.

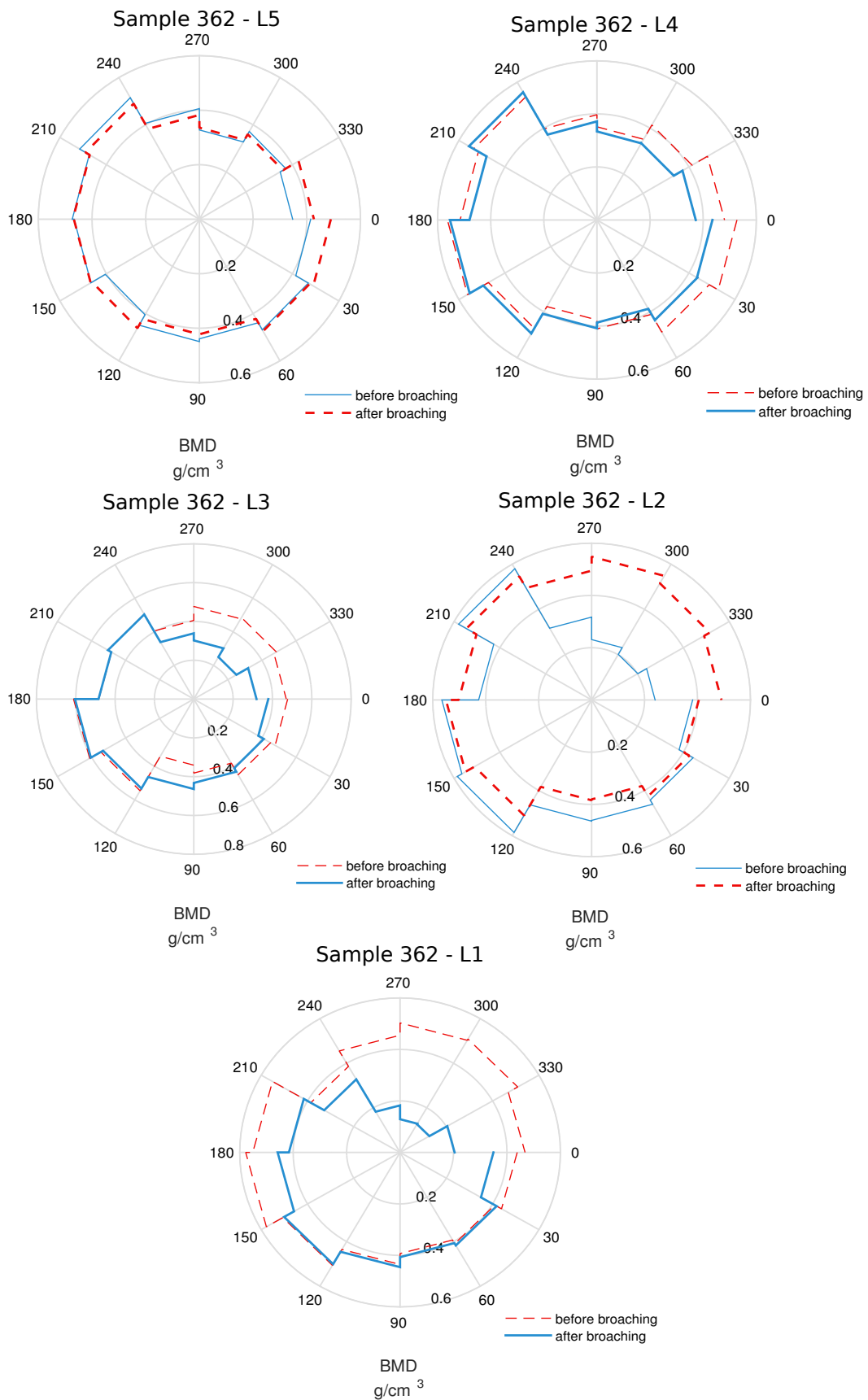


Figure D.8: BMD (g/cm^3) angular distribution before and after broaching for zones L1 - L5, sample 362.

APPENDIX E

Appendix: Results of indentation orthogonality test

Figure E.1 shows how for different angular deviations from the orthogonal axis of indentation, the maximum load is highly affected (Top). However, the stiffness, calculated as the slope of the upper part of the unload curve, is almost the same for the different angular deviations (bottom) that we tested. One explanation for this could be that the variation of the angle only has an effect on the load-displacement relation until reaching a point of fully charged penetration . In our test the maximum penetration that allowed us to reach that point was 0.3 mm.

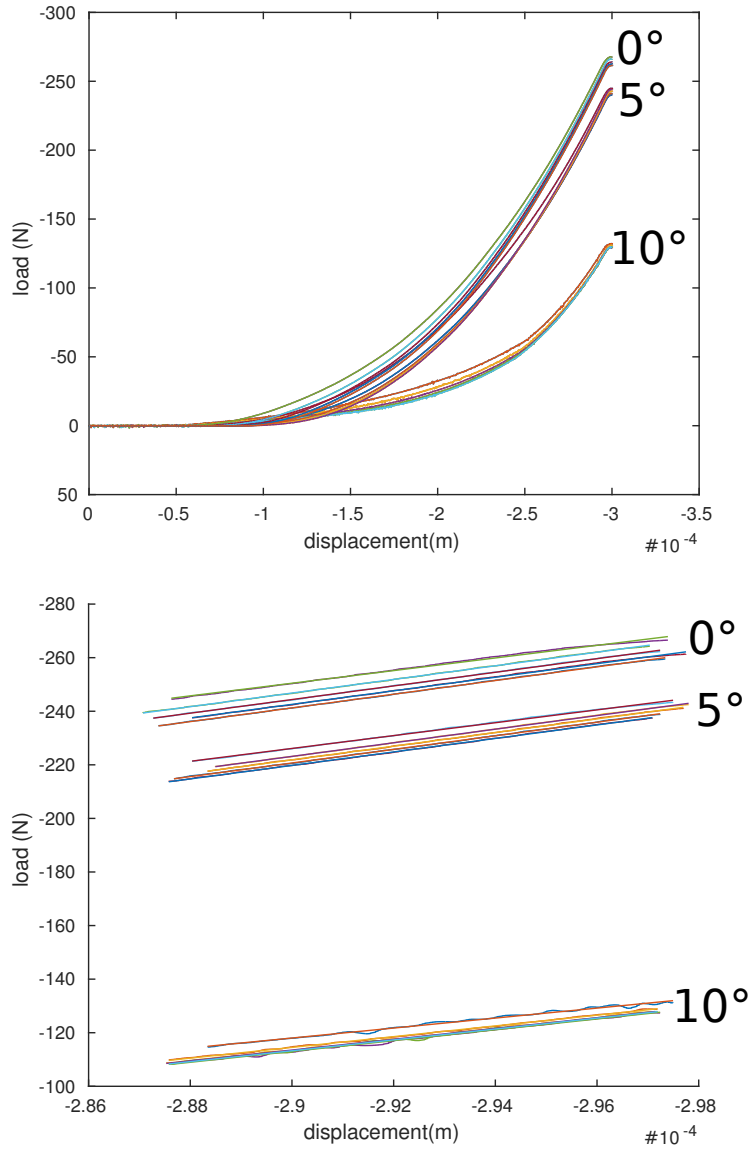


Figure E.1: Top: Load Vs Displacement curve, unload stage, of the indentation test with polycarbonate used for measuring effects of orthogonality; curves for deviation angles of 0° (perpendicular), 5°, and 10° are displayed. Bottom: Upper part of the slope of the curves in the Top figure, also for deviation angles of 0° (perpendicular), 5°, and 10° are displayed

Bibliography

- A. Aamodt, K. A. Kvistad, E. Andersen, J. Lund-Larsen, J. Eine, P. Benum, and O. S. Husby. Determination of hounsfield value for ct-based design of custom femoral stems. *J Bone Joint Surg Br*, 81(1):143–147, 1999.
- T. Albrektsson and B. Albrektsson. Osseointegration of bone implants. a review of an alternative mode of fixation. *Acta Orthop Scand*, 58(5):567–577, 1987.
- R. J. Allemang. The modal assurance criterion ? twenty years of use and abuse. *Based on a paper presented at IMAC-XX, the 20th International Modal Analysis Conference, Los Angeles, CA, February 2002*, 2003.
- Y. H. An and R. A. Draughn. *Mechanical Testing of Bone and the Bone-Implant Interface*. CRC Press, 1999. ISBN 978-1-4200-7356-0. Google-Books-ID: kEX8oi3IrBgC.
- M. Aublin. *Systèmes mécaniques: théorie et dimensionnement*. Dunod, 1992. ISBN 978-2-10-001051-6. Google-Books-ID: R48tOgAACAAJ.
- A. Auperrin. *Caractérisation tissulaire pour la détermination du comportement de l'os crânien : essais mécaniques et imagerie médicale*. PhD thesis, Université de Valenciennes et du Hainaut Cambrésis, 2009.
- P. L. BEGUEC, F. Canovas, O. Roche, M. Goldschild, and J. Batard. *Uncemented Femoral Stems for Revision Surgery: The Press-fit Concept - Planning - Surgical Technique - Evaluation*. Springer, 2015. ISBN 978-3-319-03614-4. Google-Books-ID: PNkRBwAAQBAJ.
- C. R. Bragdon, D. Burke, J. D. Lowenstein, D. O. O'Connor, B. Ramamurti, M. Jasty, and W. H. Harris. Differences in stiffness of the interface between a cementless porous implant and cancellous bone in vivo in dogs due to varying amounts of implant motion. *J Arthroplasty*, 11(8):945–951, 1996. micromotion 150.
- Bruker. Automated trabecular and cortical bone selection. Technical report, Bruker microCT, 2015.
- D. P. Byrne, K. J. Mulhall, and J. F. Baker. Anatomy & biomechanics of the hip. 4(1), 2010.
- L. W. Carter, D. O. Stovall, and T. R. Young. Determination of accuracy of pre-operative templating of noncemented femoral prostheses. *J Arthroplasty*, 10(4): 507–513, 1995. surgeon experience in preop planning.

- C. Geuzaine and J.-F. Remacle. Gmsh: a three-dimensional finite element mesh generator with built-in pre- and post-processing facilities. *International Journal For Numerical Methods In Engineering*, 2009.
- A. González Della Valle, F. Comba, N. Taveras, and E. A. Salvati. The utility and precision of analogue and digital preoperative planning for total hip arthroplasty. *Int Orthop*, 32(3):289–294, 2008. little accuracy of 2d planning.
- M. Granke, Q. Grimal, A. Sañed, P. Nauleau, F. Peyrin, and P. Laugier. Change in porosity is the major determinant of the variation of cortical bone elasticity at the millimeter scale in aged women. 49(5):1020–1026, 2011. ISSN 1873-2763.
- B. Helgason, E. Perilli, E. Schileo, F. Taddei, S. Brynjólfsson, and M. Viceconti. Mathematical relationships between bone density and mechanical properties: a literature review. *Clin Biomech (Bristol, Avon)*, 23(2):135–146, 2008.
- U. Holzwarth and G. Cotogno. Total hip arthroplasty, state of the art, challenges and prospects. *Publications Office of the European Union*, 2012.
- T. Karachalios. *Bone-Implant Interface in Orthopedic Surgery*. Springer, 2014.
- T. S. Keller. Predicting the compressive mechanical behavior of bone. 27(9):1159–1168, 1994. ISSN 0021-9290.
- J. L. Knight and R. D. Atwater. Preoperative planning for total hip arthroplasty. quantitating its utility and precision. *J Arthroplasty*, 7 Suppl:403–409, 1992. low accuracy 2D planning.
- I. D. Learmonth, C. Young, and C. Rorabeck. The operation of the century: total hip replacement. 370(9597):1508–1519, 2007. ISSN 0140-6736, 1474-547X.
- R. Martin and N. Sharkey. Mechanical effects of postmortem changes, preservation and allograft bone treatments. In *Bone Mechanics Handbook, Second Edition*, pages 20–1–20–24. CRC Press, 2001. ISBN 978-0-8493-9117-0.
- D. Mitton, C. Roux, and P. Laugier. Bone overview. In *Bone Quantitative Ultrasound*, chapter 1, pages 1–28. Springer, 2011.
- M. Nordin and V. H. Frankel. *Basic Biomechanics of the Musculoskeletal System*. Lippincott Williams & Wilkins, 2001. ISBN 978-0-683-30247-9. Google-Books-ID: UCxsf7mMBE0C.
- W. C. Oliver and G. M. Pharr. Measurement of hardness and elastic modulus by instrumented indentation: Advances in understanding and refinements to methodology. 19(1):3–20, 2004. ISSN 2044-5326, 0884-2914.

- I. Otomaru, M. Nakamoto, Y. Kagiya, M. Takao, N. Sugano, N. Tomiyama, Y. Tada, and Y. Sato. Automated preoperative planning of femoral stem in total hip arthroplasty from 3d CT data: Atlas-based approach and comparative study. *16(2):415–426*, 2012. ISSN 1361-8415.
- L. C. Pastrav, J. Devos, G. Van der Perre, and S. V. N. Jaecques. A finite element analysis of the vibrational behaviour of the intra-operatively manufactured prosthesis-femur system. *Med Eng Phys*, 31(4):489–494, 2009a.
- L. C. Pastrav, S. V. Jaecques, I. Jonkers, G. V. d. Perre, and M. Mulier. In vivo evaluation of a vibration analysis technique for the per-operative monitoring of the fixation of hip prostheses. *J Orthop Surg Res*, 4:10, 2009b.
- M. A. Perez and B. Seral-Garcia. A finite element analysis of the vibration behaviour of a cementless hip system. *Comput Methods Biomech Biomed Engin*, 16(9):1022–1031, 2013.
- R. Puers, M. Catrysse, G. Vandevoorde, R. Collier, E. Louridas, F. Burny, M. Donkerwolcke, and F. Moulart. A telemetry system for the detection of hip prosthesis loosening by vibration analysis. *Sensors and Actuators*, 85:42–47, 2000.
- G. Qi, W. P. Mouchon, and T. E. Tan. How much can a vibrational diagnostic tool reveal in total hip arthroplasty loosening? *Clin Biomech (Bristol, Avon)*, 18(5):444–458, 2003.
- B. S. Ramamurti, T. E. Orr, C. R. Bragdon, J. D. Lowenstein, M. Jasty, and W. H. Harris. Factors influencing stability at the interface between a porous surface and cancellous bone: a finite element analysis of a canine in vivo micromotion experiment. *J Biomed Mater Res*, 36(2):274–280, 1997.
- B. Reggiani, L. Cristofolini, E. Varini, and M. Viceconti. Predicting the subject-specific primary stability of cementless implants during pre-operative planning: preliminary validation of subject-specific finite-element models. *J Biomech*, 40(11):2552–2558, 2007.
- B. Reggiani, L. Cristofolini, F. Taddei, and M. Viceconti. Sensitivity of the primary stability of a cementless hip stem to its position and orientation. *Artif Organs*, 32(7):555–560, 2008. primary stability vs position and orientation of stem.
- J.-Y. Rho, L. Kuhn-Spearing, and P. Zioupos. Mechanical properties and the hierarchical structure of bone. *20(2):92–102*, 1998. ISSN 1350-4533.
- E. Sariali, A. Mouttet, G. Pasquier, and E. Durante. Three-dimensional hip anatomy in osteoarthritis: Analysis of the femoral offset. *24(6):990–997*, 2009a. ISSN 0883-5403.

- E. Sariali, A. Mouttet, G. Pasquier, E. Durante, and Y. Catone. Accuracy of reconstruction of the hip using computerised three-dimensional pre-operative planning and a cementless modular neck. *J Bone Joint Surg Br*, 91(3):333–340, 2009b.
- E. Sariali, R. Mauprivez, F. Khiami, H. Pascal-Mousselard, and Y. Catonné. Accuracy of the preoperative planning for cementless total hip arthroplasty. a randomised comparison between three-dimensional computerised planning and conventional templating. *Orthop Traumatol Surg Res*, 98(2):151–158, 2012a.
- E. Sariali, A. Mouttet, P. Mordasini, and Y. Catonné. High 10-year survival rate with an anatomic cementless stem (sps). *Clin Orthop Relat Res*, 470(7):1941–1949, 2012b.
- E. Sariali, Y. Catonne, and H. Pascal-Moussellard. Three-dimensional planning-guided total hip arthroplasty through a minimally invasive direct anterior approach. clinical outcomes at five years' follow-up. *Int Orthop*, 2016.
- T. Shapurian, P. D. Damoulis, G. M. Reiser, T. J. Griffin, and W. M. Rand. Quantitative evaluation of bone density using the hounsfield index. 21(2):290–297, 2006. ISSN 0882-2786.
- D. R. Sumner, T. L. Willke, A. Berzins, and T. M. Turner. Distribution of young's modulus in the cancellous bone of the proximal canine tibia. 27(8):1095–1099, 1994. ISSN 0021-9290.
- K. Søballe. Hydroxyapatite ceramic coating for bone implant fixation. mechanical and histological studies in dogs. *Acta Orthop Scand Suppl*, 255:1–58, 1993.
- K. Søballe, E. S. Hansen, H. B-Rasmussen, P. H. Jørgensen, and C. Bünger. Tissue ingrowth into titanium and hydroxyapatite-coated implants during stable and unstable mechanical conditions. *J Orthop Res*, 10(2):285–299, 1992.
- S. Tang, P. J. Parsons, and W. Slavin. Rapid and reliable method for the determination of aluminium in bone by electrothermal atomic absorption spectrometry. 121(2):195–200, 1996. ISSN 0003-2654.
- S. Timoshenko. *Theory of Elasticity*. Mcgraw-Hill College, 3 edition edition, 1970. ISBN 978-0-07-064720-6.
- C. Turner and D. Burr. Experimental techniques for bone mechanics. In *Bone Mechanics Handbook, Second Edition*, pages 7–1–7–35. CRC Press, 2001. ISBN 978-0-8493-9117-0.
- Q. Vallet. Analyse par une méthode vibratoire de la stabilité d'une prothèse de hanche : modélisation numérique et validation expérimentale in vitro et in vivo. Master's thesis, Université Pierre et Marie Curie., 2013.

- E. Varini, E. Bialoblocka-Juszczak, M. Lannocca, A. Cappello, and L. Cristofolini. Assessment of implant stability of cementless hip prostheses through the frequency response function of the stem?bone system. *Sensors and Actuators A: Physical*, A163:526–532, 2010.
- M. Viceconti, R. Lattanzi, B. Antonietti, S. Paderni, R. Olmi, A. Sudanese, and A. Toni. CT-based surgical planning software improves the accuracy of total hip replacement preoperative planning. 25(5):371–377, 2003a. ISSN 1350-4533.
- M. Viceconti, D. Testi, M. Simeoni, and C. Zannoni. An automated method to position prosthetic components within multiple anatomical spaces. 70(2):121–127, 2003b. ISSN 0169-2607.
- M. Viceconti, G. Brusi, A. Pancanti, and L. Cristofolini. Primary stability of an anatomical cementless hip stem: a statistical analysis. *J Biomech*, 39(7):1169–1179, 2006. osseointegration, 150 microns.
- D. C. Wirtz, N. Schiffers, T. Pandorf, K. Radermacher, D. Weichert, and R. Forst. Critical evaluation of known bone material properties to realize anisotropic FE-simulation of the proximal femur. 33(10):1325–1330, 2000. ISSN 0021-9290.

List of publications and communications

Papers

- A. Rondon, Q. Vallet, E. Sariali, Q. Grimal, "Modal analysis for the assessment of cementless hip stem primary stability in preoperative THA planning", *Submitted for publication in journal: Medical Engineering & Physics*.
- A. Rondon, S. Pinto, E. Sariali, Q. Grimal, *in edition: "* μ CT-based characterization of the broaching effect on the bone-implant interface in total hip arthroplasty."

Conferences

- A. Rondon, E. Sariali, Q. Grimal, "Finite Element Vibrational Analysis In THA Preoperative Planning", *EORS 2016 - European Orthopaedic Research Society, Annual Meeting*, Bologna, Italy, Septembre 2016, **Poster presentation**.
- A. Rondon, E. Sariali, Q. Grimal, "VIBRATIONAL NUMERICAL ANALYSIS OF A HIP IMPLANT TO ACCOUNT FOR CONTACT PROPERTIES IN SURGICAL PLANNING", *Congress of the European Society of Biomechanics*, Lyon, France, July 2016, **Poster presentation**.
- A. Rondon, Q. Vallet, E. Sariali, Q. Grimal, "Stability of a Cementless Hip Implant: Numerical Analysis of the Vibrational Behavior.", *International Mechanical Engineering Congress and Exposition (IMECE), American Society of Mechanical Engineers (ASME)*, Montreal, Canada, November 2014, **Oral presentation**.
- Q. Vallet, A. Rondon, E. Sariali, Q. Grimal, "Numerical Modeling of Hip Implant Vibrational Behavior for the Analysis of Stability", *World Congress on Computational Mechanics (WCCM XI - ECCM V - ECFD VI)*, Barcelona, Spain, July 2014, **Oral presentation**.
- A. Rondon, E. Sariali, Q. Vallet, Q. Grimal, "Prediction Of The Primary Stem Stability For Total Hip Arthroplasty Using Numerical Modal Analysis Based On Preoperative Three-dimensional Planning", *EORS 2014 - European Orthopaedic Research Society, Annual Meeting*, Nantes, France, July 2014, **Oral presentation**.